



**UNIVERSIDAD
DE ANTIOQUIA**

**EFFECT OF THE ADDITION OF SOLID
PARTICLES ON THE CAPACITY OF THERMAL
STORAGE OF NITRATE BASE SALTS**

Autor

Marllory Isaza Ruiz

Universidad de Antioquia

Facultad de Ingeniería, Departamento de Ingeniería de
Materiales

Medellín, Colombia

2021



Effect of the Addition of Solid Particles on the Capacity of Thermal Storage of Nitrate Base
Salts

Marllory Isaza Ruiz

Tesis como requisito parcial para optar al título de:

Doctorado en Ingeniería de Materiales

Asesores:

Maryory Astrid Gómez Botero Doctora en Técnicas Instrumentales de La Física

Francisco Javier Bolívar Osorio Doctor en Física de Materiales

Línea de Investigación:

Energías renovables

Grupo de Investigación:

CIDEMAT

Universidad de Antioquia

Facultad de Ingeniería, Departamento de Ingeniería de Materiales

Medellín, Colombia

2021.

This Doctoral thesis has been carried out in the Centro de Investigación, Innovación y Desarrollo de Materiales-CIDEMAT at the University of Antioquia, within the framework of the project “Efecto de la Adición de Partículas Sólidas en la Capacidad de Almacenamiento Térmico de Sales Base Nitratos” funded by Ministerio de Ciencia Tecnología e Innovación, Minciencias, through the program “Doctorados Nacionales 727-2015”

ABSTRACT

Concentrating Solar Power plants (CSP) is part of the technologies recently developed as one of the alternatives to provide for the high energy demands and the consumption of fossil sources. The main advantage of the CSP plants is the Thermal Energy Storage system (TES) which allows the production of electricity even in the absence of sunlight, achieving a reduction of the Levelized Cost of Energy (LCOE) up to 46% in 2018 compared to the value for 2010. However, the LCOE is still high in comparison with other renewable energies; therefore, researches on the subject focuses on reducing this value and making CSP technology more competitive. Molten salt-based nanofluids (MSBNFs), a stable colloidal suspension of nanomaterials with average sizes < 100 nm in molten salt, have aroused great interest thanks to the significant improvement to the low thermophysical properties of the molten salt currently used as storage fluids in TES or heat transfer fluid (HTF) increase in thermal properties. The specific heat capacity of the molten salt is typically less than $2 \text{ J}/(\text{g}^\circ\text{C})$ and thermal conductivity less than $\sim 1 \text{ W}/(\text{m K})$. However, there is still no consensus regarding the percentage of increase in the thermal properties of nanofluids as well as the mechanisms responsible that.

For this reason, this doctoral thesis focuses on the understanding of the effect of nanoparticles on MSBNFs by using Hitec salt as the base fluid and alumina nanoparticles as an additive at three different concentrations, 0.5, 1.0 and 1.5 wt.%, seeking not only to establish the effect on the specific heat capacity but also the aggressiveness of the salt towards metals. In the same way, a new method for the synthesis of MSBNFs is established by replacing the water of the traditional two-step method with butanol in order to guarantee the suspension of the nanoparticles and, in turn, the homogenization of the system. Hence, the thermal characterization, specific heat capacity evaluated by Modulated Differential Scanning Calorimetry, the melting point for Differential Scanning Calorimetry and the thermal decomposition obtained by Thermogravimetric analysis are presented, as well as the evaluation of the corrosive behavior of both the pure salt and the nanofluid with the highest specific heat capacity obtained on an austenitic stainless steel AISI 304, in a test up to 2000 h at 550°C , employing two reactors designed to have temperature control, controlled

atmosphere, and continuous mechanical agitation. The thermal and chemical stability of the pure Hitec and the molten salt-based nanofluid during the corrosive behavior evaluation is reported.

The results showed a significant increase of the specific heat capacity in all the evaluated samples, up to 18.74% with the traditional two-step method and 14.63% with the new proposed method; in the same way, a reduction of the melting point up to 4.93% and little influence on the decomposition temperature. On the other hand, a less corrosive effect was evidenced for the nanofluid compared to the pure salt, thanks to the penetration of the solid nanoparticles inside the corrosion layer. Additionally, the chemical stability of the salts and the nanofluids during the corrosion tests was assessed, thanks to the characteristic bands of the nitrite ion found in Raman spectrometry. Given the above, the feasibility of applying the proposed synthesis to obtain molten salt-based nanofluids for thermal storage in CSP plants was successfully assessed, as well as the possibility of using these nanofluids without major damage to the system, e.g. tanks, valves and pipelines. All the samples synthesized exhibited an increase in energy storage capacity with a proportional decrease in the cost of storage. However, the water elimination process was not considered in the calculations. For that reason, the time and the energy cost of removing the solvent can be the deciding factor between the traditional and new two-step method. By using a solvent with low vapor pressure, like ethanol, instead of water, the new two-step method may be more adequate than the traditional method. Thereby, the increase of the specific heat capacity, as well as the energy storage capacity by the addition of alumina nanoparticles, it can contribute to a significant reduction in the size of thermal energy storage tanks, which leads to a reduction of LCOE of CSP plants, making it a competitive technology when compared to other renewable energy systems, and even more so to traditional ones.

DEDICATION

Dedicated to my sweet husband and my family.

Thanks for your love and encouragement.

ACKNOWLEDGMENTS

Primero que todo quiero agradecerle a Dios por permitirme tener vida y salud para lograr una meta más de las tantas que me he propuesto en la vida. A mis padres por su apoyo y educación que han hecho de mí la persona que hoy soy. A mi esposo, quien desde el momento que nos conocimos ha sido mi hombro y sustento en cada uno de los momentos más difíciles, no solo personal sino también profesional y me ha regalado los momentos más felices de mi vida, sin él esto jamás hubiera sido posible.

Agradezco a mi alma máter, mi Universidad de Antioquia que me acogió cuando era solo una joven de pregrado, me permitió cumplir uno de los viajes más gratificantes para realizar mi doble titulación en Francia y ahora poder volver a mis inicios y realizar con éxito este proyecto de vida, mi doctorado. Agradezco con el corazón al grupo CIDEMAT, su director Félix Echeverría, profesores que lo conforman y mis compañeros una gran familia, por las discusiones, indicaciones y consejos que de una u otra forma me ayudaron a encontrar el camino cuando estaba perdiendo el rumbo. En especial, a mis tutores Maryory Gómez y Francisco Bolívar por sus enseñanzas, acompañamiento e infinita paciencia en este proceso, y a mis compañeros más allegados que recorrieron conmigo todo este camino, Carolina Villada, Yineth Galindez, Julián Lenis, Sara Aguilar, Nathaly Arias, Tiffany Marín, Carolina Cárdenas, Darling Perea, Sara Giraldo, Santiago Cartagena y Dayana Mesa. Además de mis amigas que a pesar de la distancia siempre han estado ahí para apoyarme, Vanessa Orozco y Carolina Londoño. Nadie dijo que sería fácil, por eso pocos nos adentramos en el profundo mundo de la investigación

Agradezco también, a las personas que me acogieron en mi pasantía en el departamento de Ingeniería Mecánica de la Universidad de Texas A&M, Estados Unidos, al Dr. Debjyoti Banerjee por permitirme estar en su grupo. Esta experiencia me ayudó a entender mucho más mi sistema y crecer personalmente. A la profesora Mónica Álvarez y sus estudiantes Carolina Cano y Andrés Zapata de la Universidad de Eafit donde realicé gran parte de mis análisis térmicos, por su paciencia y colaboración. A las profesoras Leonor Hernández y Rosa Mondragón de la Universitat Jaume I, con quienes tuvimos la oportunidad de realizar una excelente colaboración. Y al Ingeniero Diego Cardona y su equipo, quienes nos apoyaron en el diseño y fabricación de los reactores para la evaluación de la corrosión.

Finalmente y no menos importante, agradezco al “Departamento Administrativo de Ciencia, Tecnología e Innovación–COLCIENCIAS”, y a la Universidad de Antioquia por el apoyo financiero, y al programa enlaza mundos por su apoyo económico para la realización de la pasantía doctoral.

NOMENCLATURE

ASTM	American Standard Test Method
CSP	Concentrating Solar Power
DSC	Differential Scanning Calorimeter
EDX	Energy-dispersive X-ray
HTF	Heat Transfer Fluid
FBS	Fuel Backup System
LCOE	Levelized Cost of Electricity
LFC	Linear Fresnel Collector
LHS	Latent Heat Storage
MDSC	Modulated Differential Scanning Calorimeter
MSBNFs	Molten Salt-Based Nanofluids
NM	New Two-Step Method
PCM	Phase Change Material
PTC	Parabolic Trough Collector
PST	Parabolic Dish/Stirling Technology
PV	Photovoltaic
SDT	Stirling Dish Technology
SEM	Scanning Electron Microscope
SHS	Sensible Heat Storage
SPT	Solar Power Tower
SS304	Austenitic Stainless Steel AISI 304
TChS	Thermochemical Storage

TEM	Transmission Electron Microscopy
TES	Thermal Energy Storage
TM	Traditional Two-Step Method
TGA	Thermogravimetric Analysis
XRD	X-Ray Diffraction
ϕ	Volume Fraction
A	Sample Area, cm ²
C_p	Specific Heat Capacity
C_{pnp}	Specific Heat Capacity of nanoparticles
C_{pbf}	Specific Heat Capacity of Base Fluid
D	Density, g/cm ³
ρ_{np}	Density of Nanoparticles
ρ_{bf}	Density of Base Fluid
K	Constant, 8.76*10 ⁴ mm/year
T	Exposure Time
ΔT	Delta of Temperature
T_m	Melting point
m_i	Mass Initial
m_f	Mass final
S_o	Initial Area
W	Mass Loss, grams

TABLE OF CONTENTS

ABSTRACT	4
DEDICATION	6
ACKNOWLEDGMENTS	7
NOMENCLATURE	9
LIST OF FIGURES	14
LIST OF TABLES	17
1. INTRODUCTION	19
2. BACKGROUND	21
2.1 Concentrating Solar Power System	21
2.1.1 Type of Concentrating Solar Power Plant	22
2.1.1.1 Parabolic Trough Collectors (PTC)	23
2.1.1.2 Solar Power Tower (SPT)	23
2.1.1.3 Linear Fresnel Collector (LFC)	24
2.1.1.4 Parabolic Dish /Stirling Technology (PST)	24
2.1.2 Thermal Energy Storage System	25
2.1.2.1 Sensible Heat Storage	26
2.1.2.2 Latent Heat Storage	26
2.1.2.3 Thermochemical storage	26
2.2 Eutectic Molten Salts	27
2.2.1 Commercial Molten Salt: HITEC	32
2.3 Nanofluids	33
2.3.1 Molten Salt-Based Nanofluids (MSBNFs)	33
2.3.2 Preparation Methods of Molten Salt-Based Nanofluids	38
2.4 Thermophysical Properties of Nanofluids	39
2.4.1 Specific Heat Capacity	39
2.5 Corrosive Behavior	40
3. HYPOTHESIS AND OBJECTIVES OF THIS STUDY	42
3.1 Hypothesis	42
3.2 Objectives	42
3.3 Significance of this Study	43
4 EXPERIMENTAL METHODS	45
4.1 Preparation method of Molten Salt-Base Nanofluids	47

4.1.1	Preparation of the molten salt.....	47
4.1.2	Traditional Method: Two-step method	48
4.1.3	The proposed new method: Traditional Method with Modification	49
4.2	Thermophysical Properties Determination.....	50
4.2.2	Thermal Analysis.....	51
4.2.2.1	Differential Scanning Calorimetry	51
4.2.2.2	Modulated Differential Scanning Calorimetry	51
4.2.2.3	Thermogravimetric Analysis.....	52
4.3	Raman Spectrometry.....	52
4.4	Corrosive Behavior of Molten Salt-Based Nanofluids with Container Materials.....	52
4.4.1	Corrosive Behavior Test.....	53
4.4.2	Characterization Techniques	55
4.4.2.1	Transmission electron microscopy TEM	55
4.4.2.2	Scanning Electron Microscopy (SEM).....	55
4.4.2.3	X-Ray Diffraction (XRD).....	56
5	EXPERIMENTAL RESULTS	57
5.1	Characterization of alumina nanoparticles	57
5.1.1	Morphology of Alumina	57
5.1.2	Thermal properties.....	59
5.1.3	Composition and Structure by XRD.....	61
5.2	Thermophysical properties of Hitec and the MSBNFs.....	63
5.2.1	Melting Temperature (T _m)	63
5.2.2	Specific Heat Capacity (C _p).....	68
5.2.3	Microstructural Analysis	74
5.2.4	Thermal Stability.....	78
5.2.5	The storage capacity of the Hitec and MSBNFS	82
5.3	Conclusion	85
5.4	Corrosive Behavior Test of Hitec and Molten Salts-Based Nanofluids in contact with AISI 304.....	87
5.4.1	Composition and Structure by XRD.....	87
5.4.2	Morphological development by SEM/EDX analysis	90
5.4.3	Mass Change and Corrosion Rate	99
5.5	Conclusion	111

5.6	Pure Hitec and MSBNF with 1.5%Al₂O₃ evaluation after corrosive behavior test	113
5.6.1	Melting point evaluation	113
5.6.2	Scanning Electron Microscopy SEM	114
5.6.3	Raman Spectrometry of the pure Hitec and MSBNF during the corrosive behavior test	117
5.6.4	XRD	125
5.7	Conclusion	128
6.	SUMMARY	129
6.1	Summary	129
6.2	Main Achievements	133
6.3	List of Products	133
6.4	Future Directions	135

LIST OF FIGURES

Figure 1. CSP Thermal Energy Storage Global Capacity and Annual Additions [1].....	20
Figure 2. Scheme of a typical concentrating solar power plants.	21
Figure 3. Types of CSP plants [15].....	22
Figure 4. Classification of the thermal energy storage systems.	27
Figure 5. Phase diagram of binary molten salt NaNO ₃ -KNO ₃ according to (a) Coscia et al. [46] and (b) FactSage software.....	31
Figure 6. Two-step synthesis of MSBNFs, established by Shin and Banerjee in 2011 [68].....	38
Figure 7. Methodology flow chart of molten salt-based nanofluids studied.....	46
Figure 8. The traditional method to develop Molten Salt-Based Nanofluids.....	48
Figure 9. Molten salt-based nanofluid a. before and b. after fusion.	49
Figure 10. The new proposed method, traditional method modify to prepare the Molten Salt-Base Nanofluids.....	50
Figure 11. Image of a. Reactors designed to evaluate the corrosion behavior in this work, b. samples holder with three different positions inside the reactor and c. Stainless Steel AISI 304 samples.	54
Figure 12. Morphological features of pristine alumina nanoparticles used to elaborate the MSBNFs. a. SEM image, b. TEM image and c. the size distribution obtained from TEM images.	58
Figure 13. TGA of pristine alumina nanoparticles.	61
Figure 14. The XRD pattern of a. pristine alumina and b. calcined alumina.	62
Figure 15. Comparison of melting points of the traditional two-step method and the new two-step method.....	65
Figure 16. DSC of a. pure Hitec, b. MSBNF prepared by the traditional method (TM), c. MSBNF by the new method (NM), d. and e. close-up at the melting peak for TM and NM respectively.....	67
Figure 17. Graphic representation of salt embedding between nanoparticles.	68
Figure 18. Comparison of the specific heat capacity of the Traditional two-step method, New two-step method, and the theoretical models.	74
Figure 19. SEM Images of pure Hitec.....	75

Figure 20. SEM images after MDSC evaluation a, b, c samples elaborated by traditional two-step method with 0.5, 1.0 and 1.5 wt.% of alumina nanoparticles, respectively, and d, e, f .sample elaborated by new two-step method with 0.5, 1.0 and 1.5 wt.% of alumina nanoparticles, respectively.	76
Figure 21. Example elemental mapping, MSBNF with 0.5 wt.% of Al ₂ O ₃ obtained by TM after the MDSC evaluation (O-white, Na-green, Al-blue, K-orange, and N-red).....	78
Figure 22. Decomposition temperature under N ₂ atmosphere of pure Hitec from TGA measurements.	79
Figure 23. Decomposition temperature under N ₂ atmosphere of the MSBNFs synthesized by TM and NM, from TGA measurements.....	80
Figure 24. Derivate weight change showing bulk decomposition processes of the MSBNFs synthesized by a. TM and b. NM.	82
Figure 25. The XRD pattern of AISI 304 immerses in a. Hitec and b. MSBNF after 672 h at 550°C, in the bottom and medium position inside the reactors.	89
Figure 26. SEM images of the surface of metal samples in contact with pure Hitec after 500 h and 2000 h immersion test, in three different positions bottom, medium, and top.....	91
Figure 27. SEM images of the surface of metal samples in contact with MSBNF with 1.5 wt.% of Al ₂ O ₃ after 500 h and 2000 h immersion test, in three different positions bottom, medium, and top.....	92
Figure 28. Cross-section of the metal samples in contact with the pure Hitec after 500 h and 2000 h immersion test, in three different positions bottom, medium, and top.	93
Figure 29. Cross-section of the metal samples in contact with the MSBNF with 1.5 wt.% of Al ₂ O ₃ after 500 h and 2000 h immersion test, in three different positions bottom, medium, and top.	94
Figure 30. EDX mapping of SS304 surface after 2000 h of exposure time in MSBNF with 1.5 wt% of Al ₂ O ₃	96
Figure 31. EDX mapping of SS304 surface after 2000 h of exposure time in Hitec.....	97
Figure 32. Detail of the cross-section of the SS304 specimens after 2000 h immersed into a. Pure Hitec and b. MSBNF with 1.5 wt% of Al ₂ O ₃	98
Figure 33. Proposed diagram of the oxidation process of SS304 immersed in a. Hitec and b. the MSBNF.....	99

Figure 34. Gravimetric gain test at 550°C during 2000 h of the Molten salt Hitec (R1) and the MSBNF with 1.5 wt.% of Al ₂ O ₃ (R2) a. in the bottom (B), b. in the medium (M) and c. in the top (T) of the reactor.	102
Figure 35. SEM image and EDX mapping of aliquot at 2000 h of exposure of MSBNF in the reactor.	103
Figure 36. Mass loss of corroded samples immersed during 2000 h in three different position bottom (B), medium (M), and top (T), in a. Hitec (R1) and b. MSBNF with 1.5 wt.% of Al ₂ O ₃ (R2).	105
Figure 37. Corrosion rate of the pure Hitec and MSBNF with 1.5% Al ₂ O ₃ , a. 1000 h and b. 2000 h of exposure time	108
Figure 38. SEM image and EDX mapping of SS304 surface after 2000 h of exposure time in MSBNF with 1.5 wt.% of Al ₂ O ₃ in the top position.	109
Figure 39. SEM image and EDX analysis of SS304 sample after 2000 h of exposure time in MSBNF with 1.5 wt.% of Al ₂ O ₃ in the medium position.	110
Figure 40. SEM images of the aliquot of Hitec and MSBNF from the reactor after 1000, 1500, and 2000 h of corrosive behavior test.	115
Figure 41. SEM image and EDX mapping of the aliquot of MSBNF from the reactor after 1500 h of corrosive behavior test.	116
Figure 42. Raman spectra of pure Hitec.	118
Figure 43. Raman spectra of the MSBNF with 1.5 wt.% of Al ₂ O ₃ , a. showing the presence of nanoparticles and b. MSBNF without the presence of nanoparticles.	119
Figure 44. Rama spectra of pristine alumina nanoparticles.	120
Figure 45. Evaluation of the chemical stability by Raman during the corrosive behavior test of the Hitec.	122
Figure 46. Evaluation of the chemical stability by Raman during the corrosive behavior test of the MSBNF with 1.5 wt.% of Al ₂ O ₃	124
Figure 47. The XRD pattern of the aliquot of a. Hitec and b. close view of Hitec, c. MSBNF, and d. close view of MSBNF, after 2000 h at 550°C.	127
Figure 48. Summary scheme with the main properties evaluated in this research.	132

LIST OF TABLES

Table 1. Main characteristics of CSP plants [5], [7], [11], [19], [20].	25
Table 2. Thermal properties of commercial molten salts.	29
Table 3. Characteristics of commercial molten salt Hitec [5], [25], [39], [40], [45], [48].	32
Table 4. Properties of molten salt-based nanofluids: Experimental data from the literature.	36
Table 5. The reported level of impurities in the nitrate/nitrite salts.	47
Table 6. Chemical composition of the studied AISI 304 alloy according to ASTM A240.	54
Table 7. Specific Heat capacity of alumina nanoparticles and bulk.	59
Table 8. Thermal properties of bulk alumina from literature.	60
Table 9 The melting point of pure Hitec and MSBNFs.	65
Table 10. Average specific heat capacity at 300 °C of pure Hitec and the MSBNFs by both methods, Traditional Method (TM) and New Method (NM).	71
Table 11. Specific heat capacity of different particle concentrations obtained by the Simple mixing model.	73
Table 12. Thermal stability analysis under N ₂ of pure Hitec and MSBNFS by both methods studied.	81
Table 13. Storage capacity and Effective storage fluid cost of the Hitec and MSBNFs synthesize by two-step traditional and new methods.	84
Table 14. Quantitative Rietveld analysis of SS304 immersed in Hitec and MSBNF after 672 h at 550°C, in the bottom and medium position inside the reactors.	90
Table 15. Agreement indices for the Rietveld fitting procedure.	90
Table 16. EDX results of the cross-section of the SS304 specimen after 2000 h immersed into pure Hitec and the MSBNF, where A-1, A-2 and A-3 are the areas evaluated by the EDX demarcated within the image.	98
Table 17. Melting point of pure Hitec and MSBNFs after the corrosive behavior test.	114
Table 18. Raman band shifting for pure NaNO ₃ , NaNO ₂ , and KNO ₃ , components of Hitec [97].	118
Table 19. Raman bands of Hitec during corrosive behavior test.	121
Table 20. Raman bands of Hitec with 1.5 wt.% of Al ₂ O ₃ during corrosive behavior test.	123

1. INTRODUCTION

Since the industrial revolution, remarkable advances in different fields as engineering, science, and technology have been possible by using fossil fuels as a dense and inexpensive source of energy. However, nowadays we are in an energy crisis as a result of non-renewable energy sources from these fuels and the strong demand for electricity, followed by the rapid and uninterrupted increase in economic development. Therefore, research on renewable energy sources has garnered significant attention recently to reduce the use of non-renewable sources and their associated CO₂ emissions.

At present, there are several renewable energy sources (e.g. wind, oceanic, geothermal and solar), of which solar energy being the most promising thanks to its inexhaustible source, i.e. the solar irradiation. Among technologies for solar energy harvesting, the direct method by photovoltaic (PV) and the indirect method by Concentrating Solar Power System (CSP), the second is particularly attractive due to its scalability, high efficiency and low operating costs, with an annual production of around 5.5 GW in 2018 and a forecast of 10 to 22 GW by 2025 [1]. The main principle of the CSP plants is to heat a fluid by using mirrors that concentrate and direct the sunlight and finally use the concentrated heat to convert it into electricity in a conventional way [2], [3].

Within the components of CSP technology, the thermal energy storage system (TES) plays an essential role, through which energy is produced even at night, while mitigating fluctuations in cloudy periods and change power generation from the hours of greatest solar radiation to the hours of greatest demand (e.g at night), thus making it a competent system compared to other sources of renewable energy [4], [5], [6]. The currently implemented TES system, based on two-tank molten salt storage technology, shows a > 98% efficiency with a deployment worldwide of 17 GWh of thermal energy storage in 2018, see **Figure 1**; for the same year, almost all ongoing projects, except 3 out of 23, plan to use TES in Africa, Asia, the Middle East and South America [1].

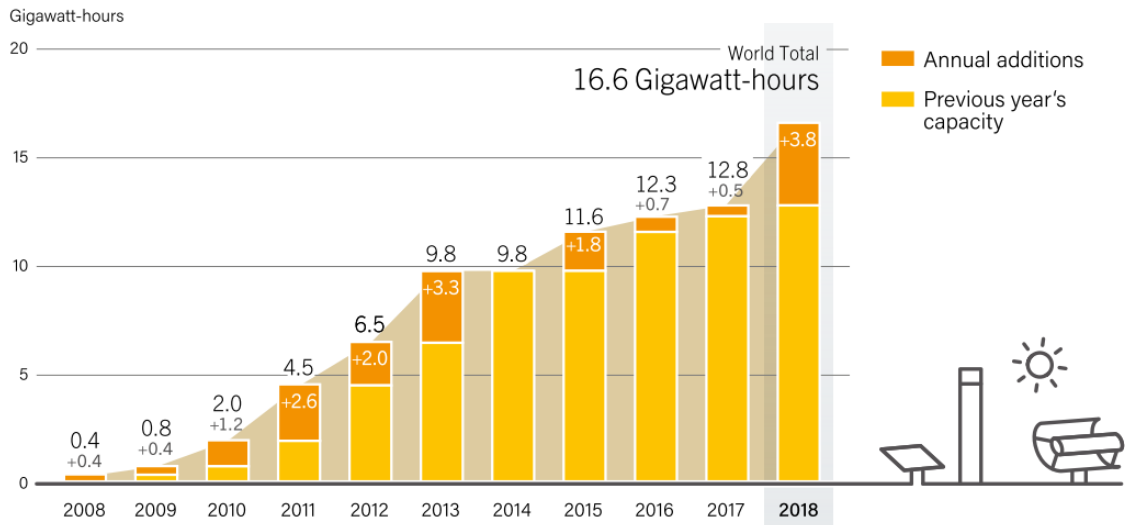


Figure 1. CSP Thermal Energy Storage Global Capacity and Annual Additions [1].

Molten salts are used as a storage medium in CSP plants thanks to its high thermal stability, high volumetric heat capacity, low vapor pressure, chemical stability, availability, and profitability, obtaining storage up to 944.000 MW/year with a thermal efficiency up to 40% [7]. However, these salts have low specific heat capacity, low thermal conductivity, high viscosity, and high corrosivity, so they are still under research [8]. The use of the addition of solid nanoparticles with size less than 100 nm in the molten salt (nanofluid), is being investigated in order to improve the thermophysical properties. Most of the reports on nanofluids with molten salts as base fluid have shown a significant increase in thermal properties compared to the pure salt by using low concentrations of nanoparticles, <2%.

The present doctoral thesis provides an understanding of the effect of the addition of alumina nanoparticles on the thermal properties of Hitec salt, evaluating two different synthesis methods and determining the specific heat, melting point, and decomposition temperature, as well as the aggressiveness of one of the nanofluids against austenitic stainless steel AISI 304, compared to Hitec base salt through the use of two reactors designed and manufactured in this project at controlled temperature, atmosphere, and under constant mechanical agitation..

2. BACKGROUND

2.1 Concentrating Solar Power System

Among the various renewable energy resources explored today, concentrating solar power (CSP) represents one of the most promising green technologies for producing electric energy, being its main advantage, the use of a thermal energy storage system (TES) that allows CSP plants to operate even in the absence of solar rays [6]. The different configurations of CSP plants share the same principle: *i.* lenses, mirrors, or heliostats used as reflectors and routers for incident sunlight, either on a point or on a line receiver, to produce heat at medium (about 400-550°C) or high (about 600-1000°C) temperatures; *ii.* central solar receiver to absorb the sunlight and convert it to heat; *iii.* heat transfer fluid (HTF), which can be water, fatty acid, synthetic oils, or molten salts, depending on the system; *iv.* thermal energy storage (TES) to compensate for the intermittent solar irradiance and to allow for night time operation of the plant; and *v.* the habitual power conversion module responsible for finally converting the received energy into electricity (e.g., Rankine or Stirling cycle) [3], [9]–[11]. **Figure 2** shows a typical scheme of operation of the CSP plants.

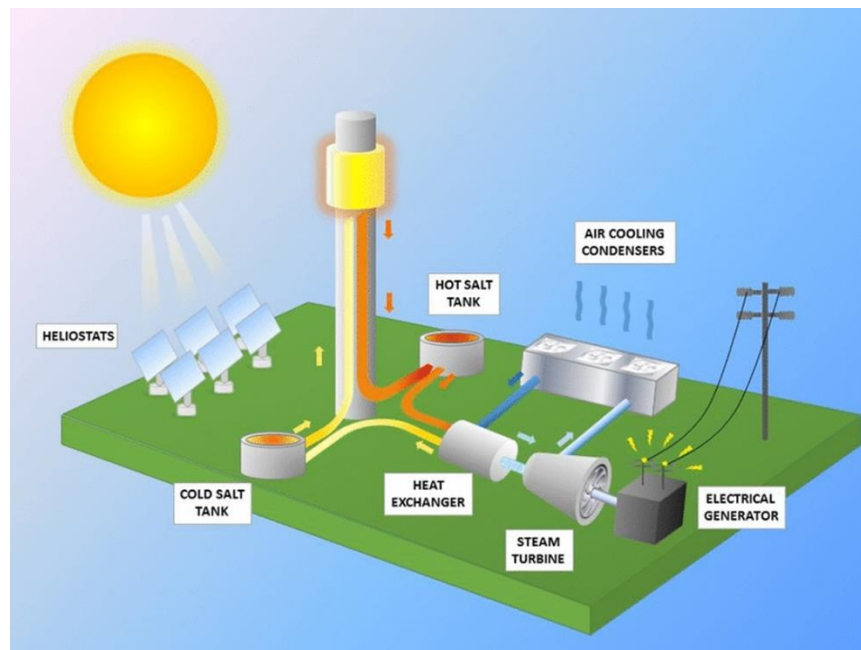


Figure 2. Scheme of a typical concentrating solar power plants.

2.1.1 Type of Concentrating Solar Power Plant

Currently, there are four major types of CSP technologies, namely: parabolic trough collectors, solar power towers, dish Stirling engines, and linear Fresnel collectors. **Figure 3** shows the different types of plants, which can be classified based on their geometry into line-focus concentrators (parabolic trough and linear Fresnel collector, with geometrical concentration ratio up to 100) or point-focus concentrators (dish Stirling and power tower, with geometrical concentration ratio up to 1000). Despite the high efficiency achieved with point focus geometries, this configuration is more expensive and complex than the line focus [11]. Global CSP power capacity increased by 11%, which was 5.5 GW, in 2018, with most plants installed in Spain and the United States [1]. In turn, these countries invest more budget in research to improve the technology of different types of plants, of which more than 82% of the CSP installations are parabolic-trough plants, with an important growth in studies and implementation of the tower plants thanks to its high operating temperatures and subsequent increased efficiency [1], [12], [13][14].

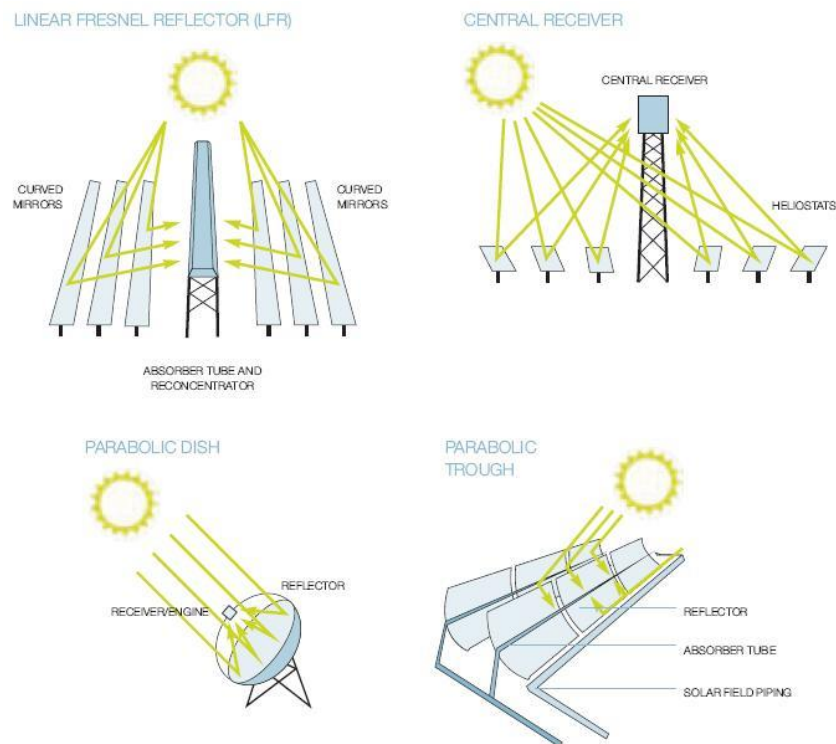


Figure 3. Types of CSP plants [15].

2.1.1.1 Parabolic Trough Collectors (PTC)

The basic operation of the parabolic trough collectors (PTCs) is to collect and direct the solar radiation through parabolic-shaped mirrors that track the sun throughout the day on a single- or dual-axis tracking system. The sunlight is reflected on a tube with a heat transfer fluid inside (water, oil or molten salt) to transport the collected energy. Optionally, a TES or fuel backup system (FBS) can be incorporated to store the energy and use it in the absence of the sun or during times of low-density solar irradiance. Finally, the system uses a conventional power conversion module to generate electricity [16], [17].

Even though there are other types of CSP technologies, parabolic trough systems are the most developed and widely accepted technology. The first PTC plant (called SEGS I) was installed in the Mojave desert in California (United States) in 1984, using mineral and synthetic oils as heat transfer fluids [17], [18].

2.1.1.2 Solar Power Tower (SPT)

Solar power tower (SPT) plants consist of thousands of fixed flat -or slightly bended- mirrors or heliostats arranged habitually around a tower in a circular shape. Each of these mirrors moves independently in such a way to allow the solar ray to be reflected towards a receiver located in the upper part of the tower. The concentrated radiation is transferred to an HTF which converts the energy into superheated steam used for the normal operation of the generator. Currently, the HTF is water/steam, air, or molten salt, which transports the heat until the exchanger and the turbine system. SPT plants can work in a temperature range from 250 to 600°C, and they could reach 1000°C in the future depending on the fluid [11], [19].

Due to the very high concentration ratios of SPTs, they are more efficient as they can achieve higher temperatures compared to the parabolic trough and linear Fresnel concentrators [19]. However, a wide space is required to establish this configuration, typically around 4.6 m²/MWh/yr, making the installation difficult [11].

2.1.1.3 Linear Fresnel Collector (LFC)

Similar to PTCs, the linear Fresnel collector (LFC) concentrates the sunlight on a line. This type of plant is composed of reflectors (flat or slightly curved mirrors) simulating a curved mirror due to the adjustable angle of each line of mirrors. A secondary reflector is needed to refocus the rays, and the receiver is a long tube located a few meters above the primary mirrors [19]. Although PTC plants are 15% more efficient than LFC plants, they are more cost-effective, have a light weight structure, and they use conventional mirrors. Furthermore, the mirrors being rested on the ground reduces their maintenance costs and gives better access for cleaning.

2.1.1.4 Parabolic Dish /Stirling Technology (PST)

Parabolic dish/Stirling technology (PST) is the oldest solar technology. The first plants based on the cycle of Rankine and Stirling started to operate in 1800, but the modern technology was not developed until 1970 and 1980. The way of focusing incident radiation in PST systems works like that of SPT plants, i.e. the radiation is reflected at a focal point. A PST system consists of a parabolic dish like a satellite dish, and the receiver is a Stirling engine or a micro-turbine that convert the sunlight directly to electrical power [11]. Despite the high operating temperatures that can be achieved using this technology, resulting in higher overall system efficiencies compared to the other technologies, there are no commercial plants in operation and the storage system is still in the research stage [19]. *Table 1* shows the typical characteristics of each configuration of CSP plants.

Table 1. Main characteristics of CSP plants [5], [7], [11], [19], [20].

	Parabolic Trough Collector	Solar Power Tower	Linear Fresnel Collector	Stirling Dish Technology
Typical capacity (MW)	10-200	10-200	10-200	0.01-0.025
Operating temperatures (°C)	290-390	250-500	250-390	250-700
Plant peak efficiency (%)	14-20	23-35	~18	~30
Thermal efficiency (%)	30-40	30-40	N/D	30-40
Concentration ratio (suns)	70-80	300-1000	25-100 (depending on the secondary reflector)	1000-3000
Capacity factor (CF) (%)	20-25 (without TES) 40-53 (6hr storage)	40-53(6-7.5hr storage) 65-80(12-15hr storage)	22-24	25-28-
Annual solar-to-electricity conversion (%)	15-16	20-35	8-10	26
First commercial plant	SEGS I Since 1984	For molten salt as HTF: Gemasolar Since 2011	CLFR plant Since 2000	Tooele Army Depot plant (Under construction)
Storage with molten salts	Commercially available	Commercially available	Possible, but not proven	Possible, but not proven
Capital Cost (US\$/kW)	3900–4100 (without TES) 6300–8300 (6 hr storage)	5700–6400 (6–7.5 hr storage) 8100–9000 (12–15 hr storage)	N/D	12,578
Operational and maintenance cost (US\$/kWh)	0.012-0.02	0.034	N/D	0.21

2.1.2 Thermal Energy Storage System

Given that the major disadvantage of solar energy is the intermittency of its source, i.e., solar radiation, numerous studies aim to develop energy- and cost-effective thermal energy storage systems [3]. In this way, some researchers are focused on the improvement of the structure of the plants, while most of them are focused on developing new materials with thermal

properties superior to the currently used. A well-established TES system can be classified into three categories: i. sensible heat storage (SHS) ii. latent heat storage (LHT), and iii. thermochemical storage (TChS). The main characteristics of each of these thermal storage forms are listed below.

2.1.2.1 Sensible Heat Storage

Sensible heat storage (SHS) is a form of energy storage, in which the temperature of the material or the substance increases without experiencing a phase change throughout the temperature range required in the storage process [4]–[6], [21]. Among the commonly used sensible heat storage materials are oils, which have a relatively low density, a low storage capacity, and a low maximum working temperature, up to 300°C. These characteristics increase the operating cost, given the relatively low peak efficiencies (due to the low operating temperatures) [4]. On the other hand, molten salts have been used in solar thermal applications, dominating the TES sector for large scale applications [22] due to their high density, low vapor pressure, low chemical reactivity, high operating temperature (up to 500°C [23]), moderate cost compared to other materials used for thermal storage, and the possibility of being used both as energy storage materials as well as heat transfer fluids. However, pure molten salts have high melting points. For this reason, eutectic molten salts (homogenous mixtures of different salts) are an attractive option for reducing the cost of electricity generation. By using these mixtures, it is possible to reduce the melting point considerably [24]–[26].

2.1.2.2 Latent Heat Storage

Latent heat storage (LHT) uses materials called phase change materials (PCMs), these materials experience a phase change in the operating temperature range. The phase-transition enthalpy changes are substantially larger (100~1000 times) than those of sensible heat storage for the same amount of used storage materials [27]–[32]. However, PCMs suffer from low thermal conductivity (0.2~0.5 for paraffin and inorganic salts) and, thus, enhanced heat transfer techniques are required to improve the power rating of these platforms [33].

2.1.2.3 Thermochemical storage

Thermochemical storage (TChS) uses the released energy of the exothermic reaction [34], [35] of some materials such as carbonates, hydroxides, and metallic hydrides [22]. The main advantages of this storage method are the high volumetric energy density (5 and 10 times higher than latent and sensitive heat storage, respectively), the wide range of operating temperatures, and the storage at room temperature [36]. However, this kind of energy storage system is still at laboratory level.

It is important to highlight that the usage of TES system confers a competitive advantage of CSP over photovoltaic (PV) technology in commercial and utility-scale power generation, thanks to the possibility of operating the plant during the night time or periods without solar rays (e.g., during cloudy conditions), and the low costs of thermal energy storage, compared to electric energy storage. *Figure 4* shows the classification of the different type of TES systems used to store the energy in CSP technology.

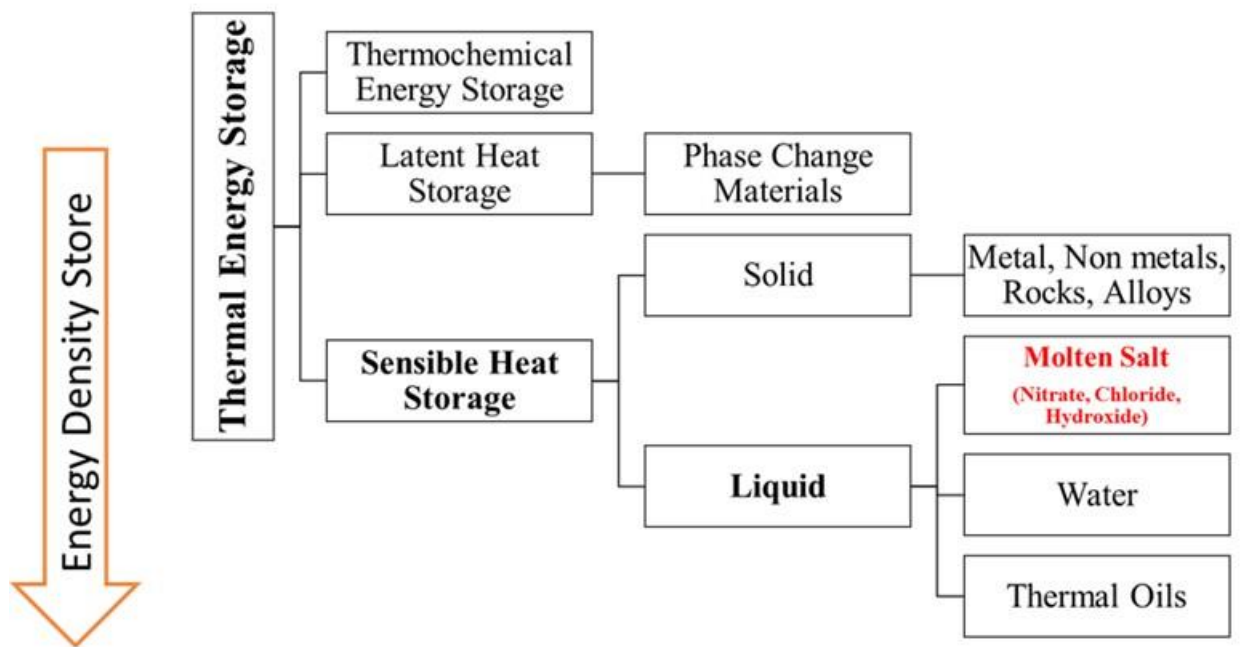


Figure 4. Classification of the thermal energy storage systems.

2.2 Eutectic Molten Salts

A eutectic system is a homogenous mixture of two or more species with a specific ratio (eutectic ratio) and with a single melting point lower than the pure species. This

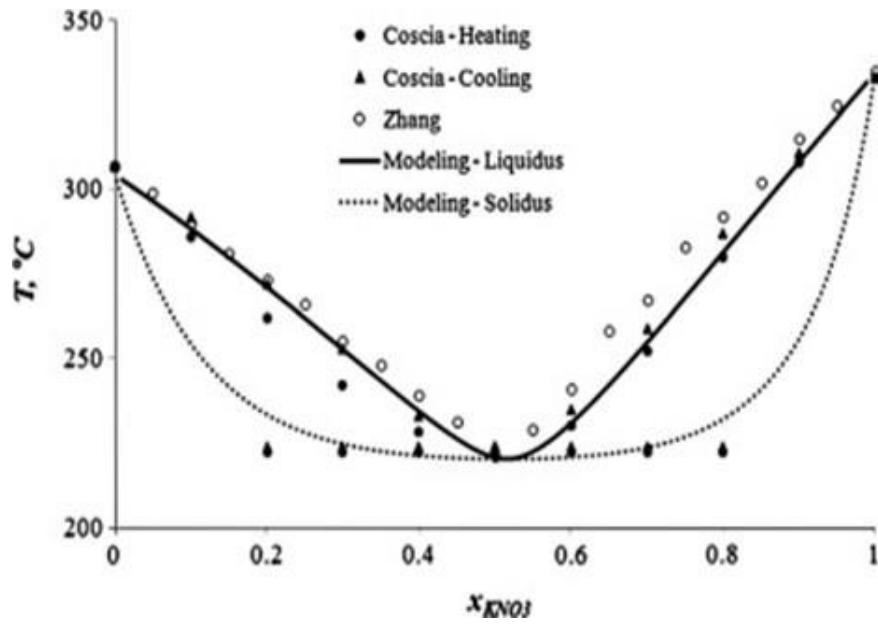
temperature is known as a eutectic temperature which is the lowest melting temperature compared to other possible mixing ratios. Phase diagrams and thermodynamic descriptions can be used to evaluate and determine the eutectic ratio and the melting point related to the components. However, molten salts comprised of more than two components have more than one eutectic point, and the eutectic ratio [37].

Nitrate/nitrite salts, carbonate salts, chloride/fluoride salts, and their mixtures, have been the most studied salts. **Table 2** shows a comparison of the thermo-physical properties of several common eutectic salt mixtures with different cations and anions. From this information, the low melting point of the nitrate/nitrite salt is evident. For that reason, molten salts have been used (starting from the year 1980) as a storage and a heat transfer medium in solar thermal solar plants such as Gemasolar and Andasol due to their high heat capacity, wide working temperature range, and low cost, with storage capacity up to 15 h in the case of Gemasolar [35]. Among binary molten salts, the most used salt is Solar Salt, comprised of 60 wt.% NaNO_3 -40 wt.% KNO_3 , with a melting point of 223 °C, a working temperature range from 290 – 580 °C, and a specific heat capacity of 1.49-1.54 J/g.°C [25], [38], [39]. **Figure 5** shows different phase diagrams reported in the literature for the binary molten salt composed of NaNO_3 and KNO_3 , all of them show that the eutectic ratio is near 50-50 wt.% of each component, with a single melting point ca. 223°C.

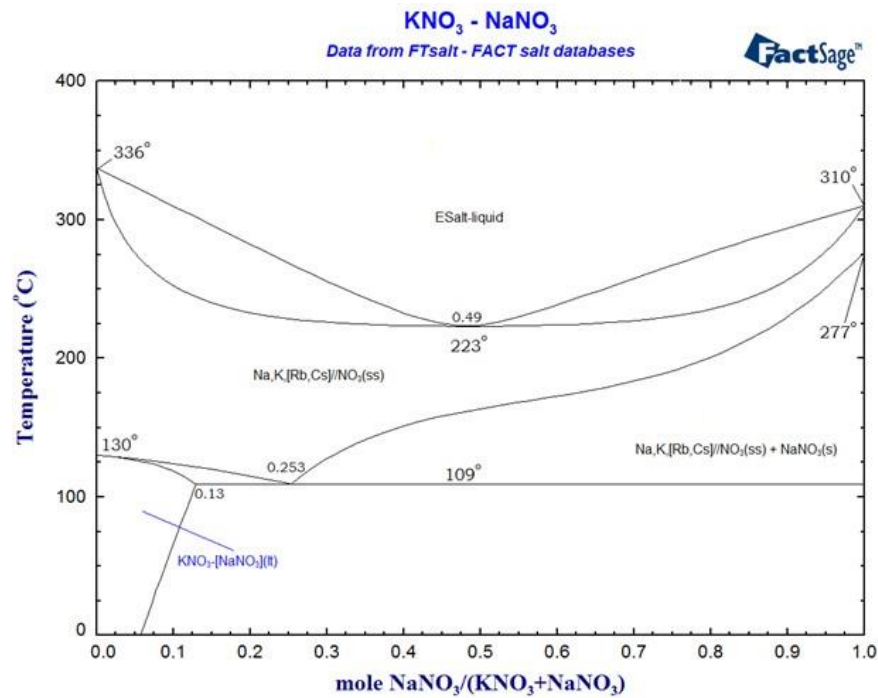
Table 2. Thermal properties of commercial molten salts.

	Melting Point (°C)	Stability (atmosphere) (°C)	Heat Capacity (kJ/kg.K)	Thermal Conductivity (W/m.K)	Density (g/cm³)	Viscosity (Pa.s)
Solar Salt NaNO ₃ (60 wt.%) - KNO ₃ (40 wt.%)	220 [40] 221 [25]	585 [5] 600 [40] 560 (air) [41]	1.54 [25] 1.49 [39], [38]	0.55 (at 400°C) [40]	1.752 (at 500°C) [25]	0.00326 (at 300°C) [40]
Hitec NaNO ₃ (7 wt.%) - KNO ₃ (53 wt.%) - NaNO ₂ (40 wt.%)	142 [25], [40], [42], [43]	535 [40]	1.42 (at 500°C) [25] 1.56 (at 300°C) [40] 1.55 [41]	~ 0.2 (at 300°C) [40] 0.492 (at 295°C) [44] 0.61 (at 350°C) [43] 0.48 [41]	1.640 [45] 1.723 (at 500°C) [25]	0.00316 (at 300°C) [40]
Hitec XL NaNO ₃ (7 wt.%) - KNO ₃ (45 wt.%) - CaNO ₃ (48 wt.%)	120 [40] 140 [34], [41]	500 [40] 454 (air) [41] 538 (N ₂) [41] 610 (N ₂) [41] 500(air) [41]	1.45 (at 300°C) [40] 1.40 [41]	0.52 [40], [41] 0.519 [34]	1.992 [45]	0.00637 (at 300°C) [40]
NaNO ₃ (28 wt.%) - KNO ₃ (52 wt.%) - LiNO ₃ (20 wt.%)	130 [40]	600 [40]	1.091 [40]			0.03 (at 600°C) [40]
LiNaK NaNO ₃ (18 wt.%) - KNO ₃ (52 wt.%) - LiNO ₃ (30 wt.%)	120 [41]	550-600 (air) [41] 435 (N ₂) [41] 584 (N ₂) [41] 600 (Ar) [41]	1.60 [41]			
KNO₃ (50-80 wt.%) - LiNO ₃ (0-25 wt.%) - Ca(NO ₃) ₂ (10-45 wt.%)	< 80 [40]	500 [40]		0.43 (at 300°C) [40]		~ 0.004 (at 190°C) [40]
NaNO ₃ (14.2 wt.%) - KNO ₃ (50.5 wt.%) - LiNO ₃ (17.5 wt.%) - NaNO ₂ (17.8 wt.%)	99 [40]	430 [40]	1.66 (at 500°C)			

Sandia Mix. NaNO_3 (9-18 wt.)- KNO_3 (40-52 wt.)- LiNO_3 (13-21 wt.)- $\text{Ca}(\text{NO}_3)_2$ (20-27 wt.)	<95 [40] 72 [41]	500 [40] 510 (N_2) [41] << 400 (air) [41] 574 (N_2) [41]	1.16-1.44 (at 247°C) [40] 1.65 [41]	0.654 (at 250°C) [40] 0.5 [41]		0.005-0.007 (at 300°C) [40]
Halotechnics SS-700 NaNO_3 (6 wt.)- KNO_3 (23 wt.)- LiNO_3 (8 wt.)- CsNO_3 (44 wt.)- $\text{Ca}(\text{NO}_3)_2$ (19 wt.)	65 [40]	500 [40]	1.22 (at 150°C) [40]			
LiNaK carbonate LiCO_3 (32.1 wt.)- Na_2CO_3 (33.4 wt.)- K_2CO_3 (34.5 wt.)	~ 400 [40]	800-850 [40]	~1.4-1.5 [40]			0.0043 (at 800°C) [40]
NaCl (13.4 mol.)- KCl (33.7 mol.)- ZnCl_2 (52.9 mol.)	~ 200 [40]	800 [40]	0.81 (at 300-600°C) [40]	0.325 (at 300°C) [40]		0.004 (at 600-800°C) [40]
Mixtures of alkali-fluorides and carbonates	~ 400 [40]	~ 900 [40]		1.17 (at 400°C) [40]		
Saltstream 700 (Halotechnics SS-700)	257 [40]	700 [40]	0.79 (at 300°C) [40]	0.35-0.4 [40]		0.004 (at 500°C) [40]



a



b

Figure 5. Phase diagram of binary molten salt $\text{NaNO}_3\text{-KNO}_3$ according to (a) Coscia *et al.* [46] and (b) FactSage software.

Thanks to their high heat capacity, wide temperature range, low cost, and negligible environmental impact, molten salts have become a promising heat transfer and storage medium for solar thermal

power applications. Improving the specific heat of molten salt can play a key role in improving the heat storage capacity and reducing the heat storage cost of solar thermal power generation systems.

2.2.1 Commercial Molten Salt: HITEC

Commercial molten salt Hitec is a ternary molten salt developed by Coastal Chemical Company with a composition of 40 wt.% NaNO_2 , 7 wt.% NaNO_3 and 53 wt.% KNO_3 . **Table 3** shows the characteristics of this molten salt. Both, Hitec and Solar Salt, have been commercially used in SPTs and PTCs [5] with a specific heat capacity between 1.42-1.56 J/g. $^\circ\text{C}$ [25], [39], [41]. The main advantage of Hitec, over Solar Salt, is its low melting point (142-147 $^\circ\text{C}$ [40], [47]). On the other hand, at high temperature Hitec has a viscosity comparable to that of water, while having almost double thermal conductivity when compared to traditional organic HTFs [40]. Even though Hitec has low cost and high freezing point compared to other molten salts [48], it does require an N_2 cover gas in the thermal storage tanks at atmospheric pressure and temperatures above 300 $^\circ\text{C}$ to prevent the nitrite from converting to nitrate [43], [48], [49]. For this reason, researchers continue to work on improving the characteristics of these salts, especially by increasing their storage capacity and thermal conductivity. With this objective in mind, new salts have been developed by mixing other nitrates while conserving the proportions of Hitec [24], or by adding solid particles to obtain molten salt-based nanofluids [50], [51].

Table 3. Characteristics of commercial molten salt Hitec [5], [25], [39], [40], [45], [48].

Characteristic	Value	Unit
Melting point	142	$^\circ\text{C}$
Heat capacity at 300$^\circ\text{C}$	1.56	J / g. $^\circ\text{C}$
Working temperature	140-538	$^\circ\text{C}$
Density	1.640 - 1.723	g / cm ³
Thermal conductivity	~ 0.2 (at 300 $^\circ\text{C}$) 0.61 (at 350 $^\circ\text{C}$)	W / m K
Viscosity at 300$^\circ\text{C}$	3.16 (at 300 $^\circ\text{C}$)	cP
Temperature rise	200	$^\circ\text{C}$
Storage capacity	876 (Short-term) 761 (Long-term)	MJ / m ³
Cost	0.93	$\$/\text{kg}$
Storage cost	10.7	$\$/\text{kWh}$

2.3 Nanofluids

The term “nanofluids” was proposed by Choi in 1995 [52] and stand for stable colloidal suspensions of nanomaterials (particles, fibers, tubes, or droplets) with average sizes smaller than 100 nm in base fluids (or solvents) such as water, oil, ethylene glycol, and recently, molten salts [53]. The concept was developed by Maxwell in 1873, but the idea that particle size is of primary importance in developing stable and highly conductive suspensions is recent. The stability of nanofluids is higher compared to the conventional solvents doped with micro-size particles. Also, hydraulic components/devices such as valves, pumps, seals, etc. are less susceptible to clogging. Thanks to the very large surface-area-to-volume ratio of the nanoparticles, they can be well dispersed in the liquid and enhances the stability of the resulting mixture. On the other hand, the surface properties of nanoparticles have been proven to bring significant changes to various thermo-physical properties of the base fluid, resulting in thermal properties superior to those of the pure fluids and the conventional particle-fluid suspensions [53]. It is important to highlight that despite the numerous recent publications on nanofluids, researchers have not yet reached a consensus on the characteristics of nanofluids, especially on the testing procedure and the reasons why the thermal properties are significantly improved.

2.3.1 Molten Salt-Based Nanofluids (MSBNFs)

Molten salts have become a potential heat transfer and storage medium in CSP plants because of the following advantages: wide temperature range, high heat capacity, low cost, pollution-free. Specific heat is one of the most important thermophysical parameters of molten salts. Its improvement can play a key role in increasing heat storage capacity and reducing the heat storage cost of solar thermal power generation systems. For that reason, many studies have been dedicated to improving the thermal properties of molten salts, especially their thermal conductivity and specific heat capacity.

The production of nanofluids with the addition of solid particles has been of great interest due to the resulting improvement of thermal properties of the molten salt, especially the specific heat capacity and thermal conductivity. Unfortunately, a significant decrease in the specific heat capacity of nanofluids with aqueous solvent has been observed [54]–[57]. For that reason, recent research worldwide are focused on both the improvement of the thermal properties improvement and the

determination of the possible causes of the anomalous increment of these properties for non-aqueous solvents as molten salt.

Within the possibilities of improving the thermophysical characteristics of molten salts used in TES systems, the use of solid particles to improve the heat capacity has been studied by several authors [50], [58]–[71], and silica (SiO_2) has been one of the most reported materials for this purpose [62]–[64], [68], [72], [73]. Seo and Shin [74] used 1 wt.% of silica nanoparticles, 5 nm and 60 nm, to minimize some stability issues by adding them to the ternary eutectic salt $\text{LiNO}_3\text{-NaNO}_3\text{-KNO}_3$. Results showed that the specific heat of the mixture increased between 13 - 16% regardless of particle size, demonstrating that particle size does not have a significant effect on the specific heat, and therefore, particle size cannot be solely responsible for improving the properties of the salt. Andreu-Cabedo et al. [58] demonstrated that with 1 wt.% of silica nanoparticles added to the commercial Solar Salt, a maximum increase of 25.03% can obtain in the specific heat.

Another type of additive used to improve the properties of salts is alumina (Al_2O_3). Ho and Pan [75] showed that the optimum amount added to commercial salt Hitec® to obtain the best properties was 0.063%, which increases the heating capacity of 19.9 %. In this study, it was shown that at higher concentrations of alumina, there is a decrease in the properties of the salt. Schuller et al. [76], on the other hand, proved that there is a parabolic relation between the specific heat and the mass fraction of alumina nanoparticles added to nitrate salts, with a maximum specific heat increase of 30.6 % for 0.78 wt.% of alumina. Other authors have investigated the use of both alumina and silica, as in the case of Chieruzzi et al. [62], who demonstrated that with a ratio between 0.5% and 1.5% of alumina-silica nanoparticles, there is a significant potential to improve the thermal storage characteristics of the binary salt $\text{NaNO}_3\text{-KNO}_3$. Chieruzzi et al. [72], reported an increase in the heat capacity of sodium nitrate up to 9.5 % in solid phase and 6 % in liquid phase after the addition of 1 wt.% of silica, alumina, and a mixture of both nanoparticles. However, the best results were obtained with silica as an additive.

Table 4 summarizes the results of experimental investigations in the literature for molten salt-based nanofluids (MSBNFs). An increment up to 33 % of the specific heat capacity has been obtained using alumina nanoparticles with carbonates as base fluid. On the other hand, Solar salt, one of the most studied, exhibited an increment up to 19.25 % in specific heat capacity by using SiO_2 nanoparticles as an additive and 8.3% with alumina nanoparticles. It must be taken into account that although Hitec

has very good properties at present, there are few reports with this salt as the base fluid [50], [51], in which an increase in the specific heat capacity up to 6.1 % has been achieved.

Due to the few pieces of research about Hitec-based nanofluids and even more with the use of alumina nanoparticles, this doctoral thesis seeks to show the influence of alumina nanoparticles on the thermal properties of Hitec molten salt, namely melting point and heat capacity. The nanofluids were synthesized by the traditional two-step method and a new two-step method developed in this work in which water is replaced by butanol, guaranteeing a suspension of the nanoparticles before they are mixed with the salt and reducing the evaporation time of the solvent. Also, this work provide insights on the corrosive behavior of the developed nanofluids against AISI 304 austenitic stainless steel, a metal commonly used for the manufacture of molten salt containers for thermal storage in the TES system of the CSP plants.

Table 4. Properties of molten salt-based nanofluids: Experimental data from the literature.

Base Fluid	Particle(s)	Size (nm)	Weight Fraction (wt. %)	Melting temperature (°C)	Specific heat Enhancement (%)	Ref.
NaNO ₃	CuO	40	0.054 (2 % vol)	334	-	[77]
	SiO ₂		1.00	-	26	[78]
KNO ₃	CuO	40	0.058 (2 % vol)	306.6	N/A	[77]
	SiO ₂	15-20	0.50, 1.00, 2.00, 4.00	333	7.1, 15.7, 11.4, 2.1	[69]
	SiO ₂	7	1.0	333.7	6.1	[72]
	Al ₂ O ₃	13	1.0	333.3	-7,8	[72]
	SiO ₂ (82-86%) Al ₂ O ₃ (14-18 %)	2-200	1.0	333.9	-3,4	[72]
LiCO ₃ -K ₂ CO ₃ (62-38 mol)	Carbon nanotube	30	0.10, 0.50, 1.00, 5.00	490	5, 9, 12.5, 14.7	[79]
	MgO	10	1.0	-	22	[80]
	SiO ₂	10	1.0	-	27	[59]
	Al ₂ O ₃	10	1.0	-	33	[70]
	Carbon nanotube	30	1.00	480	17	[81]
	Graphite	200	1.00	480	21	[81]
	SiO ₂	10	1.00	488	19-24	[73]
	SiO ₂	27	1.00	378	14.5	[63]
NaNO ₃ -KNO ₃ (60-40)	Al ₂ O ₃	20	0.5, 1.00, 1.50, 2.00	227	1.9, 5.8, 7, 8.3	[61]
	SiO ₂	15-20	1.00	227	8.9	[64]
	SiO ₂	20	1.00	227	17.6	[64]
	SiO ₂	20	1.00	227	-2	[64]
	SiO ₂	25	1.00	-	21.1, 20.3, 9.5, 10.6, 15.82	[82]
	Al ₂ O ₃	10	1.00	220	-14.7	[83]
	Graphene nanoplatelets	5-20	0.10, 0.50, 1.00, 1.50, 2.00, 2.50	-	-15.2, 7.9, 16.7, 9.4, 2.9, 0.7	[84]
	SiO ₂	5, 30	1.00	220	19, 25	[85]

	SiO ₂	25	1.00	-	21.1	[86]
	SiO ₂	10, 20, 30	0.5, 1.0, 1.5, 2.0	215	4.9, 8.4, 7.0, -1.7	[87]
	SiO ₂	15.2	1.00	-	15.01	[88]
	Al ₂ O ₃	40	0.125, 0.25, 0.5, 0.75, 1.00, 1.5, 2.00	-	2.8, 0.7, 2.1, 0.9, 0.3, 1.5, 2.7, 1.7	[76]
NaNO₃-KNO₃ (51-49)	Al ₂ O ₃	13, 50	1.00	222	6, 3	[89]
NaNO₃-KNO₃ (48.2-51.8 mol)	CuO	40	0.056 (2% vol)	223	-	[77]
NaNO₃-Ca(NO₃)₂ (53-47)	SiO ₂	10, 20 30, 60	0.5, 1.0, 1.5, 2.0	127.4	17.8	[90]
NaNO₃-KNO₃-NaNO₂ (7-53-40 mol%)	Al ₂ O ₃	50	0.016, 0.063, 0.125, 0.25, 0.5, 1, 2	-	9.6, 19.9, 12.7, 9.6, 7.8, 6.5, -2.7	[50]

2.3.2 Preparation Methods of Molten Salt-Based Nanofluids

Currently, nanofluids can be produced by one- or two-step methods. One-step methods combine the production and dispersion of the nanoparticles in the base fluid. Direct evaporation [91], and laser ablation are some of the one-step methods. The main advantage of one-step methods is low agglomeration. However, it is not possible to have good control of the nanoparticle size [37], [92].

On the contrary, the two-step method consists of two separate processes/steps. In the first step, nanoparticles, nanofibers, or nanotubes are produced in the form of dry powders. In the second step, the obtained nanomaterial is dispersed in the fluid base with the help of a magnetic stirrer or by ultrasonication. Nanoparticles can be produced by physical or chemical processes. The physical processes include inert-gas condensation and mechanical grinding, while the chemical processes include chemical precipitation, microemulsion, thermal spray, chemical vapor deposition, and spray pyrolysis [53]. **Figure 6** shows the most common two-step method used to produce MSBNFs established by Shin and Banerjee in 2011.

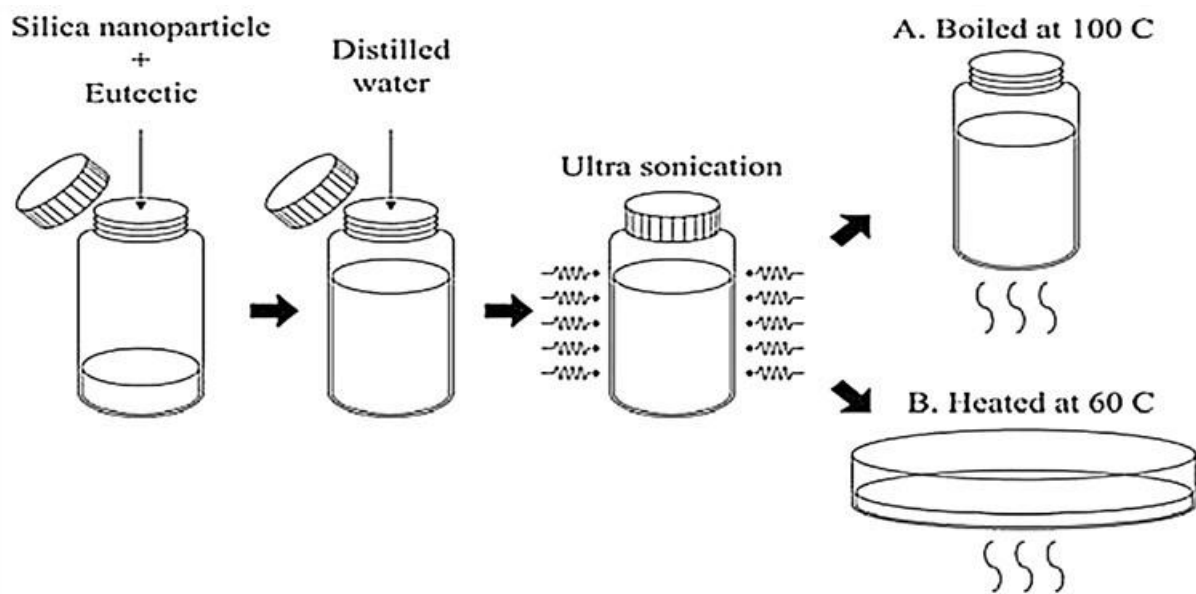


Figure 6. Two-step synthesis of MSBNFs, established by Shin and Banerjee in 2011 [68].

Recent studies are being directed to the development of new methods of preparation of MSBNFs to eliminate the use of water and ensure good thermal properties of the mixture [60], [93], [94]. For example, Chieruzzi *et al.* [60] evaluated the mixtures of 1 wt.% of Silica (SiO_2), alumina (Al_2O_3), or both ($\text{SiO}_2\text{-Al}_2\text{O}_3$) with Solar Salt directly at high temperature using a twin-screw micro-compounder,

and obtained an increment of the specific heat capacity up to 18.6 % for the case of 1 wt.% of $\text{SiO}_2\text{-Al}_2\text{O}_3$. Nevertheless, none of these reports used the commercial salt Hitec as a base salt. On the other hand, Chen *et al.* [94] evaluated the thermophysical properties of $\text{Ca}(\text{NO}_3)_2\text{-KNO}_3\text{-NaNO}_3\text{-LiNO}_3$ molten salt with the addition of the 0.5% of SiO_2 using high-temperature melting and obtaining an increase of 24.5% of the specific heat capacity.

2.4 Thermophysical Properties of Nanofluids

Taking into account the great interest in improving heat transfer, especially in CSP plants, many studies have investigated the different properties of nanofluids. In this way, researches seek to increase the thermal conductivity, and the specific heat capacity, as well as to reduce the viscosity and the corrosive behavior of the molten salt used as a thermal medium, with the overall objective of reducing the Levelized cost of energy (LCOE) and increase the system efficiency. Below are the main characteristics of each of these properties.

2.4.1 Specific Heat Capacity

In order to increase the storage capacity of the TES materials, one of the most important properties that must be enhanced is the specific heat capacity (C_p). Usually, the C_p of molten salts is low. However, using a small amount of the nanoparticles (less than 2 %), the C_p increases up to 33 % [70], depending on the molten salt and the nanoparticle used. This behavior is different for water-based nanofluids; it was reported that the addition of nanoparticles at minute concentrations caused a significant decrease in the overall specific heat capacity [54]–[57]. For that reason, researches have proposed different mechanisms to explain this anomalous behavior in MSBNFs. Shin and Banerjee in 2011 [63] proposed three mechanisms by which the anomalous increase in C_p of MSBNFs can be explained:

- Mode I. Higher specific heat capacity of nanoparticles than the bulk: due to the high energy area per unit mass of the nanoparticle, the specific heat capacity of the nanoparticle is increased when the particle size is reduced.
- Mode II. Solid-Fluid interaction energy: abnormal increase in thermal resistance between nanoparticles and surrounding liquid molecules. This resistance functions as additional storage due to the interfacial interaction of vibrational energies between atoms and interfacial nanoparticle molecules.

- Mode III. “Layering” of liquid molecules at the surface to form a semi-solid layer: the liquid molecules adhered to the surface of the nanoparticles have semi-solid behavior. These semi-solid layers normally have greater properties than those presented by the bulk material contributing to the increase of the specific heat capacity of the nanofluid.

Recently, the functionalization of nanoparticles by the ion-exchange mechanism has been proposed as the cause for the increase in the C_p of nanofluids, but has not yet been listed as a mechanism [95]. The authors have shown that by ion-exchange mechanism the nitrate groups present in the molten salt are adsorbed on the surface of the nanoparticles, regulated by the ion exchange capacity of the nanoparticle. Hence, the C_p of the nanoparticle and the nanofluid increases [95].

Most researchers in this area seek to demonstrate these methods to explain the significant increase of C_p [50], [61], [65], [96]. However, no consensus has been reached on any of these mechanisms and it has not been determined which of them is responsible for the C_p increase or if it is a mixture between them. For the system studied in this thesis, it is established that there is no single mechanism responsible for the increase in C_p of nanofluids, this increase is given by the combination of several mechanisms, that is, there is an influence of the semi-solid layer formed around the nanoparticles due to the temperature gradient between the nanoparticles and the salt, as well as the concentration gradient around the nanoparticles and the possible ionic interaction between the nanoparticles and the molten salt. Similarly, there may be an influence of the interfacial thermal resistance between the nanoparticles and the fluid that becomes larger given the high surface area of the nanoparticles.

2.5 Corrosive Behavior

Corrosion is defined as the deterioration of a material as a result of an electrochemical attack by its surroundings. The lifetime of energy storage plants in CSP can drastically decrease given the corrosion of the tanks in contact with the molten salt. The atmosphere, temperature, as well as the thermal cycling, aggravate the high-temperature oxidation [97]. In this way, nanoparticles are being used not only to increase the thermal properties of molten salts but also to reduce corrosion rates. However, there are few reports about corrosivity of molten salt-based nanofluids [98]–[102], in which the results vary depending on the base salt and the nanoparticles used.

In CSP plants, corrosion involves the dissolution and oxidation reaction of metal alloy. However, only a few metals are appreciably soluble in molten salts used in CSP. The corrosion process involves a reduction and oxidation reaction as listed below:



It is important to highlight that at high temperatures (above 600 °C) corrosion rates are higher, given the presence of oxygen-containing anions resulting from the nitrate reduction reaction, and the oxygen dissolved in the salt [103]. But, a lower temperature molten salts have similar behavior to weak bases as a result of absorption of moisture, stimulating additional pathways for reaction with the metals, and increasing the corrosive nature of these molten salts [104].

Despite the interest in molten salt-based nanofluids to increase efficiencies and reduce the LCOE of CSP plants, few pieces of research report the effect of nanoparticles on the corrosive behavior of salt. However, reports have shown a decrease in corrosion rates and the corrosion layer with the addition of solid particles such as alumina and silica, thanks to the incorporation of nanoparticles within the corrosion layer [101], [102]. Hitherto, the corrosion behavior of Hitec as base fluid with alumina nanoparticles as an additive in austenitic stainless steel 304 has not been evaluated.

3. HYPOTHESIS AND OBJECTIVES OF THIS STUDY

3.1 Hypothesis

Although the number of publications demonstrated the enhancement of thermophysical properties of molten salts by using nanoparticles as an additive, nowadays, a lack of consensus on the effect of nanoparticles on the thermal properties of molten salt-based nanofluids is evident, that is, different levels of enhancement have been reported; hence the mechanism to explain the anomalous increment of these properties have not been thoroughly understood. For that reason, the present doctoral research project aims to contribute to the thermal-fluid sciences and fundamental understanding of Molten Salt-Base Nanofluids (MSBNFs) using molten salt Hitec as fluid and alumina nanoparticles as additive.

Thereby, as hypothesis, it is possible to obtain a thermal- and time-stable suspension of the molten salt-based nanofluid with nitrates-based salts as base fluid and alumina nanoparticles as additive synthesized by a new non-aqueous method, in order to increase its thermal storage capacity by enhanced specific heat capacity (C_p) of the salt, with the aim to increase the CSP system efficiency.

3.2 Objectives

In order to contribute to the understanding of the causes of the improvement of thermophysical properties of molten salts after the addition of solid particles, the main objective of this project is to develop Molten salt Hitec-based nanofluids with alumina as additives and identify the effect of the addition of solid nanoparticles on the thermal storage capacity and the corrosive behavior of nanofluids with potential application as a thermal storage medium in CSP plants.

With the following specific objectives:

1. To design nanofluids with molten salts based on nitrates as the base fluid and alumina nanoparticles as an additive, taking into account the report from literature, their specific heat capacity, melting temperature, and viscosity.
2. To manufacture nanofluids by mixing molten salts based on nitrates and alumina nanoparticles.
3. To determine the thermal stability of the mixtures that showed better behavior concerning the specific heat capacity employing long-term tests in a controlled atmosphere.

4. To establish the corrosivity of the mixture that exhibits the best properties by deliberate exposure to austenitic stainless steel, which is used in thermal solar plants for the fabrication of containers for salts storage.

3.3 Significance of this Study

Currently, there are several reports in the literature confirming the increase in the thermophysical properties of molten salts with the addition of solid nanoparticles. However, few reports refer to nanofluids with Hitec salt as base fluid and alumina nanoparticles as an additive, in addition to the lack of consensus on the rate of increase in these properties and the mechanisms that explain it. Therefore, this work seeks to contribute to the understanding of this system. In this way, the main contributions of this research project to the literature are listed below:

- ✓ A new method for synthesizing molten salt-based nanofluids was designed and evaluated, by replacing the water with butanol, while ensuring a suspension of the nanoparticles and a good homogenization of the system, in order to reduce both, time and cost of the process. The good results of the thermal properties demonstrated the feasibility of this method to be used in the synthesis of nanofluids for thermal storage in CSP plants.
- ✓ A complete characterization of the nanofluids was performed, that is, the measurement of the thermophysical properties, e.g. melting point, specific heat capacity, and thermal stability were evaluated to apply this type of material as fluid for thermal energy storage application.
- ✓ Considering the application to which the nanofluids are aimed to be used, it is of utmost importance to determine their corrosive behavior to ensure their proper operation without affecting the structure, tanks, valves, pipes, among others elements of the plant. In this way, this doctoral project contributes to the study of the corrosive behavior of a nanofluid, based on Hitec and alumina nanoparticles as an additive compared to pure salt; for this, two reactors were designed and manufactured for this purpose. It should be noted that thanks to the size of the reactors, the amount of fluid evaluated, that is, 1000ml, exceeded the amounts normally used in other reports and is a little closer to a prototype plant.

This study aims to explore the effect of alumina nanoparticles in three different concentrations, 0.5, 1.0, 1.5 wt.%, on the thermophysical properties of the commercial molten salt Hitec, synthesized the Molten salt-based nanofluids. Prior reports in the literature showed the different thermal properties of the molten salt using different types of materials as additives. However, almost all reports focused

on the study of nanofluids with binary solar salt as base fluid. Thereby, this investigation contributes to the understanding of the Hitec-alumina nanoparticle system, studying not only the thermal aspects but also the influence of these particles on the corrosive behavior of the salt against an austenitic stainless steel AISI 304, normally used for the manufacture of containers for solar thermal plants.

Thus, nanofluids were fabricated and evaluated employing a newly proposed two-step method. Briefly, water used in the traditional two-step method was replaced by butanol in order to obtain a stable and homogeneous mixture of the alumina before being mixed with the salt. Furthermore, thermal cycling was performed in order to ensure homogenization of the final mixture. Similar to previous reports in the literature on molten salt-based nanofluids, the poor thermal properties of molten salts can be improved by the addition of nanoparticles. The addition of nanoparticles at minute concentration can significantly enhance the specific heat capacity of the molten salt and its thermal stability.

As an important factor, the corrosive behavior of the pure Hitec as a reference was compared to the MSBNF with 1.5 wt% of alumina nanoparticle. For this, two reactors were designed and tuned in order to have controlled temperature and nitrogen atmosphere; additionally, constant mechanical agitation was used in order to ensure the colloidal stability of the nanofluid for up to 2000h. The decrease in the corrosivity of the salt thanks to the embedding of the nanoparticles in the corrosion layer was demonstrated.

Thanks to the thermal properties obtained, the proposed new two-step method was demonstrated as a successful approach for the synthesis of molten salt-based nanofluids for thermal application in CSP plants. In the same way, an improvement of the corrosive character of the salt was evidenced after the addition of the solid particles, which proves that these nanofluids can be used as a storage medium in solar thermal plants without great damage to the system. All of the above can contribute to reducing the LCOE of technology, allowing it to be more competitive compared to traditional energy sources.

4 EXPERIMENTAL METHODS

In order to evaluate the properties of the Molten Salt-Based Nanofluids (MSBNFs) developed in this work, the eutectic commercial salt Hitec (7 wt% NaNO_3 -53 wt.% KNO_3 -40 wt.% NaNO_2) was selected as a reference and base fluid and commercial alumina with a nominal size of 13.6 nm as additive. Three different concentrations of alumina nanoparticle were evaluated, namely 0.5, 1.0, and 1.5 wt.%. The methodology flow chart is shown in *Figure 7*. Alumina nanoparticles were selected to be the additive for MSBNFs with Hitec commercial molten salt as base fluid, thanks to the good thermal properties such as high melting point and thermal conductivity, and good stability at high temperature, and considering the literature [50], [70], [75], [76], [105] where the alumina is used as an additive, especially with Nitrate-nitrate molten salt as base fluid. Two different methods to fabricate MSBNFs were evaluated to select the most appropriate method. The traditional two-step method developed by Shin and Banerjee in 2011 [106] was compared to a new two-step method developed in this thesis, in which deionized water was replaced by butanol to ensure a homogeneous suspension of nanoparticles before mixing it with molten salt and ending with 4 or 5 thermal cycles in order to obtain a homogeneous nanofluid. Subsequently, thermophysical properties, specifically the melting temperature, specific heat capacity, and thermal decomposition, were validated and compared to the reference to select the method that produces nanofluids with the best properties. Finally, the corrosive behavior of the MSBNF with high specific heat capacity was evaluated in a reactor specially designed to assess the influence of nanoparticles on the corrosion of stainless steel. Three different heights inside the reactor were used, at the bottom of the reactor to evaluate the precipitated nanoparticles, at medium position to evaluate the nanofluids, and partially submerged to assess, not only the nanofluids, but also the possible releases of gases by the molten salt.

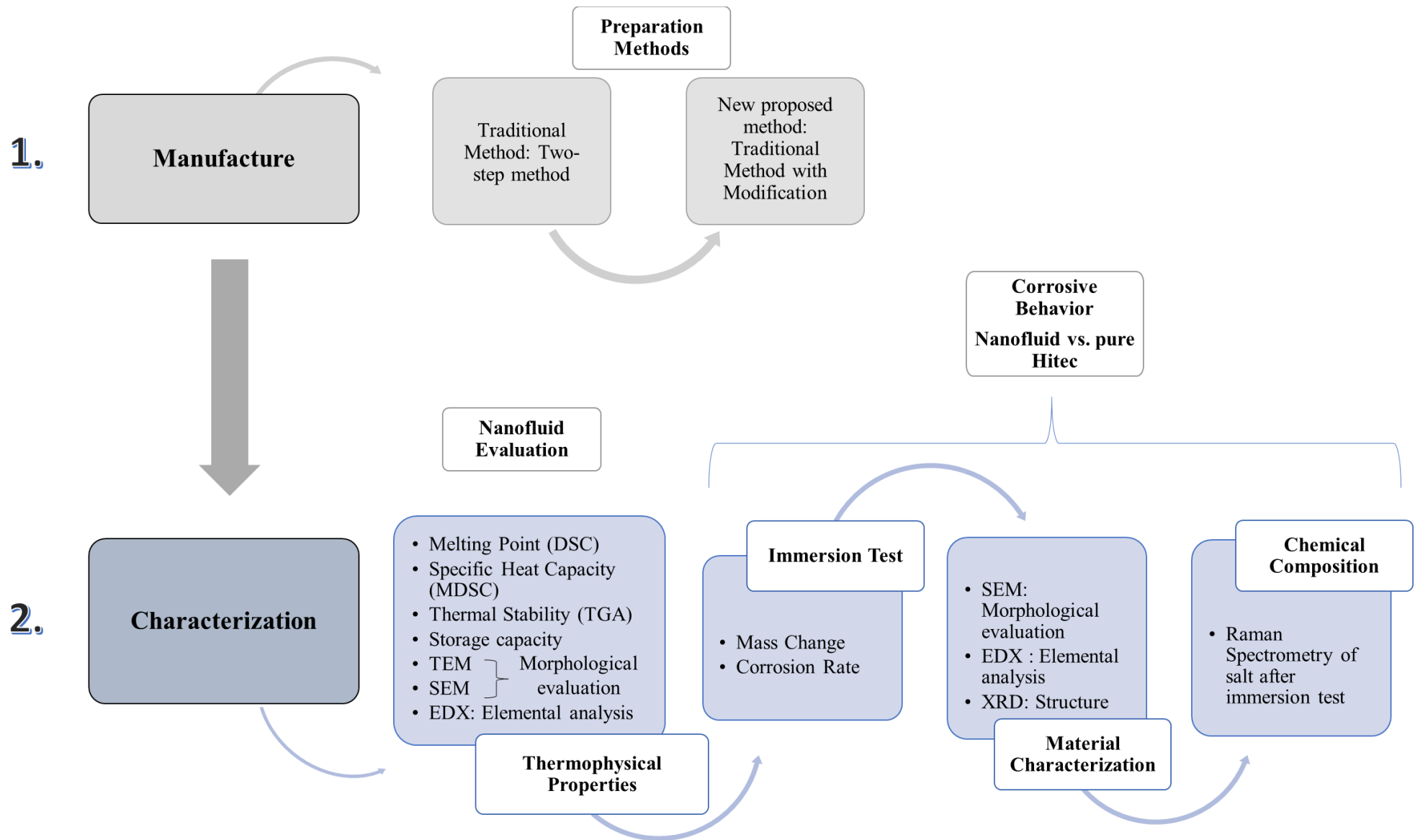


Figure 7. Methodology flow chart of molten salt-based nanofluids studied.

4.1 Preparation method of Molten Salt-Base Nanofluids

As mentioned above, there are different types of methods to prepare the nanofluids. The traditional method used was established by Shin and Banerjee in 2011 [106]. This method can be expensive at large scale, since it uses large amounts of water, which could be detrimental to the salt stability. Taking into account that the preparation method is an important factor to obtain good properties of nanofluids and intending to reduce energetic costs and synthesis time [89], researchers focus on obtaining nanofluids based on molten salts by alternative methods decreasing or eliminating the use of water without affecting the thermophysical properties of the mixture [60], [93]. Hence, in this research, the traditional two-step method was compared with a new two-step method proposed in which the water was replaced by butanol. Three different percentages of alumina nanoparticles (0.5, 1.0, and 1.5 wt.%) were used to elaborate the MSBNFs with both methods.

4.1.1 Preparation of the molten salt

The salt mixture was prepared in the laboratory from pure high-grade chemicals according to the known formulations Hitec (7 wt. % NaNO_3 -53 wt. % KNO_3 -40 wt. % NaNO_2). The nitrite and nitrate salts used were NaNO_2 , NaNO_3 , and KNO_3 (98 %) Reagent Grade purchased from Merck. Pure salts contain different levels of impurities, primarily consisting of chloride, magnesium, and sulfate. The level of impurities in the salts according to the salt provider is given in **Table 5**.

Table 5. The reported level of impurities in the nitrate/nitrite salts.

Pure salt	Amount (wt. %)				
	Chloride (Cl ⁻)	Magnesium (Mg ²⁺)	Sulfate (SO ₄ ²⁻)	Insoluble	Moisture
NaNO₂	<0.01	<0.01	0.01	<0.025	<0.05
NaNO₃	<0.05	<0.005	<0.01	<0.025	0.1
KNO₃	<0.002	<0.005	<0.01	<0.025	0.05

In the beginning, the salt mixtures were carefully prepared in an agate mortar for around 20 min under atmospheric conditions according to the proportion described above. After that, the mixture was heated in a Nabertherm LT 9/12/P330 muffle furnace until the melting point (~160°C) in a quartz

vessel for around 1 h, and the temperature was raised to 270°C for 48 h to eliminate the presence of moisture. Later, the mixture was cooled faster in a stainless steel container submerged in cold water, distributing it homogeneously at the bottom in such a way that there was a layer of ca. 5 mm thick, fast cooling it until the salt was completely solid.

4.1.2 Traditional Method: Two-step method

In order to produce molten salt-based nanofluids, the traditional method designed by Shin et Banerjee in 2011, was used as seen in **Figure 8**. Sodium nitrate, sodium nitrite, and potassium (7:53:40 weight ratio) and the alumina (Al_2O_3) nanoparticles were weighed in a Mettler Toledo AB204 Analytical Balance and mixed in a mortar for about 15 min until the obtaining of a visibly homogeneous mixture. The total mass of the mixture was 10 g. Next, the mixture was repackaged in a glass beaker and completely dissolved in 30 ml of deionized, then it was ultrasonicated for 3 hours to ensure good homogenization and a colloidal suspension (nanofluid). After that, the nanofluid was transferred to a hot plate at 120°C for evaporating the water from the mixture for around 14 hours. Finally, the nanofluid was heated at 160°C for around 4 hours to ensure a mixture completely melted and homogenous, followed by a rapid cooling to try to preserve the structure of the salt in the molten state and not allow time for the formation of new structures. After that, the samples were ground in a mortar before characterization, and stored in resealable bags inside a desiccator in order to avoid moisture ingress. **Figure 9** presents the MSBNF before and after the fusion.

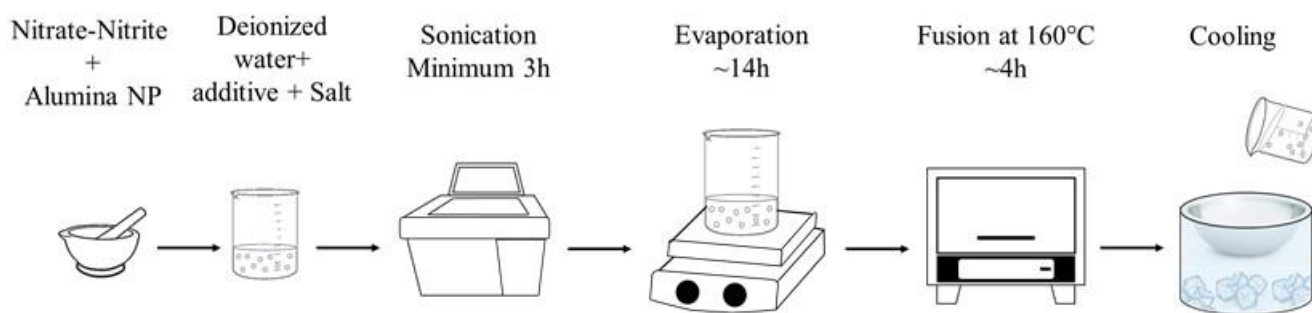


Figure 8. The traditional method to develop Molten Salt-Based Nanofluids.

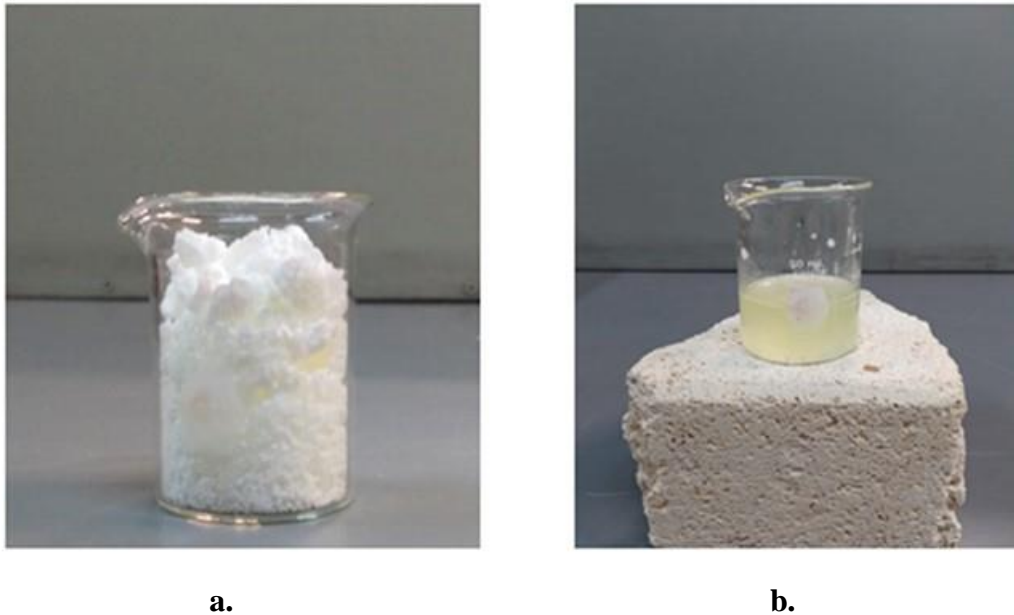


Figure 9. Molten salt-based nanofluid a. before and b. after fusion.

4.1.3 The proposed new method: Traditional Method with Modification

Molten salt-based nanofluids were also produced following a modification of the traditional method by using butanol instead of water, with the aim to ensure a homogeneous and colloidal suspension of the nanoparticles before mixing with the molten salt. Considering that the alumina nanoparticles form stable suspensions in slightly polar solvents as 1- butanol [107], ensuring the homogeneous suspension of the nanoparticles first in the butanol, it is possible to obtain a homogeneous distribution of them after the addition of the molten salt. Once the salt is obtained by the procedure established above, the mixture was homogenized using an agate mortar for 15 minutes. The homogeneous powder was mixed with the nanoparticles (0.5, 1.0, and 1.5 wt.%), which were previously mixed with 10ml of butanol, and forming a stable suspension sonicated continuously for at least 1 hour. After that, the mixture was subjected to a cycling process between 160 and 270°C at least 2 times, and fast cooling in a stainless steel container submerged in cold water to ensure the structure of the salt in the molten state and not allow time for the formation of new structures. After that, the samples were ground in a mortar to obtain powder and guarantee their homogeneity, and stored in resealable bags inside a desiccator in order to avoid moisture ingress. DSC, TGA, and rheometry were carried out to characterize pure Hitec and the MSBNFs. The preparation of MSBNFs is schematized in *Figure 10*.

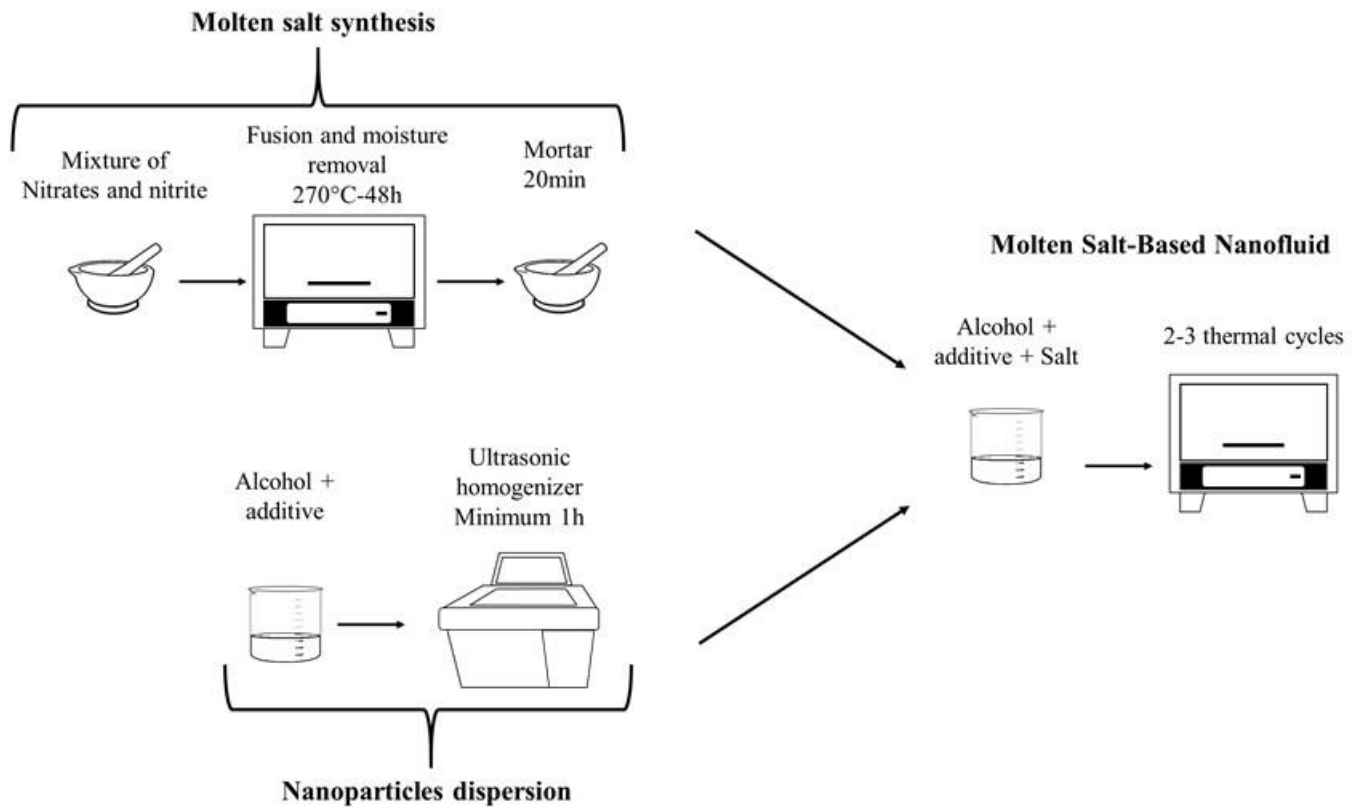


Figure 10. The new proposed method, traditional method modify to prepare the Molten Salt-Base Nanofluids.

4.2 Thermophysical Properties Determination

4.2.1 Sampling process

1. After the synthesis process, the samples are stored in resealable bags in a desiccator, in order to avoid the entry of moisture.
2. When performing the characterization by the different techniques used, DSC, MDSC, TGA, Raman, XRD and SEM; the sample is removed from the desiccator and the required quantity is immediately selected. The selection is carried out randomly, always taking from different areas of the sample for each measure.
3. Finally, after selecting the sample for characterization, it is re-stored in the desiccator.

Note: In case of requiring transfer from one place to another, the samples stored inside the resealable bag were placed in an airtight container with silica gel inside, seeking to avoid the entry of moisture.

4.2.2 Thermal Analysis

The experimental conditions to realize the thermal analyses such as differential scanning calorimetry (DSC), modulated differential scanning calorimetry (MDSC), and the thermogravimetric analysis (TGA) were as follows:

4.2.2.1 Differential Scanning Calorimetry

The melting point was measured using a differential scanning calorimetry (DSC; Q200, TA Instrument, Inc.). Tzero hermetic pan/lid aluminum (TA instruments) was used to place the samples in the DSC and analyzed by TA Universal Analyzer 2000 version 4.5A. The sample mass was around 10 mg for all samples. The thermal cycle was realized in a nitrogen atmosphere, starting at room temperature until 400°C at a rate of 10 °C / min, followed by equilibration at 40°C. The test had a sampling interval of 0.10 s / pt, and 2 cycles were realized to obtain a homogeneous result. The melting temperature of the sample was taken as the main endothermic peak in the DSC curve.

4.2.2.2 Modulated Differential Scanning Calorimetry

Differential scanning calorimetry (DSC) is the most used procedure for determining the specific heat capacity of the nanofluids and other types of material for thermal energy storage. ASTM E1269 establishes that the heat capacity should be measured by Differential Scanning Calorimetry (DSC) [108]. According to this standard, a sample measurement is comprised of three separate measurements: a baseline, a sapphire, and the sample. Finally, the determination of the heat capacity value is done by comparison between the power to heat the sample and the power to heat a known reference, usually sapphire. On the other hand, an alternative method to find the specific heat of a sample has been developed, using the Modulated Differential Scanning Calorimetry (MDSC) following the standard ASTM E2716 [109]. By this method, two simultaneous heating rates are applied to the sample, a linear heating rate where the total heat flow is analogous with the conventional DSC, and a second sinusoidal heating rate that allows the direct calculation of the specific heat capacity of the sample, allowing to have greater sensitivity to small changes in the sample, especially in non-homogeneous samples such as nanofluids.

Modulated differential scanning calorimeter (MDSC; Q200, TA Instrument, Inc.) was used to estimate the specific heat capacity of the samples, using aluminum crucibles and N₂ atmosphere. The

samples were heated up to 250°C and held at this temperature for 5 min to obtain a stable heat flux signal, after that, the applied amplitude was ± 0.50 °C every 130 s, and finally was heated again until 350 °C at 2 °C / min. The specific heat capacity was reported for both methods at 300 °C, since this is the temperature at which the salt in Parabolic Trough Plants is commonly maintained. The reference used was standard sapphire. Several factors can influence the results of the measurement, including heating rate and sample size. In order to assess the influence of the latter, DSC measurements were performed using different weights of samples, 5, 10, 20, and 30 mg, it was established that 10 mg of sample was the adequate weight to obtain homogeneous and reproducible results. Peak analysis was performed using the Universal Analysis 2000 version 4.5A. These procedures were applied to measure the specific heat capacity of every sample, pure samples, and mixtures.

4.2.2.3 Thermogravimetric Analysis

The thermal stability of pure Hitec and the MSBNFs were determined by thermogravimetric analysis (TGA; Q500, TA Instrument, Inc.) under a constant stream of nitrogen at a flow rate of 50 ml/min, temperature ramp of 15°C / min in the range 25-800°C and isothermal for 5 min.

4.3 Raman Spectrometry

Raman spectra were obtained with a Horiba Jobin Yvon Labram HR spectrometer equipped with a He- Ne laser (0.10 mW, 632 nm) and CCD matrix detector (1024×256 pixels), to evaluate the chemical stability of the both pure Hitec and MSBNF with 1.5% Al₂O₃, submitted to the corrosive behavior test at 550 °C during 24, 48, 76, 97, 336, 432, 500, 668, 720, 864, 1663, 1932, and 2000 h. Raman spectra were collected over the range 50-2000 cm⁻¹, and each spectrum resulted from a single scan, corresponding to a total collection time per spectrum of 20 s. Taking into account the heterogeneous nature of the sample nature, for both pure salt and the nanofluid, several spots on each sample were measured.

4.4 Corrosive Behavior of Molten Salt-Based Nanofluids with Container Materials

Given that the thermal energy storage system is an important part of the CSP plants, it is essential to investigate the susceptibility of the container materials in contact with the molten salt, taking into account that the corrosion decreases the plant life, and it can be aggravated by thermal cycling at high

temperature [4]. Hence, the corrosive behavior test of both pure Hitec and the MSBNF with high specific heat capacity was realized at 550 °C under a controlled atmosphere of N₂ to evaluate the interaction between the metal surface and the MSBNF. This procedure was focused on the corrosion products on the surface, the corrosion rate of the metal alloy, and the stability under the time that MSBNFs were evaluated.

4.4.1 Corrosive Behavior Test

It is necessary to take into account that the materials used to contain the storage fluid must maintain both their structural integrity and their mechanical properties at the working temperature of solar thermal plants. The most widely used metals are stainless steels, such as AISI 304, AISI 316 among others, thanks to their low cost compared to other steels and alloys [110], as well as their thermo-physical and mechanical properties. Among the stainless steels, AISI 304 stands out as one of the most used together with P91. AISI 304 was used in the Solar Two Plant in Daggett (California), for the hot tank and the parts in contact with the molten salt at high temperatures (565°C) [111], [112]. On the other hand, there are reports that highlight that steels with a high Cr content, such as AISI 304 stainless steel, can be used in systems such as pipes and molten salt storage tanks, which operate at temperatures close to the 570°C [113]. In line with this information, stainless austenitic steel AISI 304 (SS304) was selected to evaluate the corrosion behavior inside both the molten salt Hitec and the MSBNFs; **Table 6** shows the specification of the AISI 304 according to ASTM A240 [114]. Rectangular samples with initial dimensions of 25 mm×10 mm×1 mm and a 3 mm diameter hole for gripping the sample holder, were analyzed via gravimetric measurements. Then, the samples were grinded with SiC abrasive paper, degreased in alcohol, and dried in the air, to ensure a homogeneous surface without impurities. After that, they were placed in two reactors especially designed for this purpose, the first one with Hitec pure as fluid and the second one with the MSBNF with the enhanced thermophysical properties, specifically the specific heat capacity. Three different heights inside the reactor were evaluated to estimate the influence of the presence of nanoparticles. At the bottom of the reactor to estimate the influence of the precipitation of the nanoparticles, at medium position to evaluate the nanofluid, and partially submerged to evaluate, not only the nanofluid, but also the possible gases released by the molten salt. **Figure 11** shows the reactors, the sample holder with the three heights evaluated, and the samples used to estimate the corrosion behavior. The long-term test was realized during 24, 48, 72, 168, 240, 360, 500, 672, 840, 1000, 1500, and 2000 h, in which the

samples were removed from the reactor, slowly cooled in warm distilled water and then, dried and weighted. For every height evaluated (Bottom, medium, and top) three samples were removed at every time of measurement. Finally, the average value was computed from five weights, and the mass gain overtime was calculated according to *Equation 4*; where m_i is the initial mass of the sample, m_f is the mass of the sample at the selected time and S_o is the initial area of the sample.

$$\frac{\Delta m}{S_0} = \frac{m_i - m_f}{S_o} \quad \text{Equation 4}$$

Table 6. Chemical composition of the studied AISI 304 alloy according to ASTM A240.

Alloy	C	Mn	S	P	Si	Cr	Ni	N
SS 304	<0.07	<2	<0.03	<0.045	<0.75	17.5-19.5	8-10.5	0.10
Sample	0.026	1.49	0.012	0.037	0.27	18.6	8.4	-

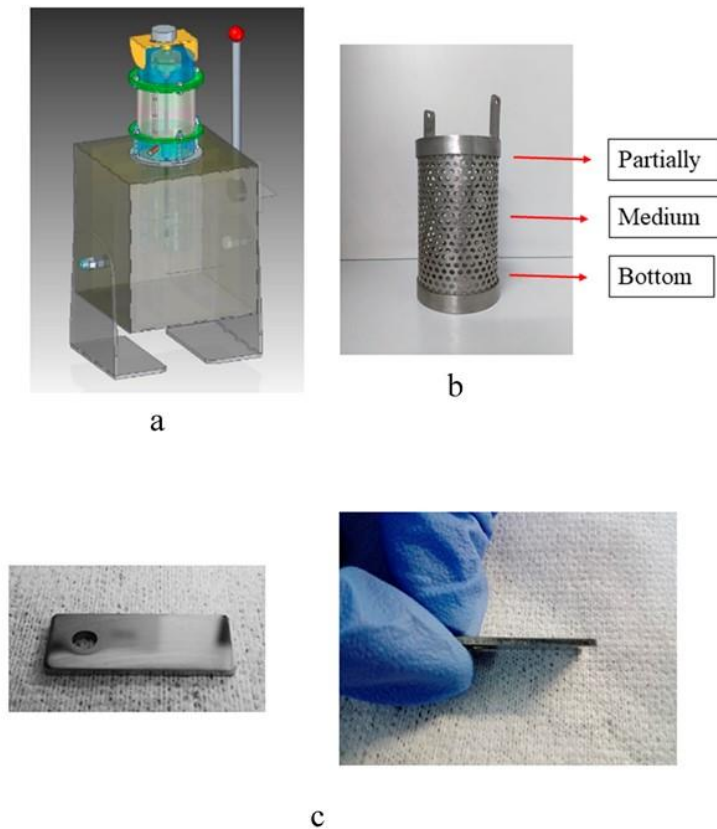


Figure 11. Image of a. Reactors designed to evaluate the corrosion behavior in this work, b. samples holder with three different positions inside the reactor and c. Stainless Steel AISI 304 samples.

In order to determine the corrosion rate, the ASTM G1-03 standard was used [115]. Hence, HNO₃ solution was used to remove the corrosion products of SS304 samples by immersion, which were further cleaned by light brushing several times. Subsequently, the mass loss was determined after each cleaning by weighing the samples. Finally, from the norm [115] the *Equation 5* was used to calculate the corrosion rate, where K is a constant (8.76x10⁴ mm / y); W is the mass loss of the sample in grams, A is the sample area in cm²; T is the exposure time in hours, and D is the density of the stainless austenitic steel AISI 304 (7.94 g / cm³).

$$\text{Corrosion rate} = \frac{(K.W)}{(A.T.D)} \quad \text{Equation 5}$$

It is important to highlight that after the process described above, SS304 samples were stored in resealable bags with nitrogen injection prior to closing, in order to displace the presence of oxygen and prevent it from continuing to attack the surface of the samples, before being characterized by XRD. In this way, the phases identified by XRD would correspond to those obtained by the immersion process in salt and nanofluid.

4.4.2 Characterization Techniques

The scanning electron microscopy (SEM) and the X-ray diffraction (XRD) was performed in order to analyze the morphology of the SS304 samples in contact with pure Hitec and MSBNFs, as well as to determine the corrosion products after the long test.

4.4.2.1 Transmission electron microscopy TEM

The size and shape of alumina nanoparticles used to elaborate the MSBNF were observed by electron transmission microscope, TEM (Tecnai F20 Super Twin TMP), using a source of emission of fields, resolution of 0.1 nm in 200 Kv. Taking into account the low solubility of alumina in butanol, the particles were dispersed in it, then an aliquot was placed on a copper grid (Lacey carbon mesh 200) and heated long enough to ensure the solvent elimination.

4.4.2.2 Scanning Electron Microscopy (SEM)

The samples were fixed on a graphite tape, covered with a thin gold coating (DENTON VACUUM Desk IV equipment) and analyzed in the high vacuum scanning electron microscope (JEOL JSM 6490 LV) to obtain high-resolution images. The detector of secondary electrons was used to evaluate the morphology and topography of the samples. The elemental analysis was carried out by energy-dispersive X-ray spectroscopy EDS (reference INCA PentaFETx3 Oxford Instruments).

SEM images were carried out after the MDSC measurement to verify the presence of the nanoparticles inside of the molten salt as well as to evaluate the agglomeration. On the other hand, the same technique was used to evaluate the morphology structure of the SS304 used to estimate the corrosive behavior of Hitec and MSBNF with 1.5 wt.% of Al₂O₃ under corrosive behavior test.

4.4.2.3 X-Ray Diffraction (XRD)

An X'Pert PRO MPD X-ray diffractometer with Co and Cu K α radiation source was used, the data were recorded over the 2 theta range of 10-90° to analyze the corrosion products formed in the SS304 at 550°C after 672 h of testing, as well as the corrosion products inside the molten salt after 2000 h of the corrosive behavior test. Rietveld refinement analysis was performed on the XRD patterns and compared to the references and standards found in HighScore Plus software from PANalytical version 3.0.

5 EXPERIMENTAL RESULTS

In order to evaluate the effect of nanoparticles on the thermophysical properties of the molten salt, that is, Molten Salt-Based Nanofluids (MSBNFs) developed in this work, the eutectic commercial molten salt Hitec (7 wt. %NaNO₃-53wt. %KNO₃-40wt. %NaNO₂) was selected as a reference and the base fluid and compared with the results of the MSBNFs with alumina nanoparticles in three different proportion, 0.5, 1.0 and 1.5 wt. %, with a nominal size of 13.6 nm. Hence, this section shows the characterization of both pure Hitec and the MSBNFs, as well as the characterization of the pristine alumina nanoparticles.

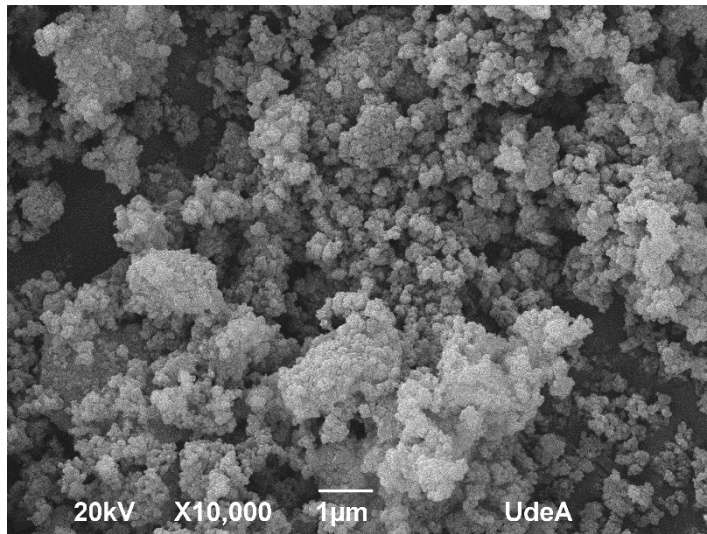
5.1 Characterization of alumina nanoparticles

Consider the significant properties of the alpha-alumina such as high melting point and thermal conductivity, good resistance to thermal impact and chemical stability and chemical stability, alpha-alumina was selected as an additive to synthesize the MSBNFs. Thus, characterization by SEM, TEM, TGA, MDSC and DRX was performed to establish the size distribution, shape, thermal, and chemical stability of the alumina used for the synthesis of the MSBNFs with the traditional two-step method and the new two-step method proposed.

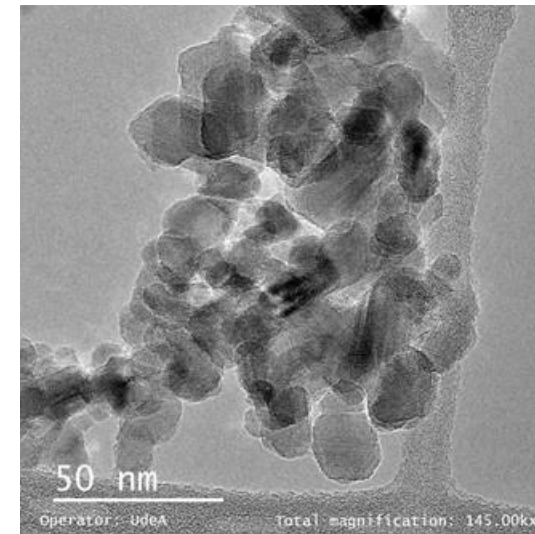
5.1.1 Morphology of Alumina

Figure 12 a and *b* shows the SEM and TEM images of the pristine alumina nanoparticles used to elaborate the MSBNFs, respectively, as well as,

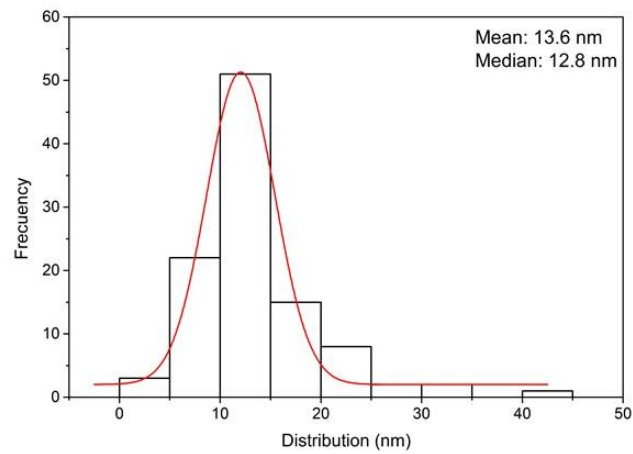
Figure 12 c and *d*, the size distribution with an average size of 13.6 nm which is even smaller than that reported by the supplier of 40 nm, and the EDX obtained from TEM where it is evident that the nanoparticles are composed only of Al₂O₃. The regular shape can be observed in the SEM and TEM images, as well as the presence of agglomerates, which can be eliminated or reduced during the MSBNFs synthesis process. The shape of the alumina is characteristic of alpha alumina, as other authors have reported [116], [117].



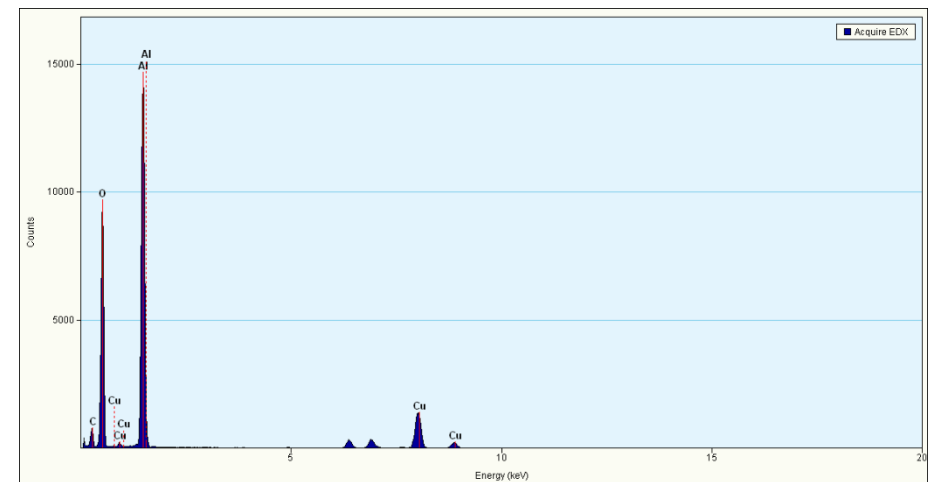
a.



b.



c.



d.

Figure 12. Morphological features of pristine alumina nanoparticles used to elaborate the MSBNFs. a. SEM image, b. TEM image and c. the size distribution obtained from TEM image.

5.1.2 Thermal properties

Considering the differences between the properties of materials in bulk compared with the nanoparticles and taking into account the significant increase in the thermal properties of salts with the addition of solid particles with a size smaller than 100 nm demonstrated by various authors in the literature, the thermal properties of the nanoparticles used for the synthesis of nanofluids in this thesis are reported. **Table 7** shows the comparison of the specific heat capacity of the nanoparticles with 13.6 nm size used in this investigation with the reported in the literature, as well as the Cp for the bulk alumina. The reduction of the Cp in the nanoparticles is evident compared with the bulk alumina as other authors have been informed [53], [89]. The difference in Cp value obtained experimentally compared to that reported by some authors for alumina nanoparticles of the same size may be due to the crystallinity of the material, that is, the presence of the three phases of alpha, beta, and gamma-alumina, as well as the shape of the particles [89].

Table 7. Specific Heat capacity of alumina nanoparticles and bulk.

Size	Specific Heat Capacity (J/g°C)	Reference
13.6 nm	0.79 (at 300°C)	Experimental
13nm	0.814 (at 310°C)	[89]
Bulk	1,09 (at 223°C)	[77]
	1,14 (at 306,5 °C)	
	1,16 (at 334°C)	

On the other hand, it is important to consider other thermal properties such as the melting point to ensure that the particles remain solid at the operating temperatures of the salts. **Table 8** reports the melting point of the alpha-alumina at 2050°C and higher, showing that this material can withstand the working temperatures in CSP plants: 550°C for Parabolic Trough Collectors and 770°C for Parabolic Dishes

Table 8. Thermal properties of bulk alumina from literature.

Property	Value	Reference
Melting Point (°C)	2050 2072	[118]
Thermal conductivity (W/mK)	36,3 (at 25°C) 20,4 (at 223°C) 16,7 (at 306,5 °C) 15,6 (at 334°C) 30 25	[77], [119]
Density (g/cm ³)	3.97 (at 223°C) 3.96 (at 306,5°C) 3.96 (at 334°C)	[72], [77]

Through the TGA shown in

Figure 13, the thermal stability of the alumina nanoparticles was confirmed; below 150°C, the weight loss was attributed to the elimination of physically adsorbed water [120]. After this temperature, the sample is stable up to 1300°C without presenting other significant losses of mass as reported by other authors [121]. This result indicates that alumina will be stable during the nanofluid synthesis process, in which the maximum temperature is 270°C, and during its use in the corrosive behavior test with a holding temperature of 550°C.

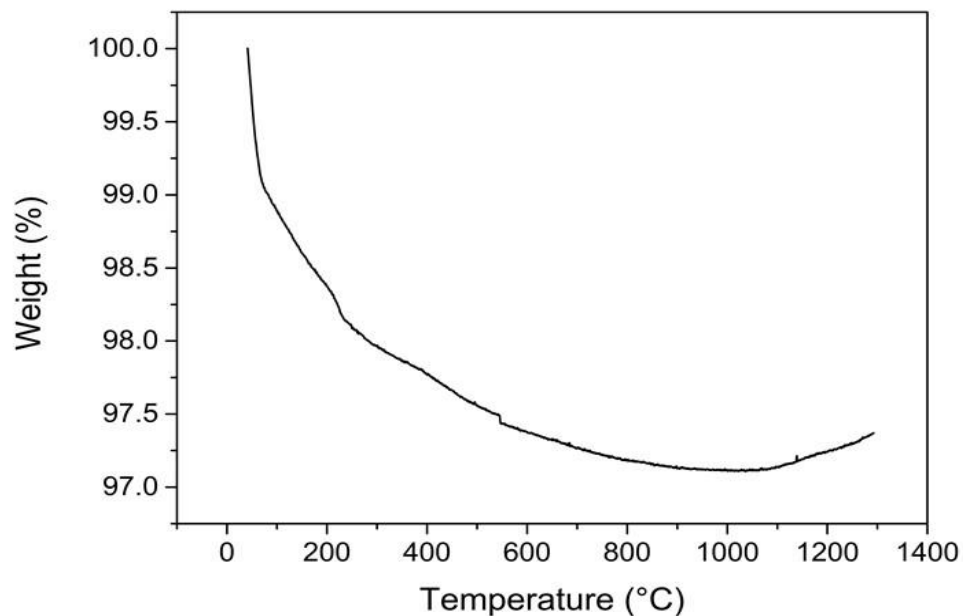
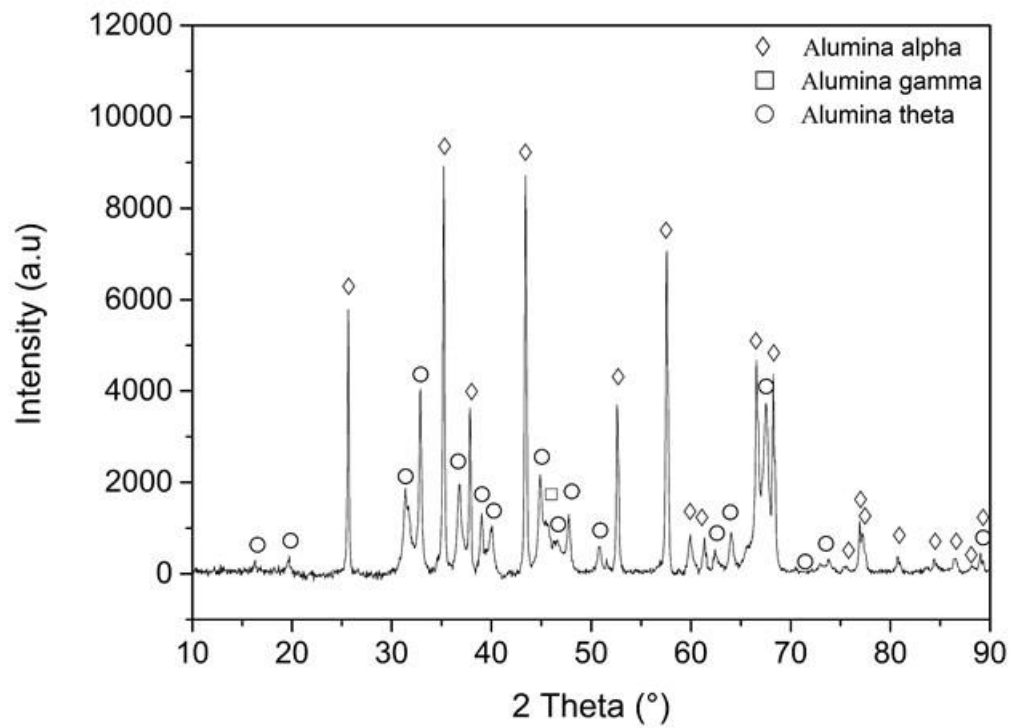


Figure 13. TGA of pristine alumina nanoparticles.

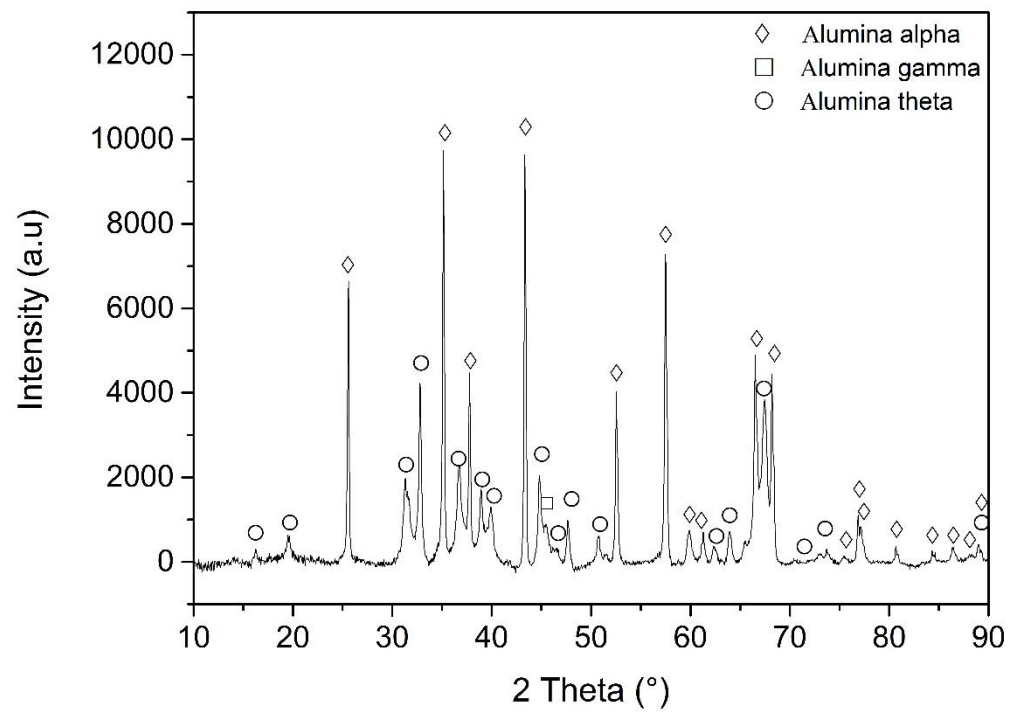
5.1.3 Composition and Structure by XRD

In order to establish the chemical stability of alumina nanoparticles, the XRD pattern shown in **Figure 14** was established for two different samples, the first one shown in the left the of figure presents the XRD result of the pristine alumina used to synthesize the MSBNFs in this research, and the second one in the right of **Figure 14**, shows the result for the alumina calcined during 6 hours at 600°C, this temperature was selected considering the maximum temperature used in CSP plants and the temperature selected to evaluate the corrosive behavior test reported later, i.e., 550°C. In both diffractograms, the presence of the same phases of alumina, alpha, gamma, and theta was found in the same positions, thus, the chemical stability of the nanoparticles can be ensured as there are no appreciable changes in the structure of the sample after calcination.

Despite the supplier of the alumina nanoparticles reported the composition of nanoparticles with only alpha alumina, the DRX results confirmed that it is a mixture of the three mentioned phases, alpha, gamma, and theta, the presence of these different phases of alumina can be related to factors such as the characteristics of the starting material (degree of crystallinity, impurities, alkaline) and the thermal cycle used to obtain the alpha-alumina. However, it is known that all of these phases are very stable both thermally and chemically, especially at the working temperature of the salts in the plant, that is, less than 600°C [122]. Although in the research with alumina nanoparticles used in the synthesis of nanofluids, the alumina phase is not reported, the improvement of the thermophysical properties with alumina gamma in the nanofluids has been reported [123], [124]. Likewise, the different phases may affect the thermophysical properties of different proportions compared to other authors, as indicated by Nithiyantham *et al.* [89].



a.



b.

Figure 14. The XRD pattern of **a.** pristine alumina and **b.** calcined alumina.

5.2 Thermophysical properties of Hitec and the MSBNFs

The melting temperature, specific heat capacity and the thermal stability were assessed by DSC, MDSC and TGA, respectively; these thermal analyses are presented in this section. Also, the calculation of the storage capacity and the SEM evaluation after the specific heat capacity determination are shown in this section.

5.2.1 Melting Temperature (T_m)

The melting temperature values of the pure Hitec and the MSBNFs were obtained by DSC. Two heating and cooling runs were performed to avoid discrepancies in the melting temperature produced by the hygroscopic nature of some nitrates. The first cycle was performed to achieve the perfect mixing of the mixture, and the results from this sequence were not taken into account. The second cycle was analyzed, and the data from these runs are reported in **Figure 16**. The first transition is related to the solid-state phase transition α/β associated with the KNO_3 eutectoid [125], and the second endothermic peak corresponds to the melting temperature.

Given that both, the base molten salt (Hitec) and the nanofluids with the different proportions of the alumina nanoparticles, are not pure materials, and considering previous reports by Gimenez and Fereres [126] and Mohammad *et al.* [127], the heating rate affects the onset of melting as well as the peaks height, peaks width, and transition enthalpies. Therefore, the melting temperature of the sample was taken as the endset temperature of the main endothermic peak at the DSC curve [41]. Thereby, the melting point related to the Hitec salt was 145.38°C and the endset point was obtained at 149.83°C , slightly higher than reported in the literature [40], [43], [47]. This behavior may be related to the preparation of salt in the laboratory without atmospheric control during the fusion process, that is, the fusion was performed under an air atmosphere. As indicated by Olivares [128] the use of air during fusion can change the composition of the initial mixture after oxidizing part of the nitrite to nitrate raising the melting point.

The effect of the Alumina nanoparticles aimed at lowering the melting point of Hitec salt is shown in **Table 9** and **Figure 16**, where the results are presented for both the traditional two-step method (TM) and the new two-step method (NM), with the three proportions of nanoparticles, 0.5, 1.0, and 1.5 wt.% of Al_2O_3 nanoparticles. The addition of Alumina led to an apparent reduction of the onset,

endset, and melting point temperature. This effect was found for all samples investigated, but it was more evident for the new two-step method up to 4.93 % with 1.0 wt.% of nanoparticles compared to the base salt mixture. This behavior corresponds to the reports of several authors [62] in which the thermal properties of the molten salt have higher enhancement with 1.0 wt.% of Al_2O_3 , and with a greater amount of nanoparticles the thermal properties begin to be affected negatively. In particular, the onset temperature decreased by adding Al_2O_3 . This performance means that the phase change occurred at a lower temperature in comparison to the base salt; this behavior is a clear advantage for the use of the MSBNFs in CSP plants. On the contrary, with the traditional two-step method, the sample presented lower melting points between 1.5 wt.% and 4.08 % of Al_2O_3 , contrary to what has been reported in the literature. However, taking into account the standard deviation of all samples evaluated, **Figure 15**, there was no statistically significant difference in the decrease of the melting point, which means that the samples exhibited a similar decrease regardless of the proportion of nanoparticles and the method of synthesis used.

Few pieces of research have been reported for the variation of the melting point of salt with the addition of nanoparticles, and none of them used Hitec as the base fluid. Habitually, the researchers focus on other properties, like thermal conductivity and specific heat capacity. However, using the same type of nanoparticles, Nithiyantham *et al.* [89] reported a decrease of ca. 1°C for the melting temperature after the addition of 1 wt.% of Al_2O_3 in the binary Solar salt. On the other hand, Chieruzzi *et al.* [62] showed a decrease of less than 1 % of the melting temperature for the molten salt after the addition of alumina nanoparticles.

Table 9 The melting point of pure Hitec and MSBNFs.

Sample	Melting Point (°C)	Change Percentage (%)	Standard Deviation	Onset (°C)	Endset (°C)	Heat of Fusion (J/g)
Hitec (H)	145.38	-	0.53	139.36	149.83	85.43
H+0.5% Al ₂ O ₃ -TM	140.25	-3.53	0.84	131.52	146.50	78.76
H+1.0% Al ₂ O ₃ -TM	139.54	-4.01	1.03	129.55	129.81	71.69
H+1.5% Al ₂ O ₃ -TM	139.45	-4.08	1.20	129.81	145.95	71.81
H+0.5% Al ₂ O ₃ -NM	138.98	-4.40	1.41	128.62	144.99	70.40
H+1.0% Al ₂ O ₃ -NM	138.71	-4.93	0.25	127.42	144.50	68.42
H+1.5% Al ₂ O ₃ -NM	139.27	-4.21	0.69	131.75	145.57	77.07

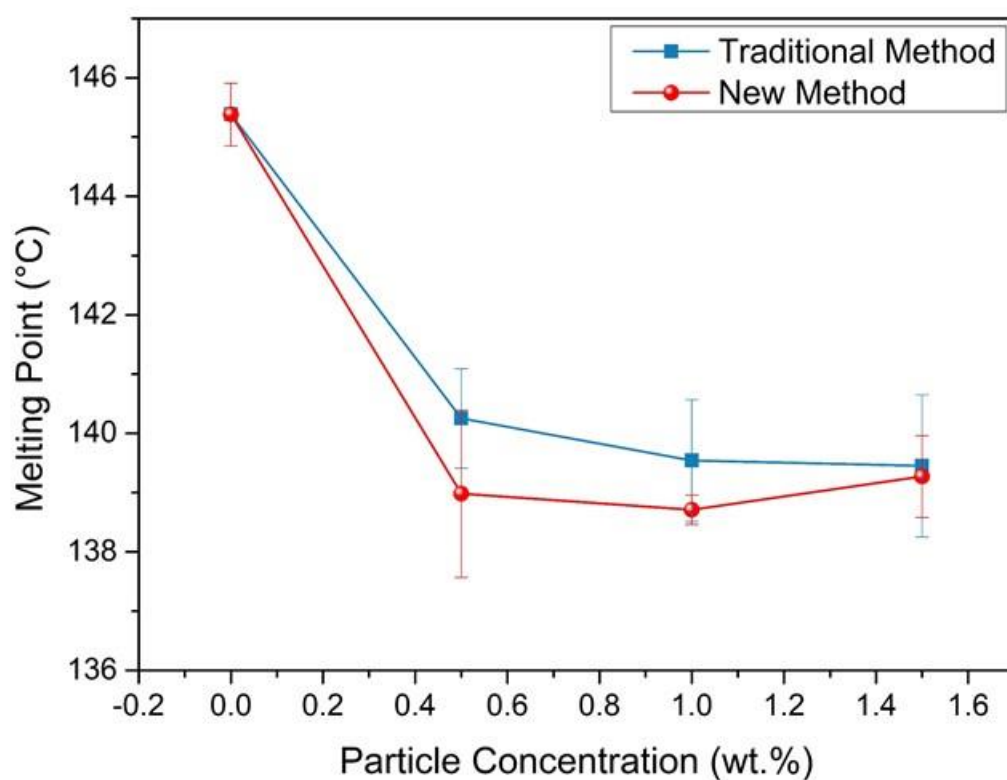


Figure 15. Comparison of melting points of the traditional two-step method and the new two-step method.

The addition of the alumina nanoparticles changed the shape of the heat flow curves during the solid-liquid phase transformation as observed in *Figure 16 d* and *e*, as well as the reduction of the heat

fusion up to 20 %. This behavior means that the added nanoparticles allowed the heat storage to be less effective per unit volume. The decrease in the melting point and the heat of fusion may be due to the nano-sized salt embedded in the interparticle space, as well as the significant heat transfer behavior of the nanoparticles [89]. This combination generates a pre-melting, that is, the melting of the solid interface at a temperature below the melting point [129]. Additionally, Svobodova-Sedlackova et al. [130] indicate a broadening in the melting peak relating it to an alteration between the phase formed on the surface, the aforementioned white layer, and the rest of the system. Due to the salt located between nanoparticles as shown in **Figure 17**, local heating is generated in them that helps to distribute the heat in a more homogeneous way throughout the nanofluid, and therefore, its melting point decreases. On the other hand, as indicated below for the increase in C_p , the formation of the white foamy phase and the ion exchange between the nanoparticles and the salt, can affect the melting temperature in the same way due to the alteration of the thermal behavior between the phase formed and the rest of the system. This behavior can lead to the formation of the shoulder shown in the curve depending on the interaction within the salt, taking into account that it is a ternary salt and not a single salt. However, this behavior must be confirmed experimentally. The interfacial thermal resistance influence cannot be ruled out either taking into account the shape of the curve obtained by the DSC and the decrease of the melting point and the heat of fusion. Nevertheless, one of the most determining factors for this behavior is given by the different synthesis methods, of the nanofluids and the base salt, and the subsequent possibility of different segregations or recombination that can be evidenced in the change in the shape of the flow curve, **Figure 16**. However, considering the storage capacity equation $Q = m\Delta TC_p$, the decrease of the melting temperature can lead to a ΔT increment, and in turn to an increase in storage capacity.

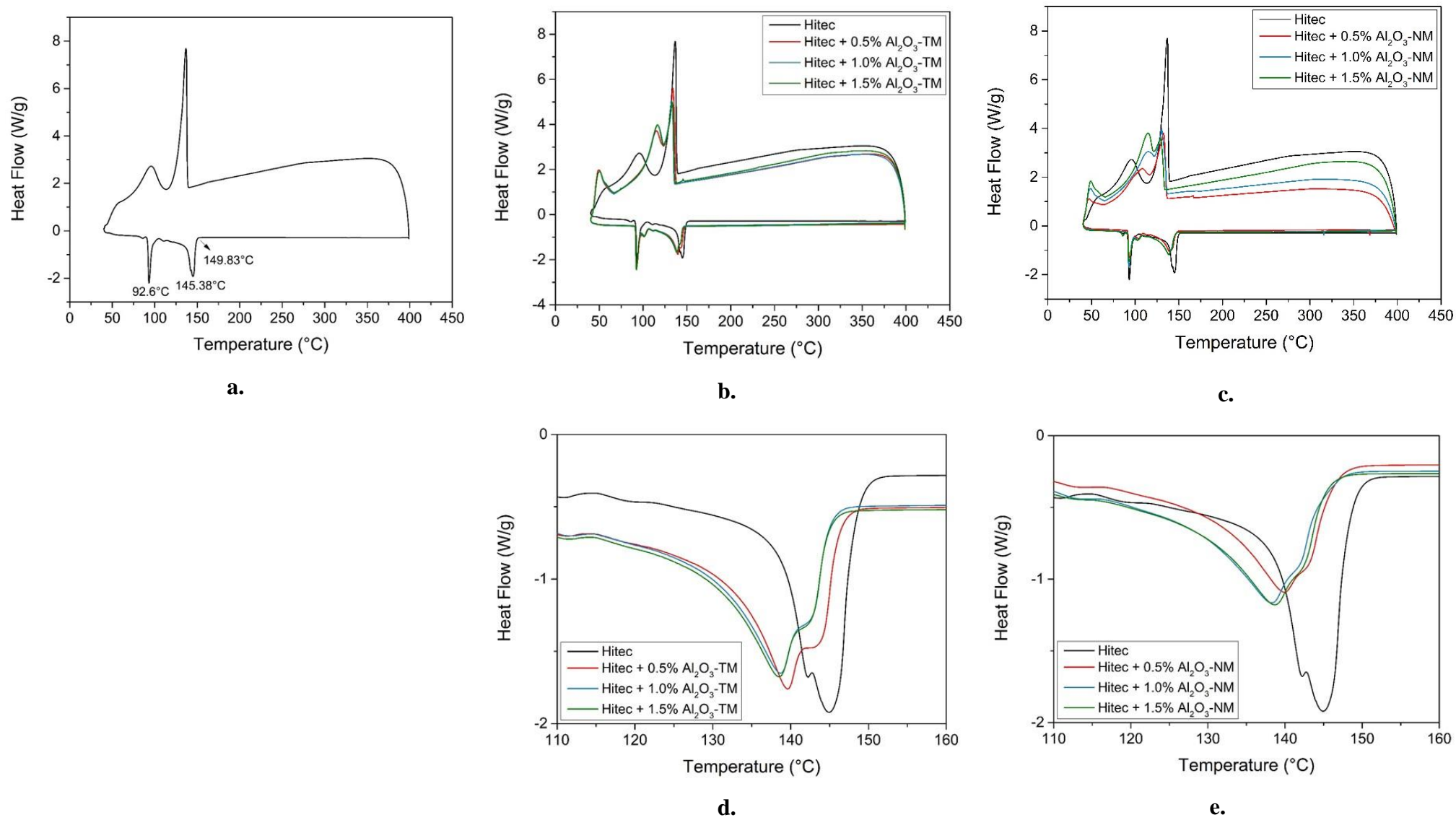


Figure 16. DSC of **a.** pure Hitec, **b.** MSBNF prepared by the traditional method (TM), **c.** MSBNF by the new method (NM), **d.** and **e.** close-up at the melting peak for TM and NM respectively.

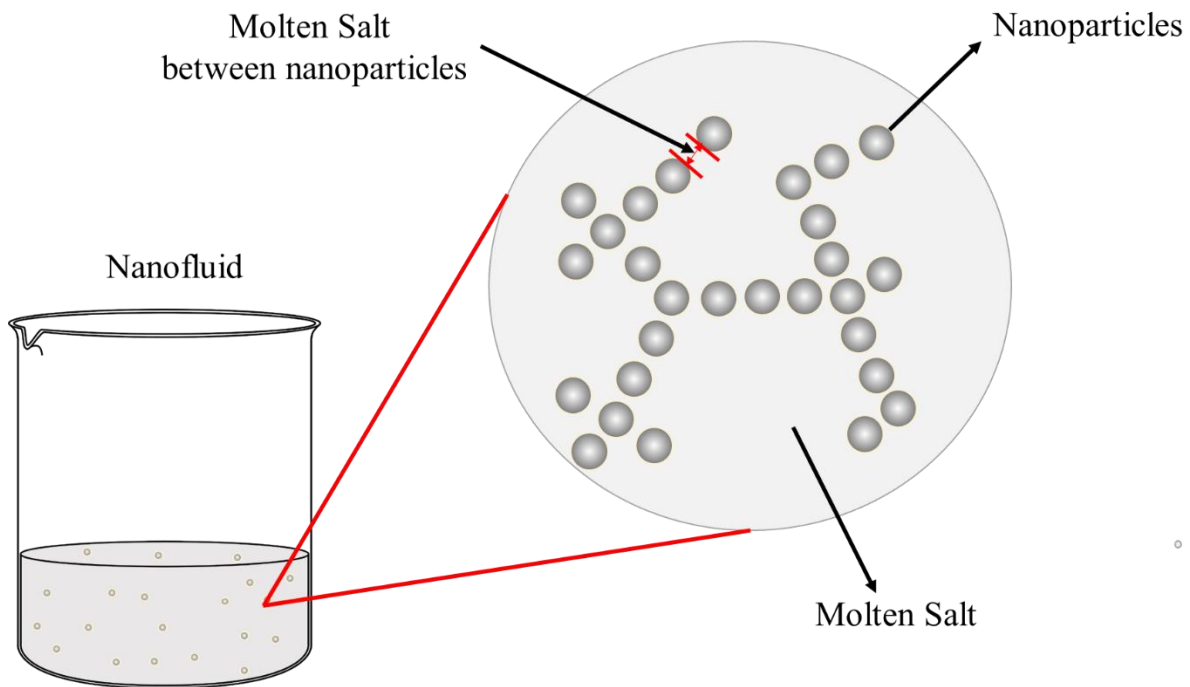


Figure 17. Graphic representation of salt embedding between nanoparticles.

5.2.2 Specific Heat Capacity (C_p)

Considering the importance of increasing the heat capacity of molten salts as a means to reduce their volume in CSP plants, the most suitable method to measure the specific heat capacity (C_p) of the molten salt is still a controversial topic, especially when nanoparticles are involved. This work is focused on the understanding of this property (C_p), mainly for the commercial molten salt Hitec compared to the Molten Salts Based Nanofluids (MSBNFs) with 0.5, 1.0, and 1.5 wt. % of alumina nanoparticles with a nominal size of 13.6 nm.

Much of the researches on nanofluids has focused on the study of the influence of particles on thermal conductivity, only 5 % of the works studied the influence on specific heat capacity [131]. It should be noted that the first researches on nanofluids showed a decrease in C_p after the addition of solid particles [132], [133]. However, these investigations were based on water-based fluids and other fluids different from molten salts. But, around 2011 [9], researches using molten salts as base fluids in nanofluids began to be reported and showed a positive and significant effect on both C_p and thermal conductivity, after the addition of small proportions of solid particles.

In this research, the specific heat capacity was measured using modulated differential scanning calorimetry (MDSC) in a temperature range of 250 to 350°C, considering the normal operating

temperature in CPS plants, especially parabolic through collectors, only results were reported at 300°C. Hence, **Table 10** shows the Cp of the pure Hitec and the MSBNFs synthesized by the traditional two-step method (TM) and the new two-step method (NM). The results show a positive effect in all the samples after the addition of the alumina nanoparticles in different concentrations and by both synthesis methods. The new two-step method, proposed here, showed an apparent improvement in Cp up to 14.08 % with the addition of 1.5 wt.% of Al₂O₃. This result, together with the decrease in the melting point, demonstrated that new method is viable for the manufacture of molten salt-based nanofluids for thermal storage applications in CSP plants, avoiding the use of water in the process and therefore its subsequent elimination. With the same proportion of nanoparticles (1.5 wt%) synthesized by TM, a maximum apparent increase of 18.74 % was obtained, considering that the dispersion of the nanoparticles within the salt is an important parameter in the improvement of the Cp of the nanofluids [37], [134], the time of sonication in the TM process can allow better dispersion of nanoparticles in the nanofluid and lead the increment of Cp. According to the standard deviations **Figure 19**, there was no statistically significant difference between the evaluated samples, which would indicate a similar increment of Cp of the MSBNFs with 0.5 and 1.0 wt.% for both synthesis methods used.

The proposed and reported mechanisms to explain the significant increment of Cp in MSBNFs considers: *i.* a higher specific heat capacity of nanoparticles than the bulk, *ii.* the abnormal increase in thermal resistance between nanoparticles and surrounding liquid molecules, *iii.* the layering of liquid molecules at the surface to form a semi-solid layer [63] and a possible fourth recently proposed mechanism regarding the functionalization of nanoparticles by ion-exchange mechanism [95]. Experimentally, in this thesis, it was not possible to demonstrate that the increase in the Cp of the nanofluid occurs by one of the mechanisms previously established. However, it is considered that the abnormal increase in Cp is not given by a single mechanism, that is, this increase may be due to a mixture of the mechanisms.

Given that the Cp of the alumina nanoparticles used to prepare the MSBNFs in this thesis is lower than the base fluid, the first mechanism cannot explain the increment of the Cp. In addition to the influence of the high surface area of the nanoparticles per unit volume and the good dispersion of the smaller in the salt, the formation of a semi-solid layer or the formation of a liquid-solid interface, which had initially been tried to verify by means of molecular dynamic simulation [78], [135], could recently be demonstrated by means of infrared thermography and thermal analysis [130]. Given the

presence of these interfaces, the existence of a temperature gradient and a foamy white layer with the nanofluid in the molten state was shown. It should be noted that this foamy white layer was also observed in this project through the initial visual observation of the melting process of the system, as well as at the time of the viscosity evaluation, in **Figure 18** the images taken in each of the these moments. However, this white layer was not evaluated individually, that is, at the end of the salt preparation process, the container was shaken manually in order to distribute the nanoparticles and proceed with cooling.

According to Svobodova-Sedlackova *et al.* [130] the white layer has a higher crystallinity compared to the rest of the fluid. In the same way, they were able to verify an alteration of the environment of the NO_3^- ion due to changes in the characteristic bands of this, evaluating in the nanofluid fusion process by means of FT-IR, as well as an ion exchange between the hydroxylated nanoparticles and the nitrate of sodium, which leads to the formation of a large super specific. Additionally, a new ordering of the species that causes the enhancement of specific heat capacity. Within the same article they report the existence of a thermal limit resistance or additional Kapitza resistance, that is, there is a resistance between the nanoparticles and another between them and the fluid. In this way, if we make an analogy between what is reported by the authors and the system evaluated in this thesis, that is, $\text{NaNO}_3 + \text{SiO}_2$, and our system the ternary salt Hitec ($\text{KNO}_3\text{-NaNO}_2\text{-NaNO}_3$) + Al_2O_3 , taking into account that visually the white foamy layer was also observed; it could be indicated that an ion exchange is also possibly generated and the formation of a second Kapitza resistance that leads to an increase in the C_p of the nanofluid [87]. However, it is important to experimentally test this behavior to be able to affirm it, especially since it has a ternary mixture instead of an individual salt, in addition to alumina nanoparticles instead of silica.

In accordance with the above, and taking into account the work reported by Mondragón *et al.* [95] in which the ion exchange capacity (IEC) of alumina and silica nanoparticles with the salts NaNO_3 , KNO_3 and LiNO_3 is evaluated. It could be indicated that the increase in C_p in the system evaluated in the thesis is lower than other systems reported in the literature, since the alumina nanoparticles have a lower IEC compared to silica, for all the salts evaluated in said article. This is due to the fact that the size of the silica nanoparticles is smaller and therefore greater specific surface area. Additionally, given that the salt in this thesis is a ternary salt with a greater presence of the K^+ cation, a greater affinity of the nanoparticles for the NO_3^- ion could be expected due to the larger size of this anion compared to Na^+ , as reported by the same authors having a higher IEC when K^+ is present.

Table 10. Average specific heat capacity at 300 °C of pure Hitec and the MSBNFs by both methods, Traditional Method (TM) and New Method (NM).

Sample	Specific Heat Capacity (J/g°C)	Change Percentage (%)	Standard Deviation
Hitec (H)	1.46	-	0.033
H+0.5% Al ₂ O ₃ -TM	1.64	12.58	0.107
H+1.0% Al ₂ O ₃ -TM	1.68	14.91	0.140
H+1.5% Al ₂ O ₃ -TM	1.73	18.74	0.028
H+0.5% Al ₂ O ₃ -NM	1.67	14.63	0.143
H+1.0% Al ₂ O ₃ -NM	1.60	9.66	0.011
H+1.5% Al ₂ O ₃ -NM	1.67	14.08	0.001



a.



b.

Figure 18. Evidence of the presence of the foam layer in the nanofluids a. during visual inspection of the fusion, b. the corrosion assessment process and c. in the evaluation of viscosity.

So far, there is no consensus on the reason for the improvement of the Cp of nanofluids, especially the MSBNFs, as well as the mechanisms that lead to a significant increase with low proportions of nanoparticles. Some authors have reported that with 1 wt.% of nanoparticles the greatest increase in Cp is obtained [61], [69], [72], [85], others such as Ho and Pan [50] have carried out a study of the optimal concentration of alumina nanoparticles in Hitec salt, concluding that with a concentration

greater than 0.063 wt.% the Cp of the salt is negatively affected with reductions of up to 5.7 % with the addition of 2 wt.% of Al₂O₃, while Hu *et al.* [61] reported an 8.3 % increase in Cp of binary salt with 2 wt.% Alumina nanoparticles.

Additionally, several theoretical models have been reported for determining the Cp of nanofluids, the first model is similar to the mixing theory for ideal gas mixtures, **Equation 6**, the second model, known as the “simple mixing model”, assumes that the base fluid and the nanoparticles are in thermal equilibrium as expressed in **Equation 7**, and the third model, established by Shin *et al.* and shown in **Equation 8**, considers the contribution of the compressed phase to the total specific heat capacity of the nanomaterials.

$$Cp_{nf} = \phi Cp_{np} + (1 - \phi) Cp_{bf} \quad \text{Equation 6}$$

$$Cp_{nf} = \frac{\phi(\rho_{np} Cp_{np}) + (1 - \phi)(\rho_{bf} Cp_{bf})}{\phi(\rho_{np}) + (1 - \phi)(\rho_{bf})} \quad \text{Equation 7}$$

$$Cp_{nf} = \frac{\rho_{np} \phi_{np} Cp_{np} + \rho_c \phi_c Cp_c + \rho_{bf} \phi_{bf} Cp_{bf}}{\rho_{np} V_{np} + \rho_c V_c + \rho_{bf} V_{bf}} \quad \text{Equation 8}$$

Where, ϕ is the volume fraction of nanoparticles, ρ the density and the subscripts nf, np, c, and bf refer to the nanofluid, nanoparticle, compressed layer, and base fluid, respectively [58], [65], [136]. It is important to highlight that in nanofluids discussed in here, the values of Cp, density and volume fraction of the compressed layer were taken according to what was established by Shin *et al.*, that is, the Cp value of the layer is 4 times the Cp value of the salt, the density of the layer is equal to that of the base salt, and the volume fraction was calculated taking into account the thickness of the layer of 1.67 nm for the alumina particles.

Table 11 shows the Cp values determined by the three models previously established. A lower value of Cp compared with the base fluid is obtained with the addition of nanoparticles and decrease with the concentration increment for the first two theoretical models (Model-1 and Simple mixing model), while the model established by Shin *et al.* showed an increase in Cp compared to the base fluid and concerning the concentration of nanoparticles. Although some authors report a good agreement between these models and the experimental data, and even though the theoretical model proposed by

Shin *et al.* considers the compressed or semi-solid layer and which shows a growth of the Cp of the nanofluids regarding the Cp of the molten salt, the rate of increase is not equal to what was found experimentally. For that reason, in this case, it is necessary to consider other factors or physical-chemical parameters that can explain the anomalous improvement obtained.

Table 11. Specific heat capacity of different particle concentrations obtained by the Simple mixing model.

Concentration Particle (wt.%)	Model-1 Cp (J/g°C)	Simple mixing model Cp (J/g°C)	Shin <i>et al.</i> model Cp (J/g°C)
0	1.460	1.460	1.460
0.5	1.459	1.457	1.465
1.0	1.457	1.453	1.470
1.5	1.456	1.450	1.475

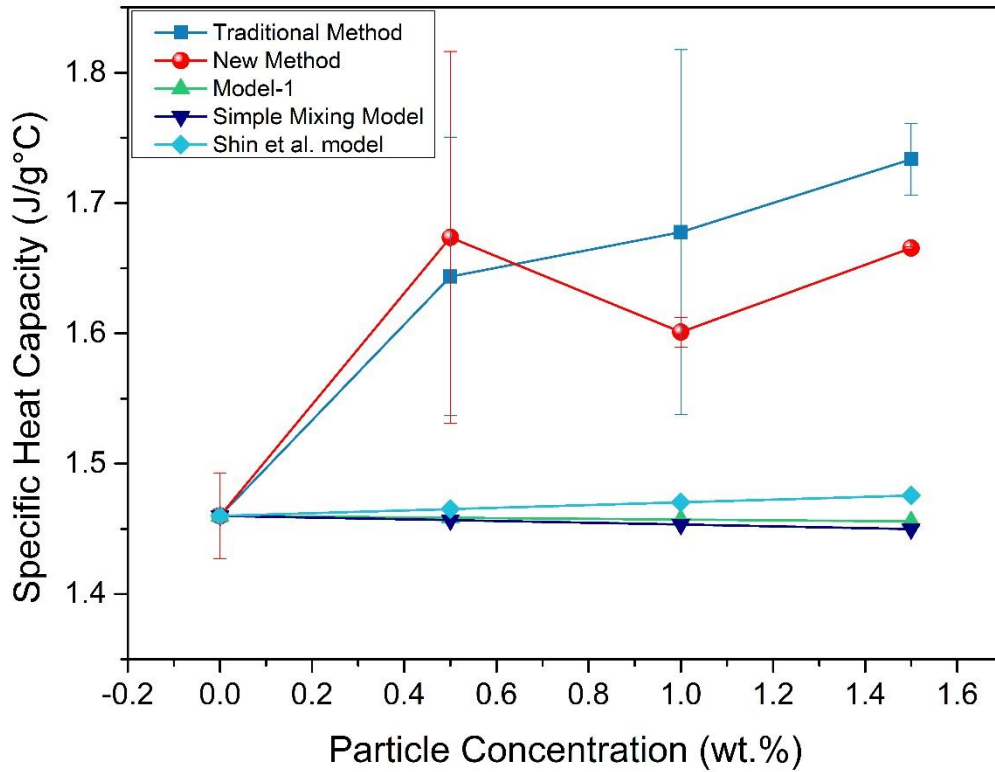


Figure 19. Comparison of the specific heat capacity of the Traditional two-step method, New two-step method, and the theoretical models.

5.2.3 Microstructural Analysis

To determine the presence of the nanoparticles after the measurement of the C_p by MDSC, as well as to observe the degree of dispersion and agglomeration of solid particles in the molten salt, a microstructural study was performed using Scanning Electron Microscopy (SEM). In the same way, the elemental mapping was performed to ensure the good distribution of the nanoparticles and the molten salt components. **Figure 20** shows the SEM image of the pure Hitec and the nanofluids are shown in **Figure 21**, in which, the images a, b, and c correspond to the samples synthesized by the traditional two-step method with proportions 0.5, 1.0 and 1.5 wt.% of alumina respectively, and d, f, and e the samples prepared by the new two-step method with 0.5, 1.0 and 1.5 wt.% of Al_2O_3 respectively.

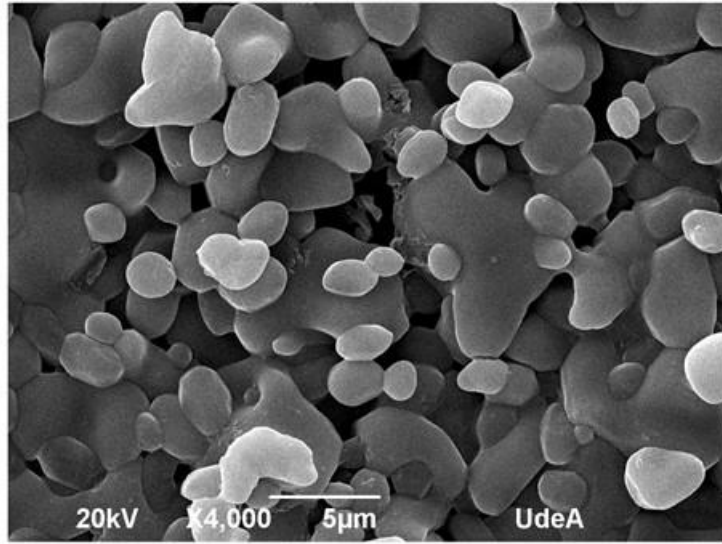


Figure 20. SEM Images of pure Hitec.

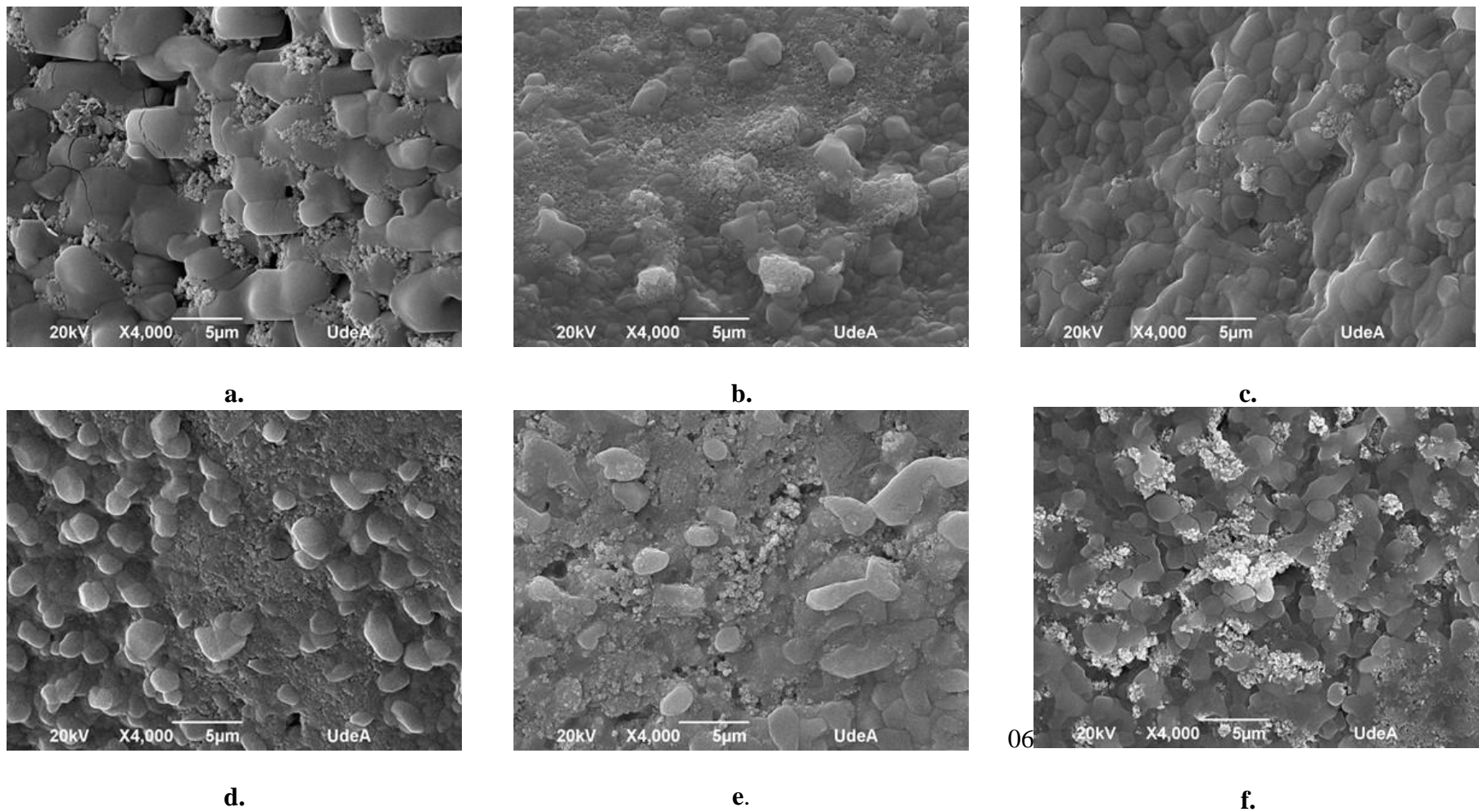


Figure 21. SEM images after MDSC evaluation a, b, c samples elaborated by traditional two-step method with 0.5, 1.0 and 1.5 wt.% of alumina nanoparticles, respectively, and d, e, f. sample elaborated by new two-step method with 0.5, 1.0 and 1.5 wt.% of alumina nanoparticles, respectively.

A similar microstructure of the MSBNFs can be observed in **Figure 21**, which means that they are not influenced by the synthesis method. The presence of the alumina nanoparticles in all samples prepared by both methods TM and NM was evident, as well as the uniform nanoparticles dispersions inside the molten salt that can be observed for all samples evaluated. This result can be confirmed by elemental mapping shown in **Figure 22**, where a good distribution of the base elements of the salt was evident, i.e. Na and K, and the presence of the nanoparticles (blue color) was observed. However, localized agglomeration was visible.

It is important to highlight that this research did not show the presence of the interconnecting network of nanoparticles or needle-like structure as reported for some authors [63]. However, the absence of these connecting networks has been reported by several authors [50], [60], [62], [72]. Therefore, this is not the reason why there was a significant increase in C_p , although the distribution in the solid-state does not necessarily correspond to the distribution of the nanoparticles in the molten state. In this case, the increment of the heat capacity could be due to the high surface area of the nanoparticles per unit volume and the particle size distribution, that is, smaller particles may be more dispersed within the salt and increase thermal properties [62].

On the other hand, some authors have reported that the C_p decrease is given the increment of the agglomeration of the nanoparticles with the increase of particle concentration [78]. Nevertheless, in this research, a greater increase in C_p could be observed for the highest concentration obtained by traditional two-step method, a sample in which less agglomeration was observed, see **Figure 21 c**. Though, samples with greater agglomeration, 1.0 and 0.5 wt.% of Al_2O_3 obtained by TM and 1.0 wt.% of Al_2O_3 synthesized by NM, presented the lower C_p value, while the other two samples prepared by NM showed the similar grade of agglomeration and C_p value, confirming that the amount of agglomerates is a determining factor in the C_p of nanofluids. Additionally, comparing the structure of the salt in the MSBNFs **Figure 21** and the base fluid **Figure 20**, the grain size reduction can be detected, especially for the samples with higher C_p values, this behavior has been reported by other authors [50], [72].

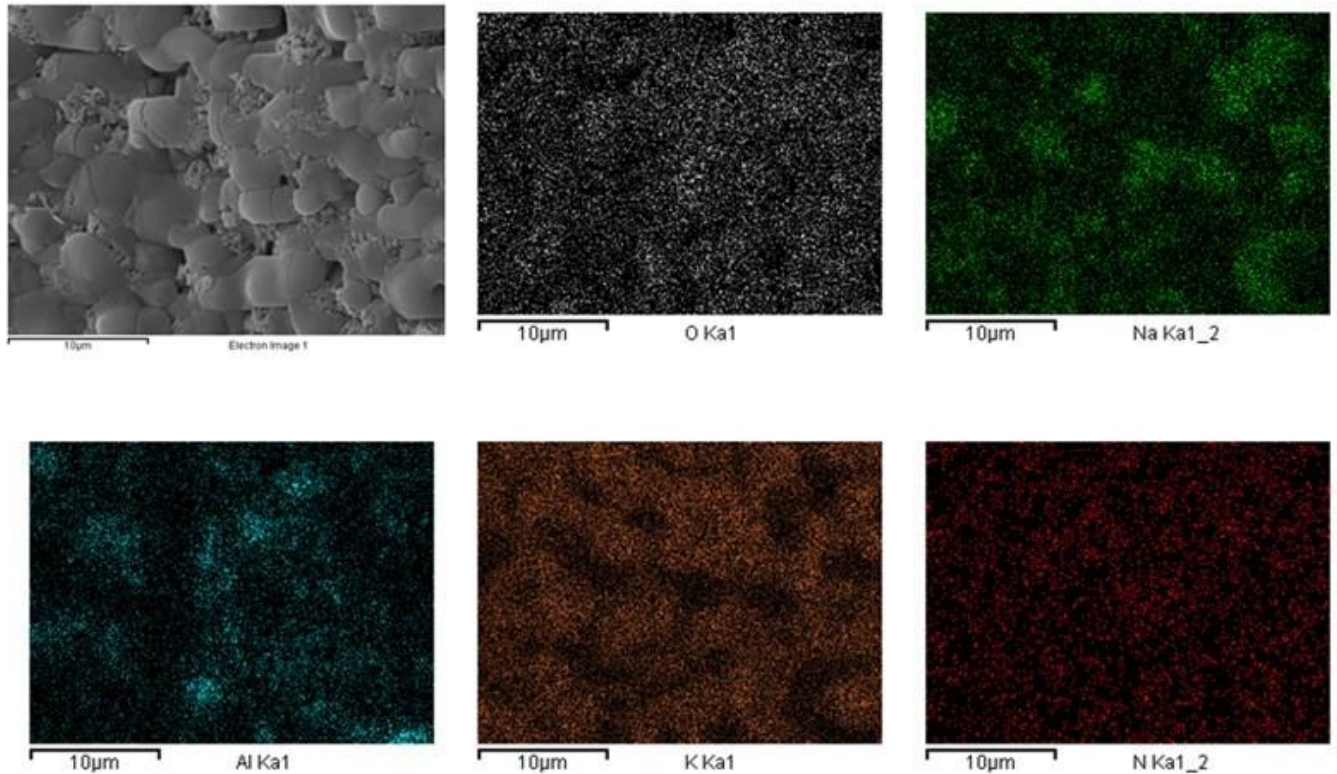


Figure 22. Example elemental mapping, MSBNF with 0.5 wt.% of Al_2O_3 obtained by TM after the MDSC evaluation (O-white, Na-green, Al-blue, K-orange, and N-red).

5.2.4 Thermal Stability

The results for the TGA experiments are summarized in *Table 12* and **Figure 23**, **Figure 24**, and **Figure 25**. To evaluate the thermal stability of the molten salt Hitec and the MSBNFs, we followed the criterion for the maximum stability temperature where 3 % of the overall weight has been lost [24], [26], for this a temperature of 300°C was chosen as the initial temperature where the mass loss started.

As can be observed in **Figure 23** and **Figure 24** Hitec and the nanofluids presented a similar decomposition curve and the thermal stability under N_2 atmosphere. The decomposition temperature of Hitec was estimated at 621.88°C, this value was slightly lower than the reported by Villada *et al.* [24] who reported a decomposition temperature value of 639.11°C, and Fernández *et al.* [43] informed 630.97°C, both studies for an inert atmosphere. However, other authors presented a maximum

thermal stability between 535 to 538°C under N₂ atmosphere [48], [137] and 610°C under the same atmosphere [128], this behavior may be due to both the raw materials and the salt preparation method, showing that there is not a consensus about this thermal property. On the other hand, the decomposition temperature for the MSBNFs was higher than 616°C, it was not significantly affected by the addition of the nanoparticles or by the nanofluid synthesis method, TM and NM. Increases of up to 1.91 % and reductions of up to 0.15 % were obtained. In this way, it could be said that the nanofluids obtained by both methods are stable; this behavior is in accordance with some reports by other authors in which, a mass of loss of 1 % was observed [58], [89].

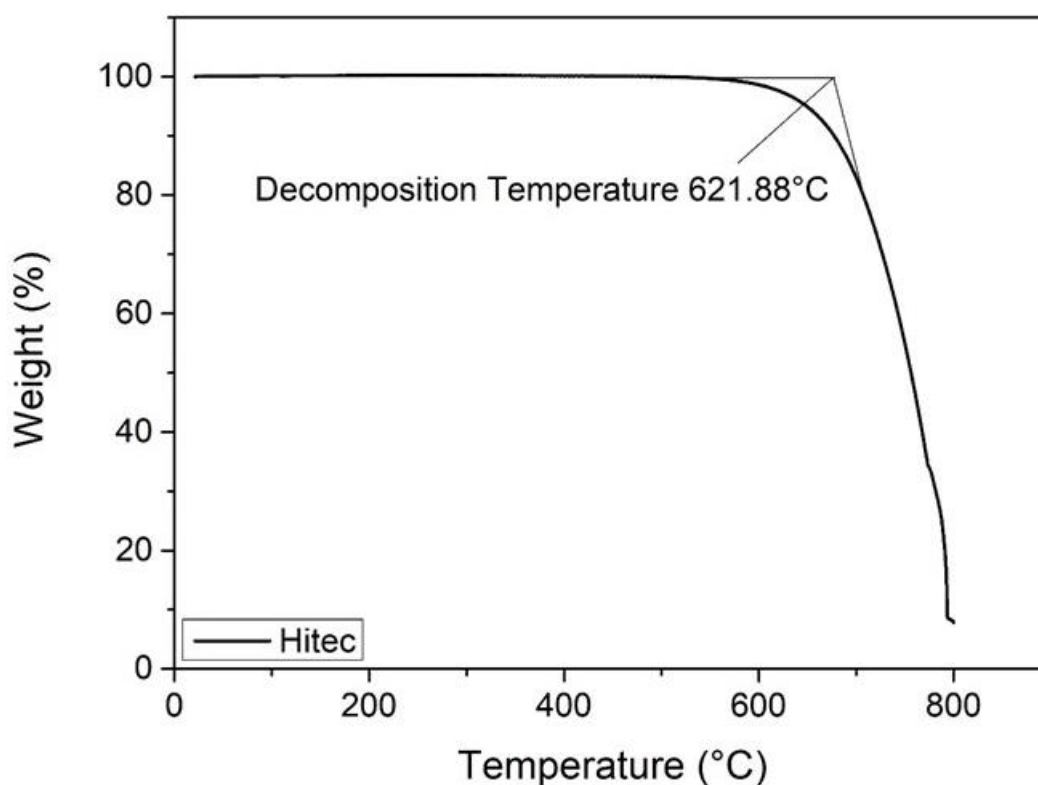


Figure 23. Decomposition temperature under N₂ atmosphere of pure Hitec from TGA measurements.

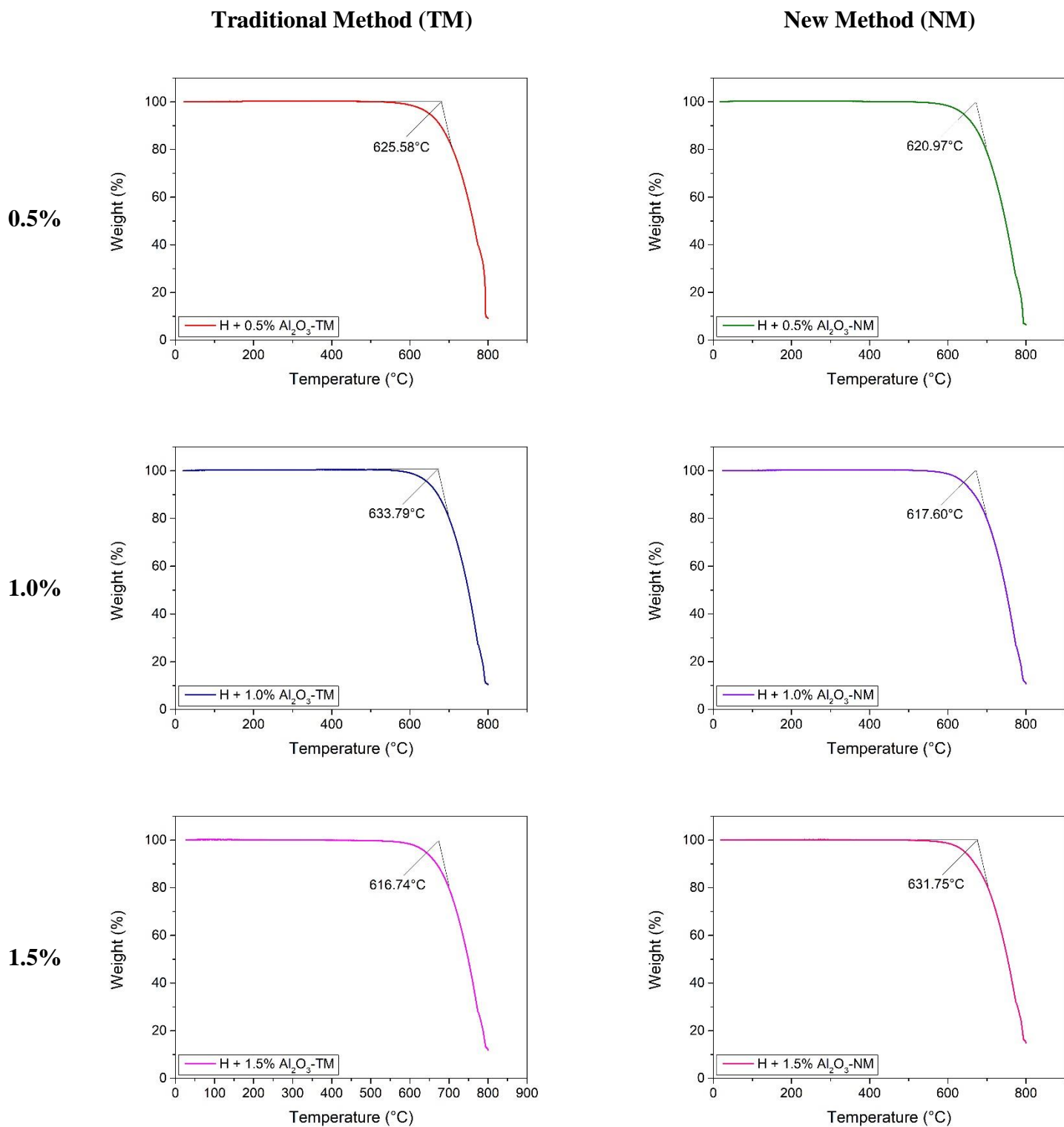
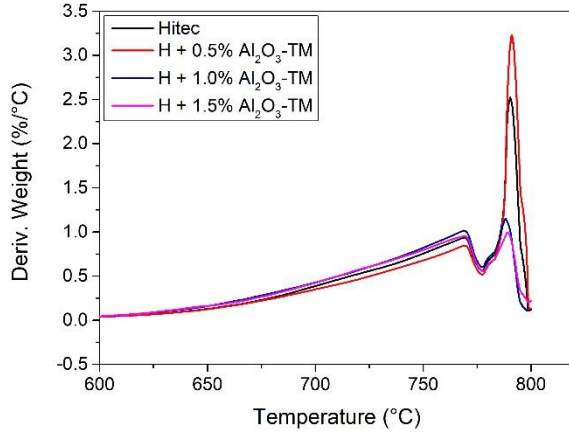


Figure 24. Decomposition temperature under N₂ atmosphere of the MSBNFs synthesized by TM and NM, from TGA measurements.

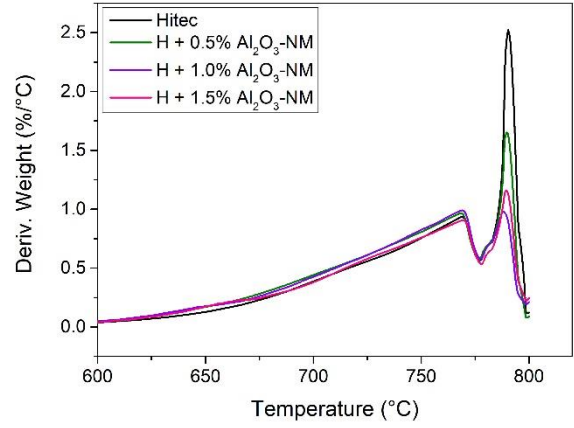
Table 12. Thermal stability analysis under N₂ of pure Hitec and MSBNFS by both methods studied.

Sample	Thermal decomposition (°C)	Standard deviation	Change Percentage (%)	Bulk of decomposition (°C)	Standard deviation	Change Percentage (%)
Hitec (H)	621.88	0.58	-	785.68	4.58	-
H+0.5% Al₂O₃-TM	625.58	6.22	0.59	788.30	2.79	0.33
H+1.0% Al₂O₃-TM	633.79	7.66	1.91	791.11	2.76	0.69
H+1.5% Al₂O₃-TM	616.74	4.36	-0.83	789.40	0.35	0.47
H+0.5% Al₂O₃-NM	620.97	4.14	-0.15	784.92	9.57	-0.10
H+1.0% Al₂O₃-NM	617.60	5.49	-0.69	790.18	2.83	0.57
H+1.5%Al₂O₃-NM	631.75	6.99	1.59	790.67	1.34	0.64

Figure 25 shows the bulk decomposition of the MSBNFs prepared by TM and NM methods that is the maximum signal in the derivate weight change curves. According to the results, the bulk decomposition values were also not affected significantly by the addition of nanoparticles or the use of different synthesis methods, and Hitec bulk decomposition temperature is close to those reported by other authors (789°C under N₂) [128]. The form or the peaks can be related to the evolution of nitrogen species (N, N₂) at 780°C, as well as O₂ and NO₂ species [128]. However, considering the amount of sample evaluated by TGA (less than 10 mg), and compared to the real amount in CSP plants, approximately 30.000 tons, the examination in terms of salt composition and kinetics are required, similar to the reported by Villada [49]



a.



b.

Figure 25. Derivate weight change showing bulk decomposition processes of the MSBNFs synthesized by **a.** TM and **b.** NM.

5.2.5 The storage capacity of the Hitec and MSBNFS

Considering the main use of the materials proposed in this research, that is, as material for thermal storage in CSP plants, the influence of their thermal properties, especially the specific heat capacity, melting temperature, and stability temperature, as well as the system operating temperature and tank size in the thermal storage capacity must be taken into account. Hence, the storage capacity through the sensible heat was calculated using *Equation 9*, according to the properties previously presented (specific heat capacity, melting point, and thermal decomposition under nitrogen) and with 1 ton as a calculation basis. Similarly, the density of the samples was obtained by applying mixed classical theory *Equation 10* [138] where ϕ_p is the volume fraction of the particles and ρ_{bf} and ρ_p the density of base fluid and nanoparticles respectively.

$$Q = mC_p\Delta T \quad \text{Equation 9}$$

$$\rho_{nf} = (1 - \phi_p)\rho_{bf} + \phi_p\rho_p \quad \text{Equation 10}$$

Table 13 shows the storage capacity in KW-h as well as the cost per kilogram, the storage cost, estimated by **Equation 11** [135], and the density of the Hitec salt and the MSBNFs synthesized by both the traditional two-step method and the new two-step method proposed in this research. The calculation was performed taking into account the cost value of the molten salt at analytical and industrial grade. Hence, all samples evaluated showed a reduction of more than 10 % in the storage cost, in addition to a small reduction in cost per kilogram and an increase in storage capacity. Concerning the degree of purity of the salt, using an industrial-grade salt costs less than using an analytical grade salt.

Also, it is possible to observe an increase in storage capacity of up to 20% for the MSBNF with 1.0 wt.% of alumina synthesized by the traditional two-step method and with storage cost less than 18 % compared with the base salt. However, these calculations do not take into account other important factors of the process such as the amount of water used in the traditional method, the energy consumed for its elimination, and therefore the additional cost. Thus, when comparing the nanofluids obtained by the two methods, with the same proportion of nanoparticles, the increases in the storage capacities and costs were similar, except for 1.0 wt.%. However, the potential of the proposed method is evident given the reduction of water and decrease of energy consumption to eliminate it. The density increases with the increase of particles concentration, behavior reported by other authors [61], [138], which shows that this property can be estimated very accurately using classical mixed theory.

$$\text{Storage cost} \left[\frac{\$}{\text{kWh}} \right] = \frac{\text{Cost per kg} \left[\frac{\$}{\text{kg}} \right]}{\text{Average } C_p \left[\frac{\text{kJ}}{\text{kgK}} \right] * \Delta T [\text{K}] * 2.778 \cdot 10^{-4} \left[\frac{\text{kWh}}{\text{kJ}} \right]} \quad \text{Equation 11}$$

Table 13. Storage capacity and Effective storage fluid cost of the Hitec and MSBNFs synthesized by two-step traditional and new methods.

Sample	Specific Heat Capacity kJ/KgK	Density (kg/m ³) at 300°C [Ref.]	Storage Capacity (kWh)	Change of Storage Capacity from Hitec (%)	Cost per kg (US \$/ kg) [Ref.] Analytical grade	Storage Cost (US \$/ kWh) Analytical grade	Cost per kg (US \$/ kg) [Ref.] Industrial grade	Storage Cost (US \$/ kWh) Industrial grade
Hitec (H)	1.46	1640 [139]	161	-	0.930 [48]	5.78	0.370	2.30
Alumina	0.79	3951.74	-	-	0.170 [140]	-	0.170 [140]	-
H+0.5% Al₂O₃-TM	1.64	1644.81	185	15	0.926	5.02	0.369	2.00
H+1.0% Al₂O₃-TM	1.68	1649.65	193	20	0.922	4.77	0.368	1.90
H+1.5% Al₂O₃-TM	1.73	1654.52	191	19	0.919	4.81	0.367	1.92
H+0.5% Al₂O₃-NM	1.67	1644.81	185	15	0.926	5.02	0.369	2.00
H+1.0% Al₂O₃-NM	1.60	1649.65	177	10	0.922	5.20	0.368	2.08
H+1.5%Al₂O₃-NM	1.67	1654.52	191	19	0.919	4.80	0.367	1.92

Currently, one of the problems for the deployment of solar energy is the high Levelized cost of energy (LCOE), i.e., the commonly used metric that represents the performance and cost as a dollar amount per unit energy generated [141]. By the end of 2018, the LCOE of CSP plants was 0.185 US\$/kWh for 0.5 GW of capacity added [20]. Some of the parameters to be calculated for the estimation of LCOE is the initial investment cost including the components and system costs, as well as the efficiency; the implementation of TES system with molten salt as a storage medium in the two-tanks configuration, used as a strategy to reduce the LCOE, showed an efficiency of >98% [89]. Hence, increasing the storage capacity improves the TES and in turn contributes to the reduction of the LCOE, making the technology more competitive compared to traditional energy sources [142].

5.3 Conclusion

The thermophysical properties of the pure Hitec as a reference and the molten salt-based nanofluids (MSBNFs) was evaluated. MSBNFs were successfully synthesized by two different methods, traditional two-step method (TM) and a new two-step method (NM) proposed by replacing the water with butanol, with the aim to avoid the use of water in the process and the decrease the preparation time of the nanofluids. The melting temperature, the specific heat capacity and thermal stability were reported and measured by DSC, MDSC and TGA, respectively. The microstructure after the MDSC evaluation was also shown, in addition to the heat capacity storage of the molten salt evaluated.

A new two-step method was proposed, in which the use of water in the process is avoided and the time of the process is reduced with the use of butanol to obtain a good dispersion of alumina nanoparticles. According to the results, it was possible to demonstrate the viability of the synthesis of the molten salt-based nanofluids by this method thanks to the apparent increase in specific heat capacity up to 14.08 % with 1.5 wt.% of nanoparticles, as well as the apparent decrease in the melting point of up to 4.21 % with the same amount of nanoparticles, with a minimum effect on the stability temperature of nanofluids. Using the traditional method established by Shin and Banerjee for the synthesis of MSBNFs, an apparent increase of up to 18.74 % of the specific heat capacity was obtained with 1.5 wt.% of nanoparticles, and a decrease of 4.08 % of the melting point. Similarly, there was no significant effect on the stability of the nanofluid. The other alumina nanoparticle proportions synthesized by both methods (0.5 and 1.0 wt.%), did not show a statistically significant difference in the increase in C_p , so their behavior was similar.

After the evaluation of the thermal properties, especially of the C_p by MDSC, the presence of the nanoparticles was determined by SEM for both synthesis methods. It should be noted that no new nanostructures like those reported by other authors were found, which have been proposed as being responsible for the significant increase in the C_p of MSBNFs. Experimentally, in this thesis, it was not possible to demonstrate that the increase in the C_p of the nanofluid occurred by one of the mechanisms proposed by other authors. However, taking into account what was observed both visually in the nanofluids developed and in the results obtained for the thermophysical properties, in addition to the current reports in the literature. It is considered that the increase in C_p may be due to a combination of some of these mechanisms.

In addition to the influence of the high surface area of the nanoparticles per unit volume and the good dispersion of the smallest particles in the salt, the increase in C_p may be due to the formation of a new phase, a white foam also observed in this work, which some authors have shown has an effect both on the ionic interaction of the fluid with the nanoparticles, and on the generation of a second Kapitza resistance. On the other hand, taking into account other studies, it could be indicated that the ion exchange capacity would be favored thanks to the presence of the potassium ion within the salt. The mixture of all these factors and the additional ones that must be tested experimentally for this particular system, in which there is the presence of three different salts, can lead to obtaining additional storage and therefore to an increase in the C_p of the nanofluid.

An increase up to 20% in the storage capacity of the nanofluids synthesized by both methods was shown compared to the base fluid, with 1.0 wt.% of alumina nanoparticles synthesized by TM method and with 1.5 wt.% of alumina nanoparticles using NM method. Similarly, the cost of storage had a positive effect after the use of nanoparticles, that is, it was reduced by up to 18% using the traditional two-step method (with 1.0 wt.% of nanoparticles) and up to 17% for the new two-step method (with 1.5 wt.% of nanoparticles).

According to the results previously exposed, the feasibility of applying the method developed in this thesis is demonstrated, obtaining properties comparable to the traditional two-step method, with similar storage costs as well as storage capacity, but reducing costs in the synthesis process by decreasing solvent evaporation time.

5.4 Corrosive Behavior Test of Hitec and Molten Salts-Based Nanofluids in contact with AISI 304

To establish the aggressiveness of nanofluids against steel, which is commonly used for the manufacture of containers in CSP plants [143], Hitec was used as a reference salt and, given the results of Cp described above, the nanofluid with 1.5 wt.% of Al₂O₃ synthesized by the traditional two-step method was also selected as the corrosive environment. Stainless steel AISI 304 (SS304) was chosen given its characteristics, such as good resistance to corrosion, prevention of contaminating products, and adequate resistance to creep. Two reactors, see *Figure 11*, with controlled N₂ atmosphere, temperature, and mechanical agitation were manufactured to ensure the same conditions during 2000 h at 550°C for pure Hitec and the selected MSBNF. Three different positions inside each reactor were selected for the evaluation of stainless steel samples: bottom to evaluate the influence of particles precipitation, as some authors have proposed [102], medium to determine the real aggressiveness of the nanofluid, and top with a part in contact with the fluid and another part above the nanofluid level to evaluate the possible effect of gases released by the salt. In the following section, the isothermal immersion test to measure the mass change and the corrosion rate is shown. Moreover, the characterization of SS304 samples and the molten salts evaluated is presented. SEM and EDX analyses were employed to determine the morphological evolution, thickness, and chemical composition of the samples; finally, the corrosion products were determined by XRD.

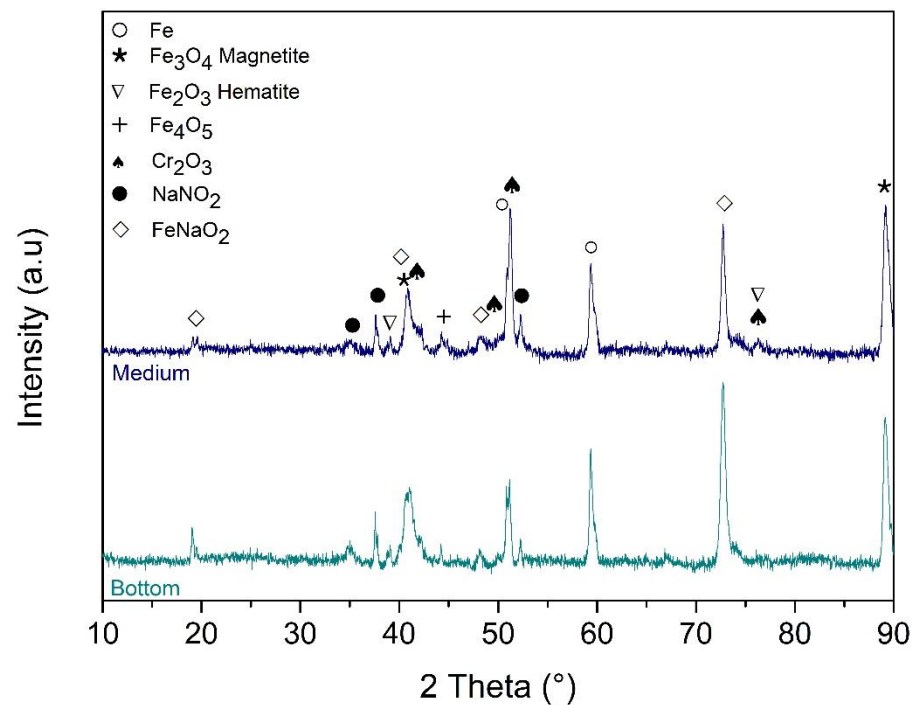
5.4.1 Composition and Structure by XRD

A conventional XRD and a Rietveld refinement analysis were used to identify the corrosion products present in the SS304 samples immersed in the Hitec salt and the nanofluid after 672 h at 550°C under a controlled N₂ atmosphere. *Figure 26* and *Table 14* shows the XRD pattern and the phases obtained by the refinement, it is important to highlight that the Rietveld refinement was performed without background subtraction, which was done only to improve the presentation of the images. *Table 15* presents agreement indices for the Rietveld fitting procedure. The weighted R profile (Rwp) and the goodness of fit (GOF) confirmed a good fit because their values were lower than 10% and 4, respectively [144].

After 672 h of exposure, all samples showed the presence of two main corrosion phases, magnetite (Fe₃O₄) and sodium iron oxide (NaFeO₂), as well as a protective layer of chromium. However,

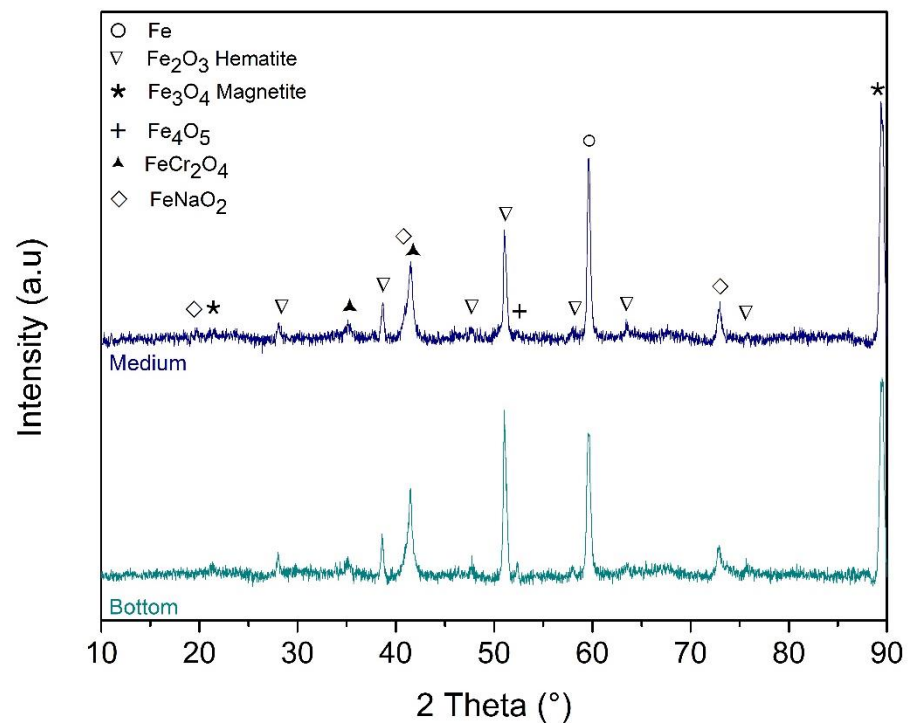
different types of chromium oxide protective layers were found for the samples exposed in Hitec compared to those exposed in the nanofluid. The samples exposed in Hitec formed a simple chromium oxide Cr_2O_3 , while those immersed in the nanofluid showed the “less-protective” compound spinel FeCr_2O_4 (35.1° and 38.7°) [145]–[147]. This behavior had been reported by other authors with similar exposure times and temperatures, indicating that the protective layer of chromium oxide Cr_2O_3 that characterizes SS304 samples is not maintained given the dissolution of chromium in contact with nitrate/or nitrite base salts [113].

Additionally, in both cases the presence of some peaks corresponding to the substrate was evidenced, indicating that the penetration depth of X-ray beams (micrometers) exceeded the corrosion layer thickness, 9.50 nm for the samples immersed in Hitec salt and 6.08 nm for the samples immersed in the nanofluid [102]. Also, the increase in the exposure time of the samples could propitiate the growth of the iron oxides present in the sample and the FeNaO_2 layer, as it was observed in SEM and EDX analysis; this behavior has been reported by other authors [148].



a.

a.



b.

Figure 26. The XRD pattern of AISI 304 immerses in a. Hitec and b. MSBNF after 672 h at 550°C, in the bottom and medium position inside the reactors.

Table 14. Quantitative Rietveld analysis of SS304 immersed in Hitec and MSBNF after 672 h at 550°C, in the bottom and medium position inside the reactors.

Phase	Weight fraction (%)			
	Hitec		MSBNF	
	Bottom	Medium	Bottom	Medium
Iron	8.0	37.3	14.6	12.5
Hematite (α -Fe ₂ O ₃)	-	3.6	8.2	7.9
Magnetite (Fe ₃ O ₄)	58.2	5.2	32.3	27.6
Fe ₄ O ₅	25.6	16.8	16.6	20.3
Chromite (FeCr ₂ O ₄)	-	-	4.6	6.5
Cr ₂ O ₃	2.9	4.7	-	-
FeNaO ₂	4.4	27.8	23.8	25.3
NaNO ₂	0.8	4.7	-	-

Table 15. Agreement indices for the Rietveld fitting procedure.

Sample		Weighted R Profile Rwp (%)	Goodness of Fit GOF
Hitec	Bottom	2.61	1.65
	Medium	3.10	2.22
MSBNF	Bottom	2.27	1.31
	Medium	2.30	1.33

5.4.2 Morphological development by SEM/EDX analysis

In order to compare the corrosion behavior produced by pure Hitec and the MSBNF with 1.5 wt.% of Al₂O₃ in the SS304, SEM was used to determine the evolution of the morphology throughout immersion time. *Figure 27* and *Figure 28* show the morphology of the oxide layer of the samples immersed in the reactor with pure Hitec and with the MSBNF, respectively. Different microstructures, stick type and hexagonal, were observed in all samples evaluates, which grew with

the time of exposure. By comparing the samples immersed in the different salts, R1 with pure Hitec and R2 with the MSBNF, it seems the microstructures are similar, although their growth was faster for samples immersed in pure Hitec. Additionally, the presence of nanoparticles in the sample layer even after 2000h of exposure was observed. It is important to highlight that the morphology was not affected by the location of the samples inside the reactors.

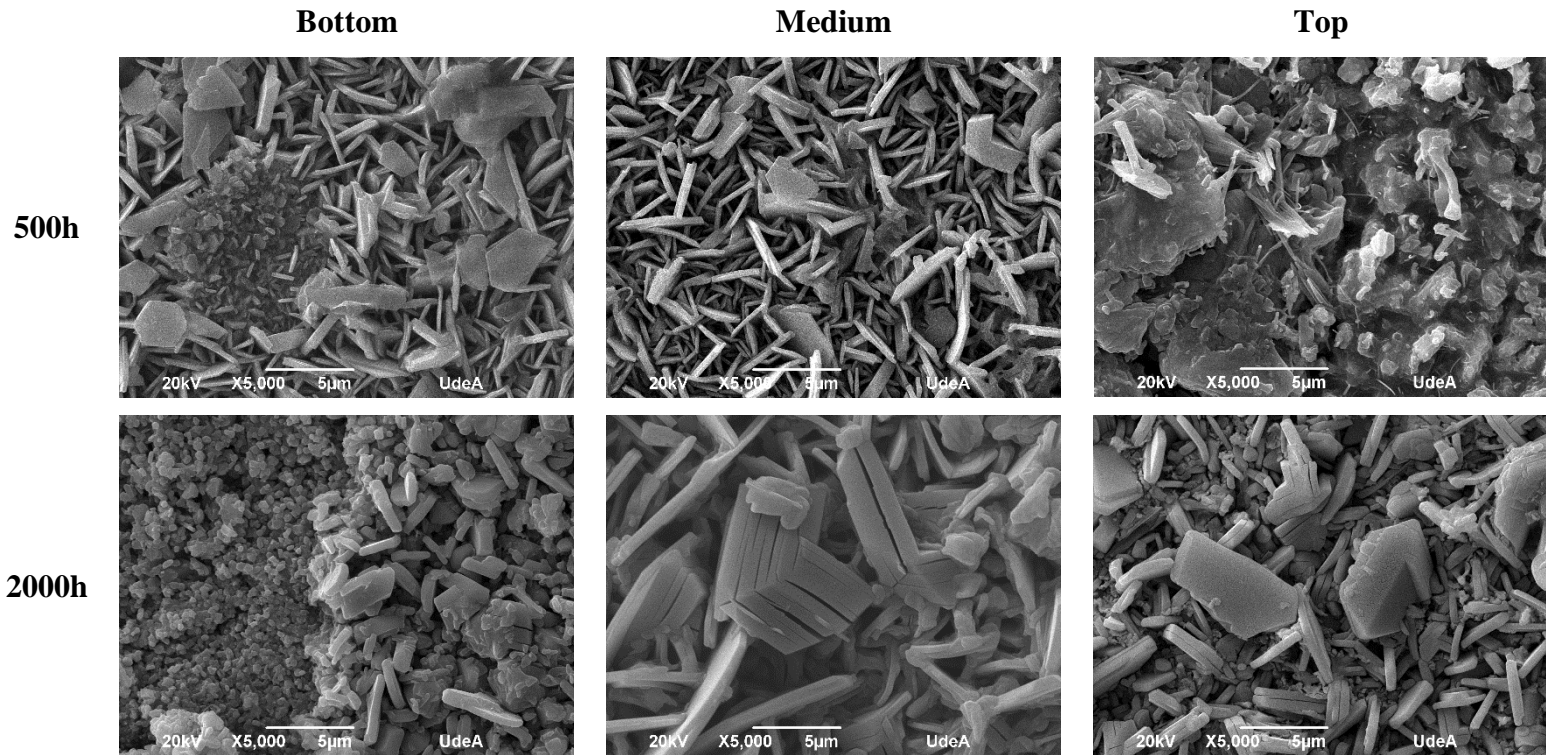


Figure 27. SEM images of the surface of metal samples in contact with pure Hitec after 500 h and 2000 h immersion test, in three different positions bottom, medium, and top.

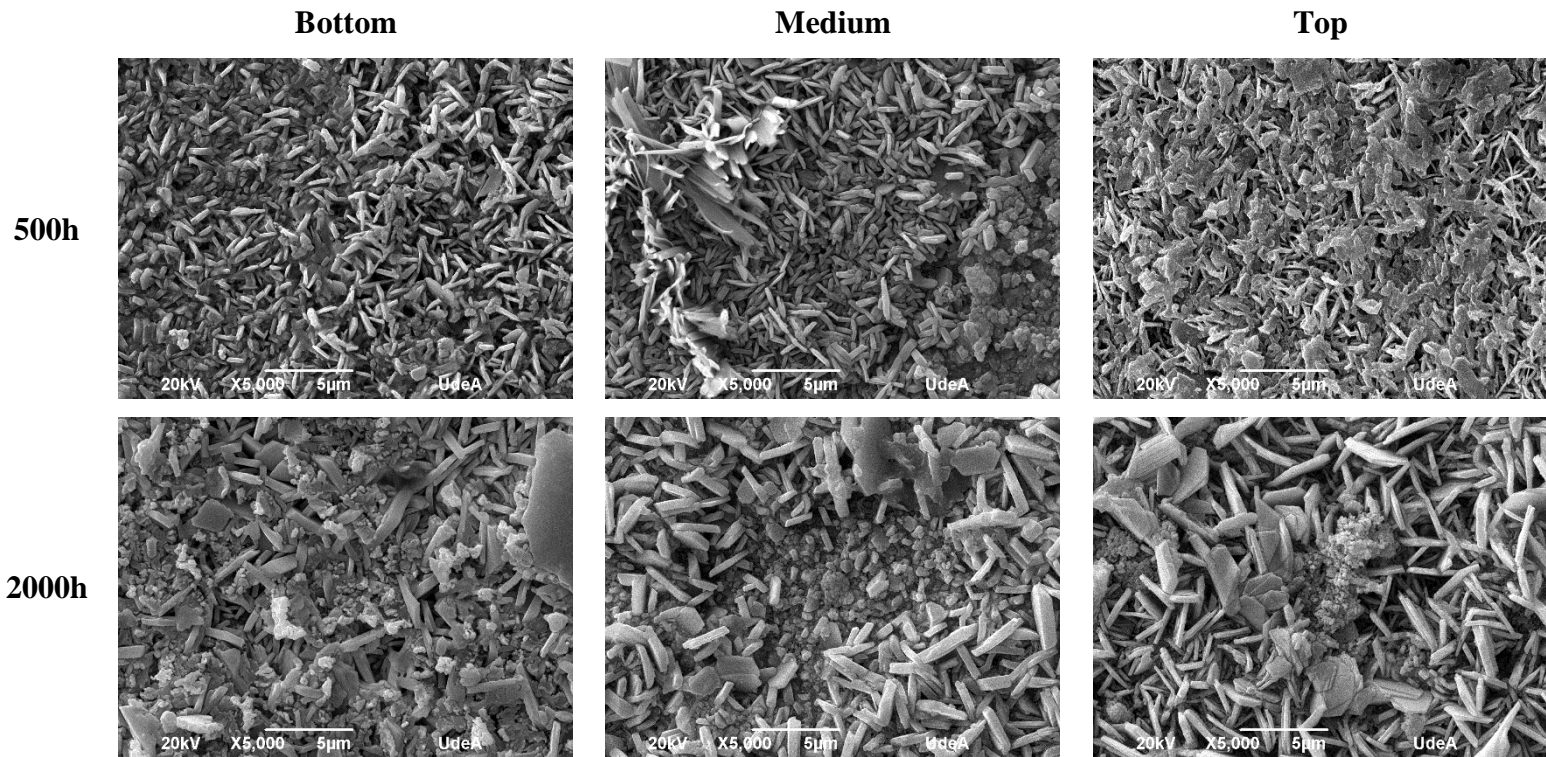


Figure 28. SEM images of the surface of metal samples in contact with MSBNF with 1.5 wt.% of Al_2O_3 after 500 h and 2000 h immersion test, in three different positions bottom, medium, and top.

To establish the distribution of the corrosion products across the surface of samples SEM analysis coupled with Energy-Dispersive X-ray spectroscopy (EDX) was performed. *Figure 29* and *Figure 30* show the SEM images of the cross-section of samples immersed during 500 and 2000 h in pure Hitec and MSBNF with 1.5 wt.% of Al_2O_3 nanoparticles, respectively. The samples immersed in pure Hitec have a thicker oxide layer (9.50 nm) compared to those obtained in the immersed in the nanofluid (6.08 nm). It is possible to observe by comparing the samples of both reactors, that the corrosion layer of the samples immersed in the nanofluid is more homogeneous and compact. These inner oxide layers adhered to the base metal indicated that the layer had a protective nature. However, the sample in the top position of reactor 2 showed a detachment of the inner layer. On the other hand, the samples after 2000 h of exposition in Hitec showed the presence of "spider" type oxides, this may indicate the presence of localized points of aggressive anions from the molten salt. However, the SEM image and EDX mapping in *Figure 32* appears homogenous with no indication of any attack through the grain boundaries, and therefore the intergranular corrosion was not observed, evidencing

uniform internal oxidation. There was not significant pitting in any of the samples evaluated, neither exposed to Hitec nor in the nanofluid.

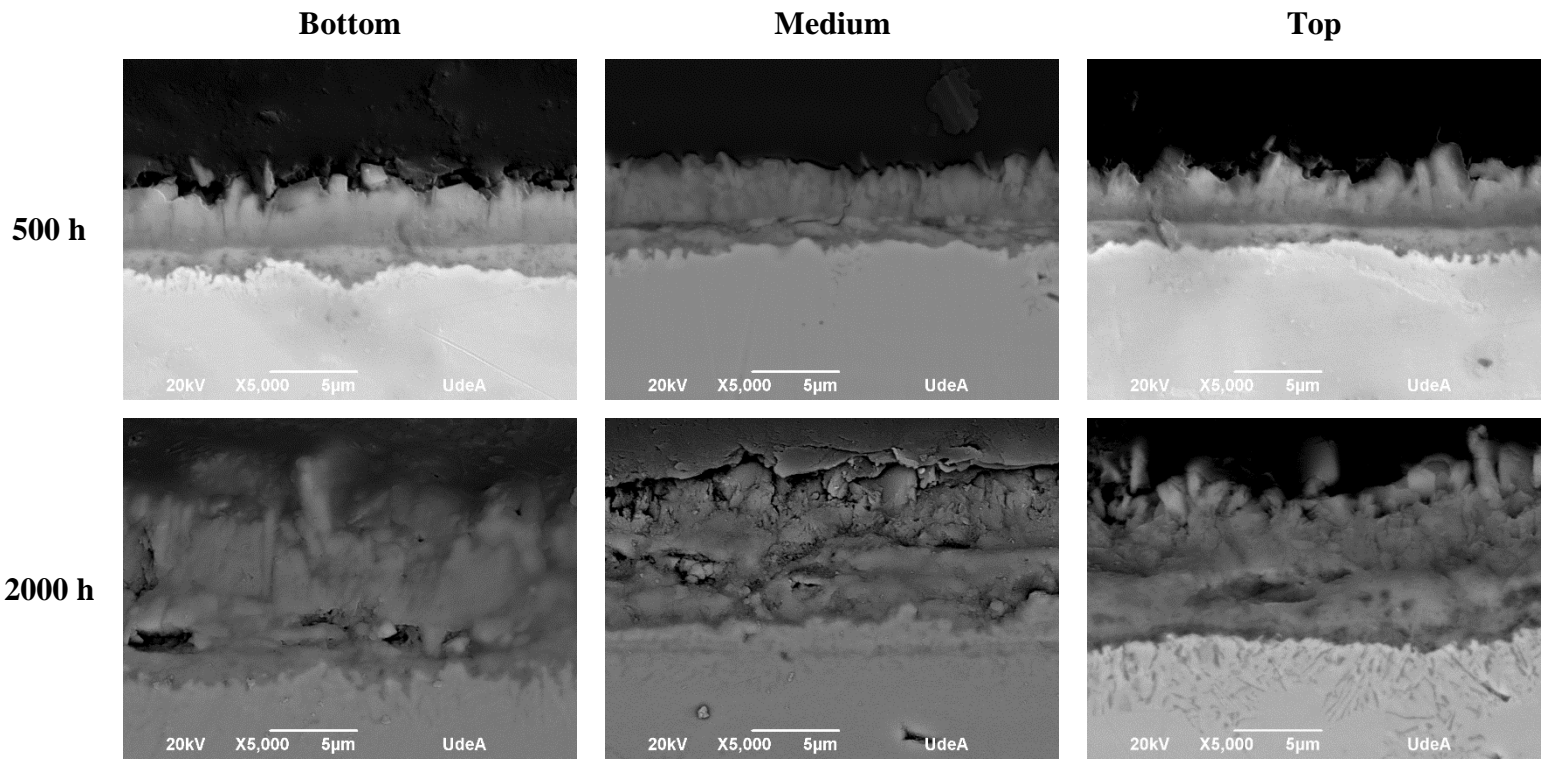


Figure 29. Cross-section of the metal samples in contact with the pure Hitec after 500 h and 2000 h immersion test, in three different positions bottom, medium, and top.

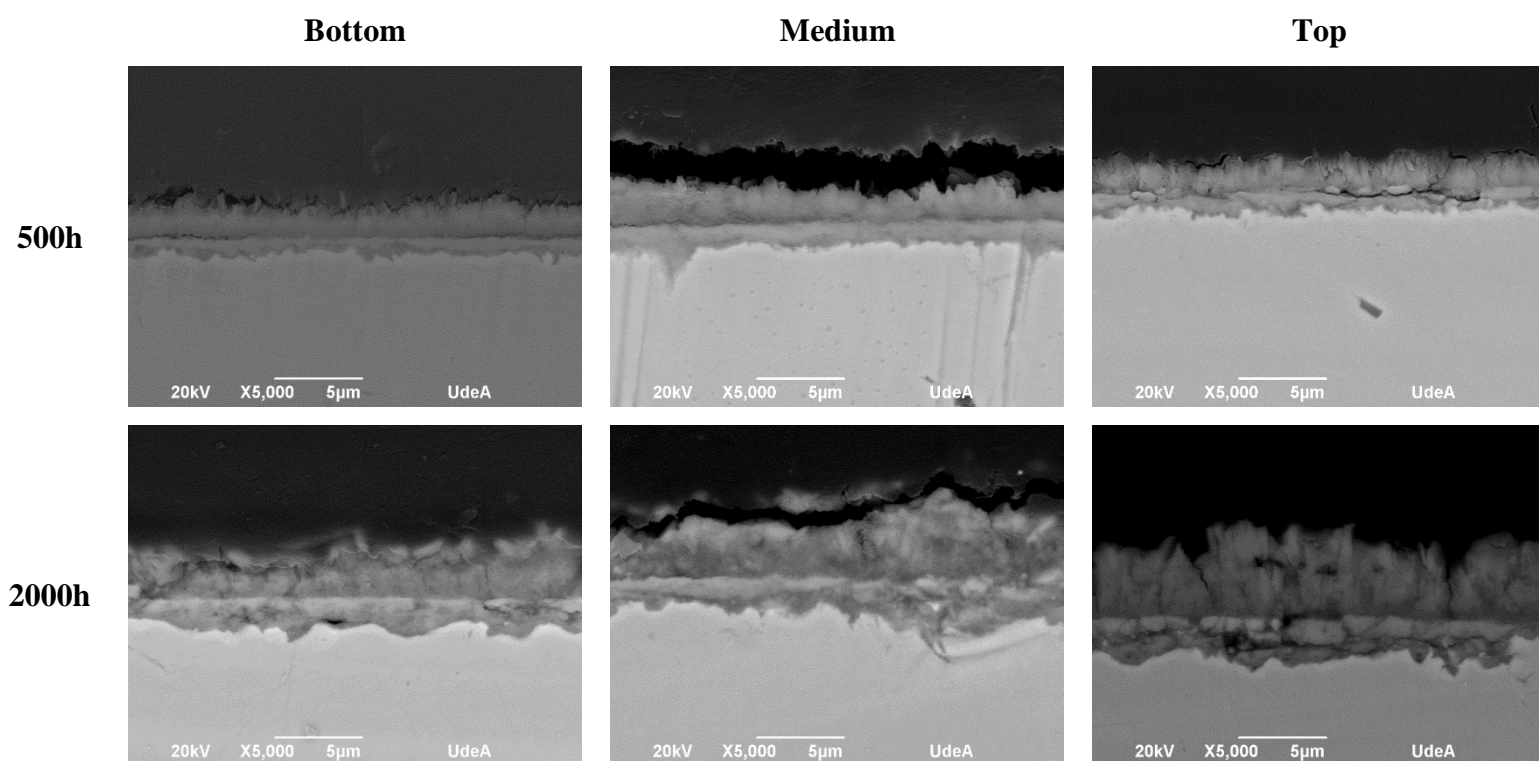


Figure 30. Cross-section of the metal samples in contact with the MSBNF with 1.5 wt.% of Al_2O_3 after 500 h and 2000 h immersion test, in three different positions bottom, medium, and top.

Figure 33 presents the detail of the cross-section SEM images of the SS304 specimens after 2000 h immersed in pure Hitec and MSBNF with 1.5 wt% of Al_2O_3 . The measured oxide layer corresponds to the thickest layers obtained. Taking into account the EDX results in *Table 16* and the EDX mapping of the samples immersed during 2000 h in both reactors, it is possible to observe that at the beginning the formation of a protective layer of chromium oxide was followed by a layer of sodium oxide, as other authors have shown [97], [101]. The position of this corrosion layer is shown in *Figure 33*. At the same time, the presence of nanoparticles within the corrosion layer was observed as mentioned before, which may be the cause of the ameliorated effect of the corrosion of samples immersed in the nanofluid [149]–[152]. Some authors even modify the amount of Nb in the molten salt, depending on the Ni and Al levels, looking for external protective scales of Al_2O_3 , which adds more protection qualities to Cr_2O_3 layers [151], [153], [154].

Despite the evidence in the XRD results of a less-protective layer of chromium in the samples immersed in the nanofluid after 672 h at 550°C, and the lack of the reports showing that the presence of nanoparticles influences the growth of different chromium oxide layers, such as those found in the

samples submitted to the nanofluid. It could be indicated that the alumina nanoparticles contribute to the growth of the spinel. The samples subjected to the nanofluid showed greater resistance to the inlay of the salt compared to the samples immersed in the pure Hitec salt. The presence of the main component of the salt (sodium nitrite NaNO_2) inside the corrosion layer of the samples immersed in Hitec was evident, which could cause the presence of aggressive anions that generate greater penetration of corrosion. This behavior could be confirmed with the presence of "spiders" shown in SEM images. The gravimetric test, i.e. gain and loss of mass, as well as the corrosion rate (discussed later), showed that the nanofluid had better behavior against corrosion, this could be related to the presence of nanoparticles within the corrosion layer, generating a more compact layer and therefore improving their corrosive behavior [151].

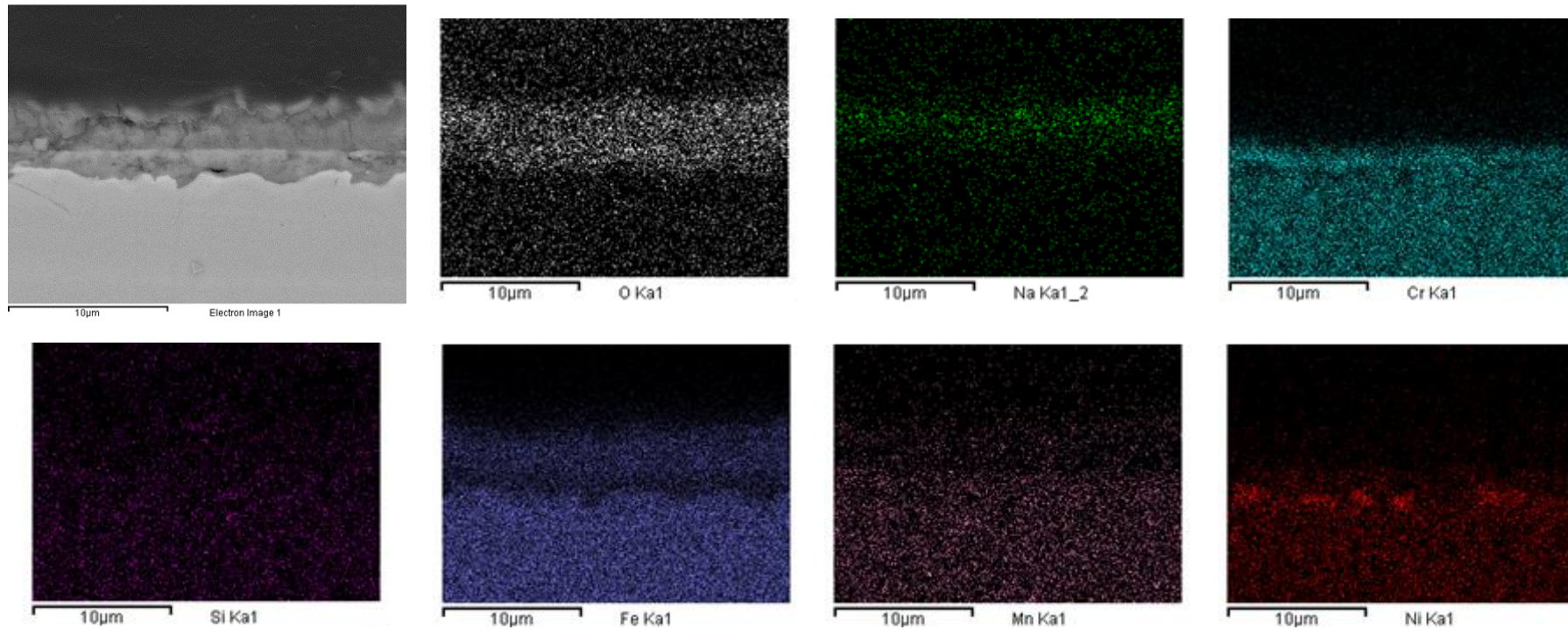


Figure 31. EDX mapping of SS304 surface after 2000 h of exposure time in MSBNF with 1.5 wt% of Al_2O_3 .

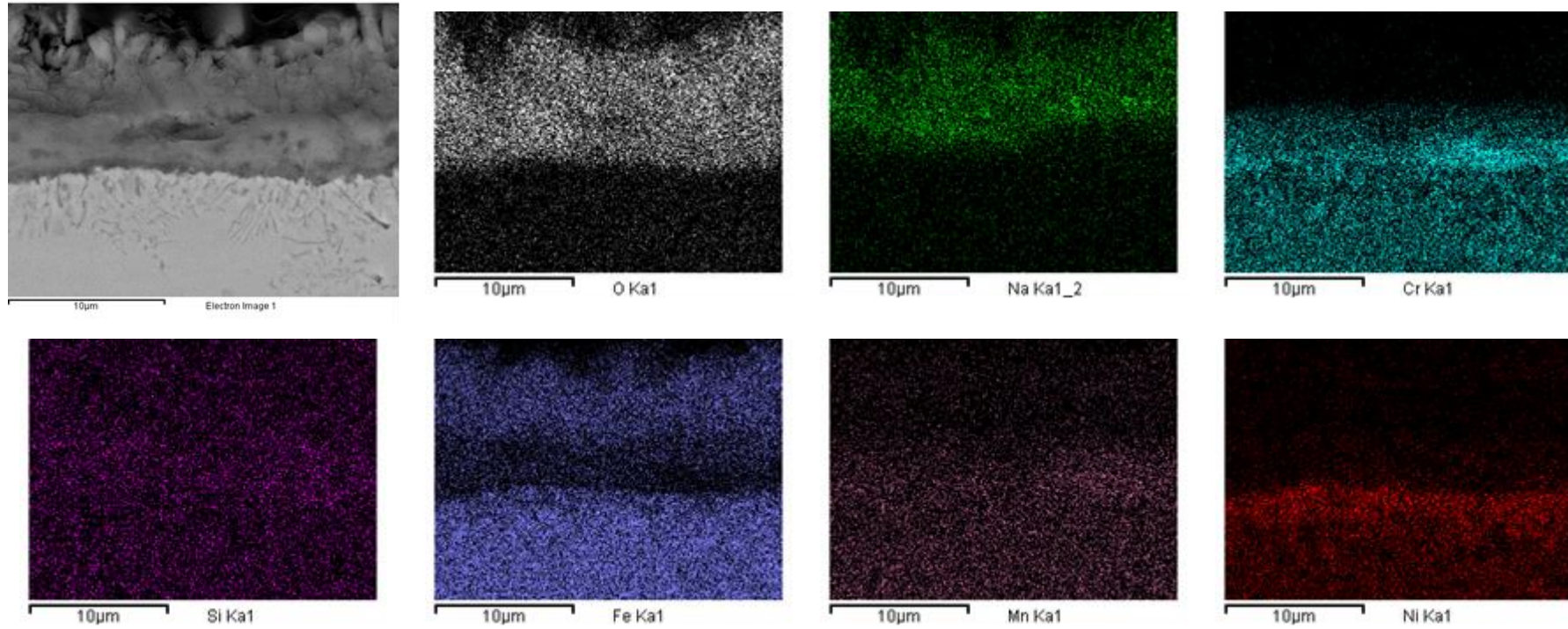


Figure 32. EDX mapping of SS304 surface after 2000 h of exposure time in Hitec.

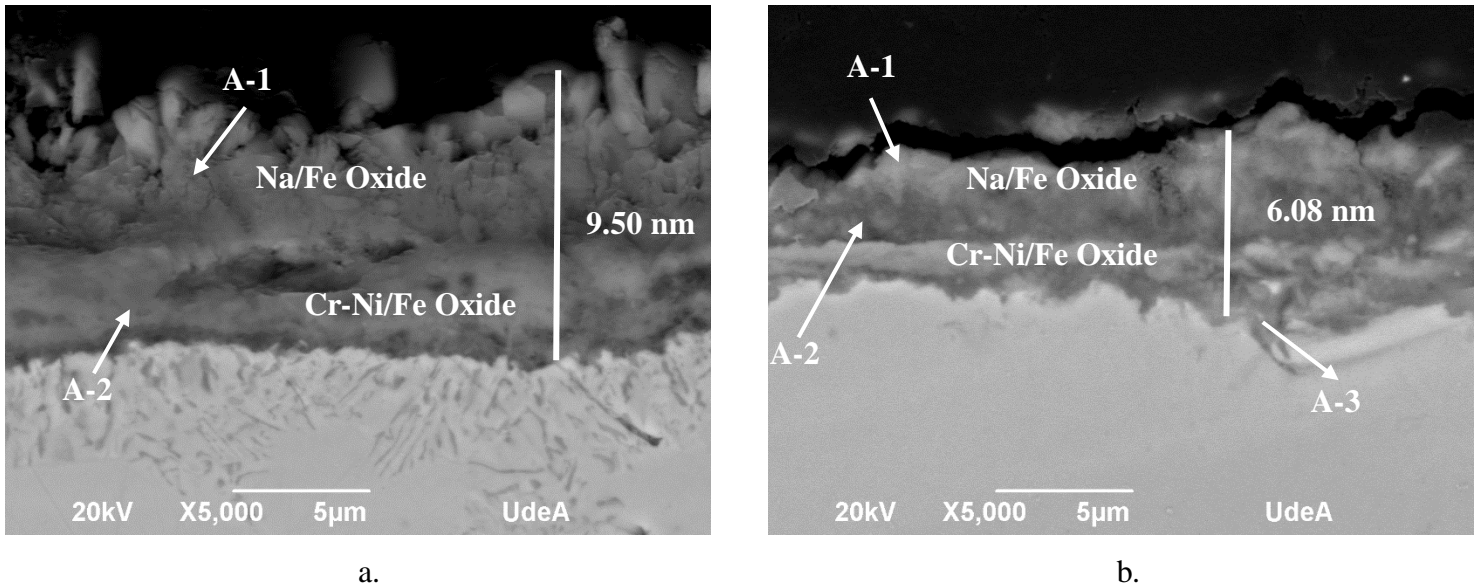


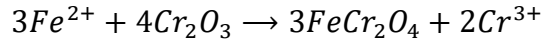
Figure 33. Detail of the cross-section of the SS304 specimens after 2000 h immersed into a. Pure Hitec and b. MSBNF with 1.5 wt% of Al_2O_3 .

Table 16. EDX results of the cross-section of the SS304 specimen after 2000 h immersed into pure Hitec and the MSBNF, where A-1, A-2 and A-3 are the areas evaluated by the EDX demarcated within the image.

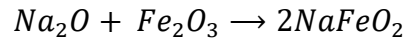
Fluid	Spectrum	O	Na	Cr	Mn	Fe	Si	Ni	Al	C
Hitec	A-1	25.04	12.44	1.24	0.78	60.5	-	-	-	-
	A-2	20.57	3.35	26.81	1.35	41.02	1.42	5.14	-	-
MSBNF	A-1	16.85	9.09	0.87	2.72	67.83	1.39	1.26	-	-
	A-2	10.96	5.47	3.91	-	74.88	1.88	1.98	0.93	
	A-3	1.67	-	14.86	1.32	55.75	0.48	8.59	-	17.32

According to the EDX and the XRD results for the samples immersed in Hitec and MSBNFs at 550°C from 24 to 2000 h, an oxidation process of SS304 in the presence of the salt and the nanofluid is proposed and shown in **Figure 34**. In the beginning, there is a migration of Fe and Cr to the metal surface forming the protective layer of chromium oxide, in the case of samples subjected to Hitec a simple layer of Cr_2O_3 is formed, while for the nanofluid the layer of FeCrO_4 spinel due the **Reaction 1**. These layers prevent the oxidation of the steel; however, given the effects of temperature, the critical percentage of Cr is lost with time; hence, the layer starts degrading and leading to the formation of the iron oxides layers, e.g. magnetite, hematite, and Fe_4O_5 . Finally, the sodium ferrite

may have its origin in the reaction between trace amounts of sodium oxide in the molten nitrate and hematite according to **Reaction 2** [148], [155].



Reaction 1



Reaction 2

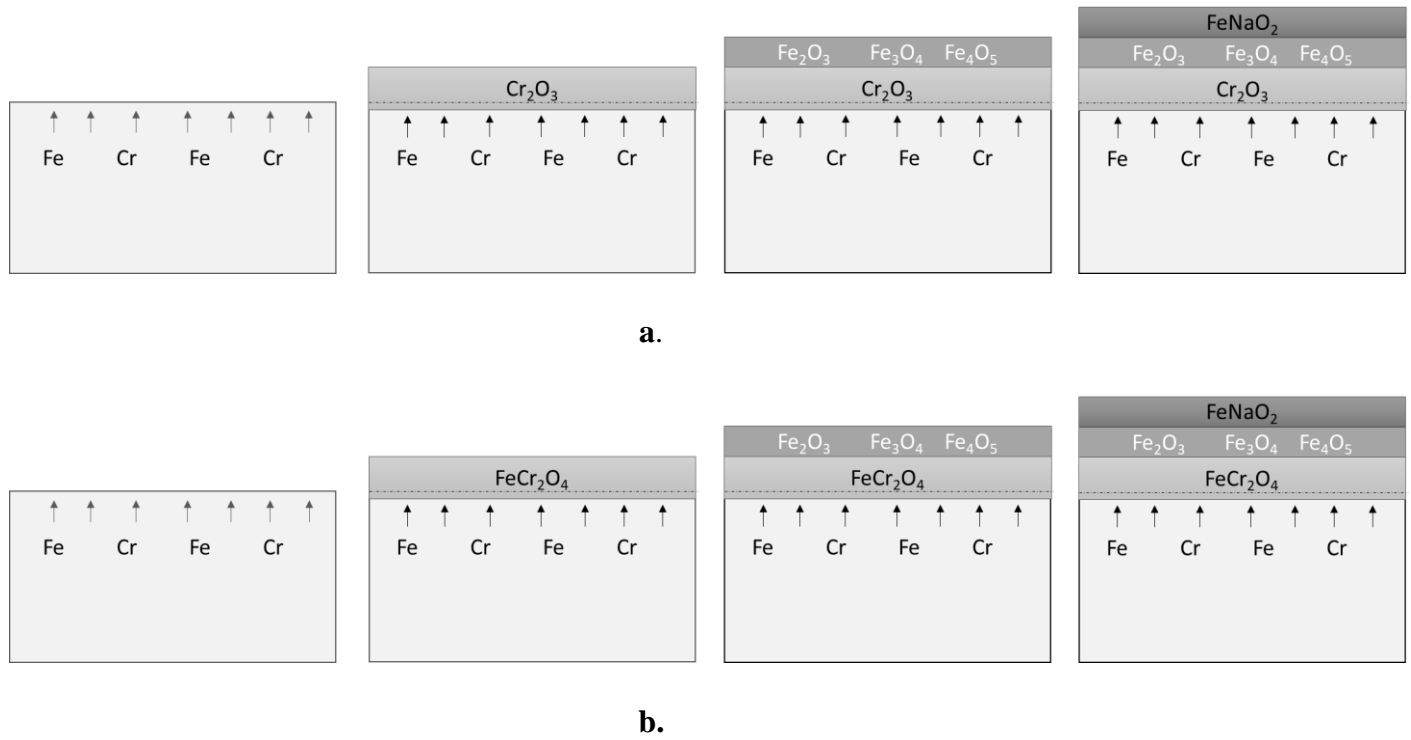


Figure 34. Proposed diagram of the oxidation process of SS304 immersed in a. Hitec and b. the MSBNF.

5.4.3 Mass Change and Corrosion Rate

To determine the mass gain and have control of the growth of the oxide layer over time, the gravimetric gain test at 550°C during 2000 h was performed, the results comparing the three different positions inside of each reactor, R1 with pure Hitec and R2 with MSBNF with 1.5 wt.% of Al₂O₃ nanoparticles, are shown in **Figure 35**.

Less than 1000 h after the start of the experiment, the corrosion produced by R1 was higher than the weight gain in R2 with alumina nanoparticles in all the positions evaluated. Nevertheless, after 1000 h, the rapid growth of corrosion was evident in both reactors, being greater for R2. However,

from 1000 h of exposure, the mass gain of R2 (with nanoparticles) was higher than R1 (pure Hitec). This behavior could be related to the first oxide layers formed, i.e. the spinel layer formed in R2, that, as demonstrated by XRD above, is more compact and stable compared to the chromium oxide layer found in R1 samples.

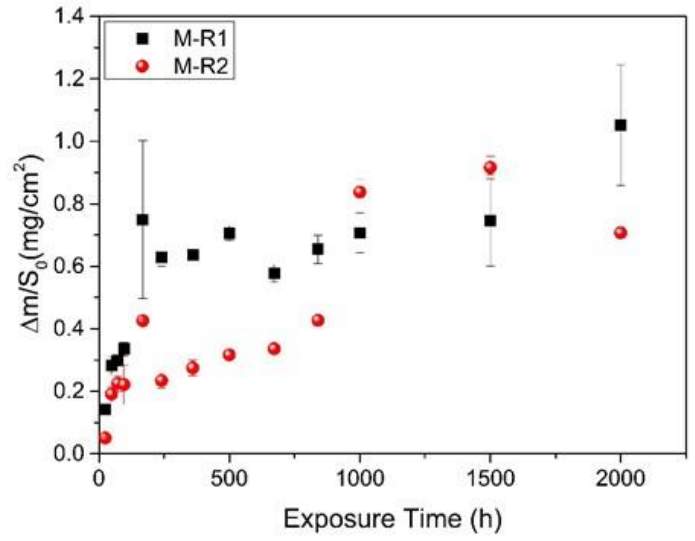
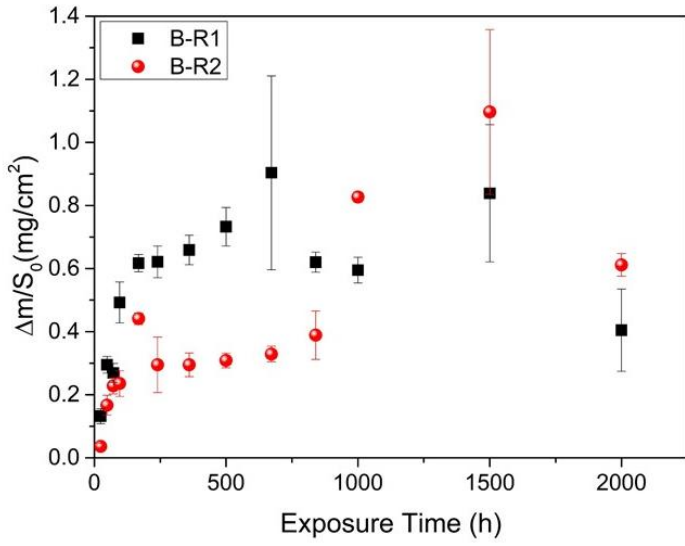
At the bottom of the reactors, R2 has a rapid growth in mass gain up to 1.10 mg / cm^2 at 1500 h of exposure followed by a rapid decrease in mass gain up to 0.62 mg / cm^2 at 2000 h, this behavior could be associated with a detachment of corrosion products. In R1, after a low reduction of the mass gain at 1000 h of exposure, rapid mass growth is reported up to 0.84 mg / cm^2 at 1500 h, followed by a rapid decrease in mass gain up to 0.40 mg / cm^2 at 2000 h, as in R2, this behavior can be associated to the detachment of the corrosion layer.

In the medium position of the reactors, **Figure 35 b**, the mass gain of R1 was almost constant up to 1500h of exposure followed by rapid growth until 1.05 mg / cm^2 , by the contrary, R2 showed rapid growth after 1000 h followed by a detachment of the corrosion products up to 0.71 mg / cm^2 . It is important to highlight that the mass gain in this work at the habitual conditions evaluated, that is, SS304 metal completely immersed inside the molten salt, was less than the reports in the literature. In the compilation of Gasia *et al.* [156] reported the corrosive behavior of the SS304 in contact with pure Hitec, the mass gain at 390°C was less than 1 mg / cm^2 and less than 3 mg / cm^2 at 550°C , while Villada in 2018 [97] informed a mass gain of 0.744 mg / cm^2 at 2000 h of exposure at the same temperature. On the other hand, Ma *et al.* [157], reported the effect on the corrosion of alumina nanoparticles obtained by the one-step method from Alumina Nitrate in Solar Salt; and after 432 h of testing at 565°C they obtained a mass gain of 0.39 mg / cm^2 less than that obtained by us but in much less time of holding.

It should be noted that there is no significant difference between the bottom and the medium positions, which could mean that the conditions were similar, that is, there is no large number of particles at the bottom of the reactor, and the MSBNF was stable during the test. The presence of alumina nanoparticles found in the salt aliquots collected during the test confirm this theory, see **Figure 36** for the SEM and EDS images of the aliquot of MSBNF from the reactor after 2000 h of exposure.

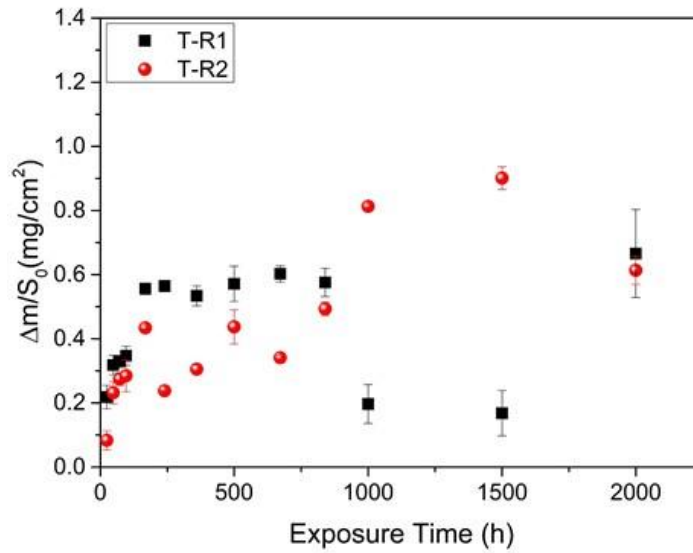
On the other hand, the behavior is different at the top position in the reactor, where half of the sample is immersed in the salt and half is above the level in order to assess the influence of the possible gases released by the salt. The mass gain of the R1 was almost constant up to 840 h time experiment, then,

a marked decrease in mass gain was observed, followed by a rapid recovery up to 0.67 mg / cm^2 . Contrarily, R2 presented a continuous increase of mass gain up to 1500 h of exposure with a rapid decrease at 2000 h with a mass gain of 0.61 mg / cm^2 , this behavior can be related to the detachment of the layer formed so far; hence, knowing that the layer in R2 had a progressive growth up to 1500h, this layer is more stable than the layer formed in R1. It is important to highlight that although part of these samples was above the salt, and having the possibility of generating different corrosion products and increasing the mass gain, the samples in this position in R1 had a lower gain compared to the other positions evaluated. Meanwhile, the behavior of the samples in this position in R2 was similar to the other positions. Taking this into account, it could be said that there was no influence of possible gases released by the salt.



a.

b.



c.

Figure 35. Gravimetric gain test at 550°C during 2000 h of the Molten salt Hitec (R1) and the MBSNF with 1.5 wt.% of Al₂O₃ (R2) a. in the bottom (B), b. in the medium (M) and c. in the top (T) of the reactor.

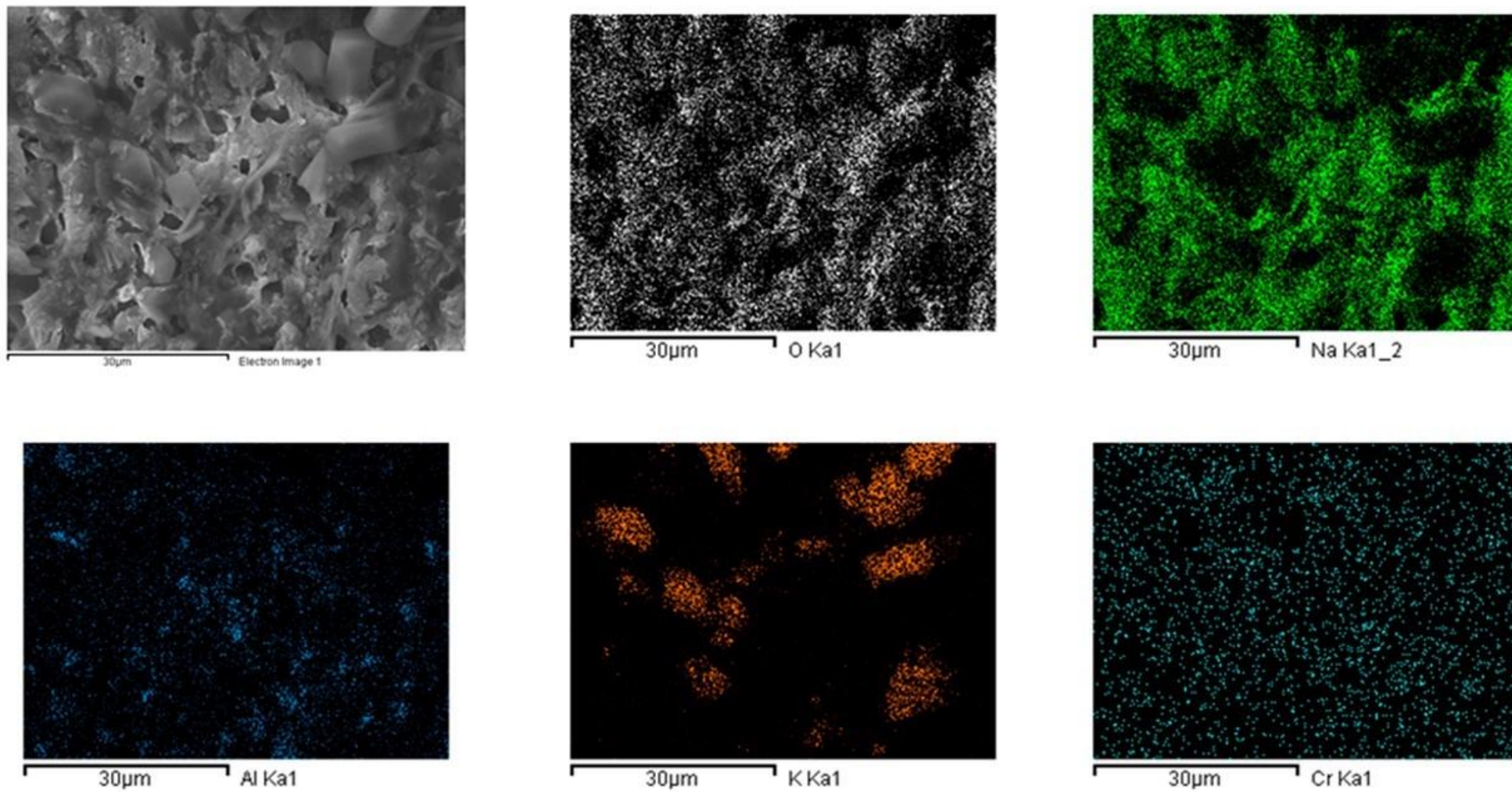
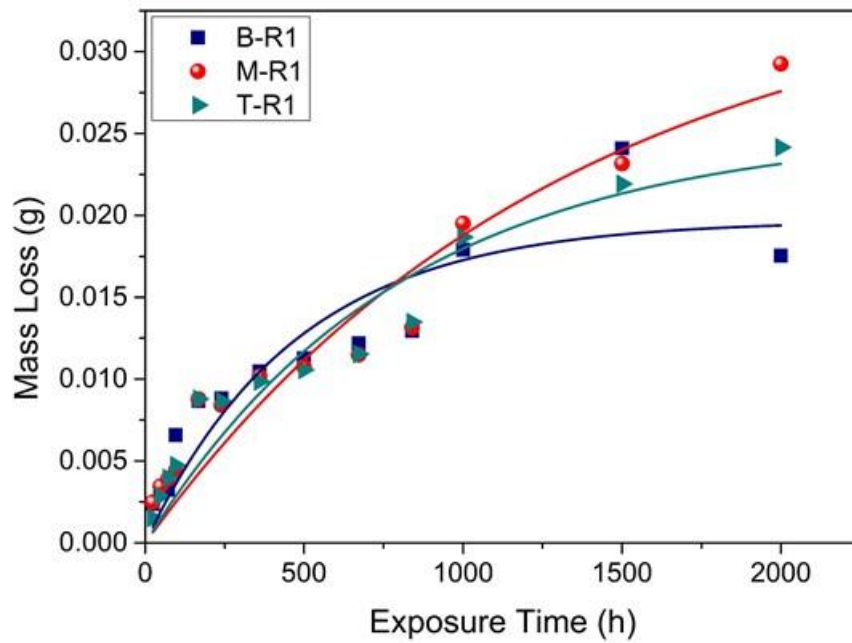


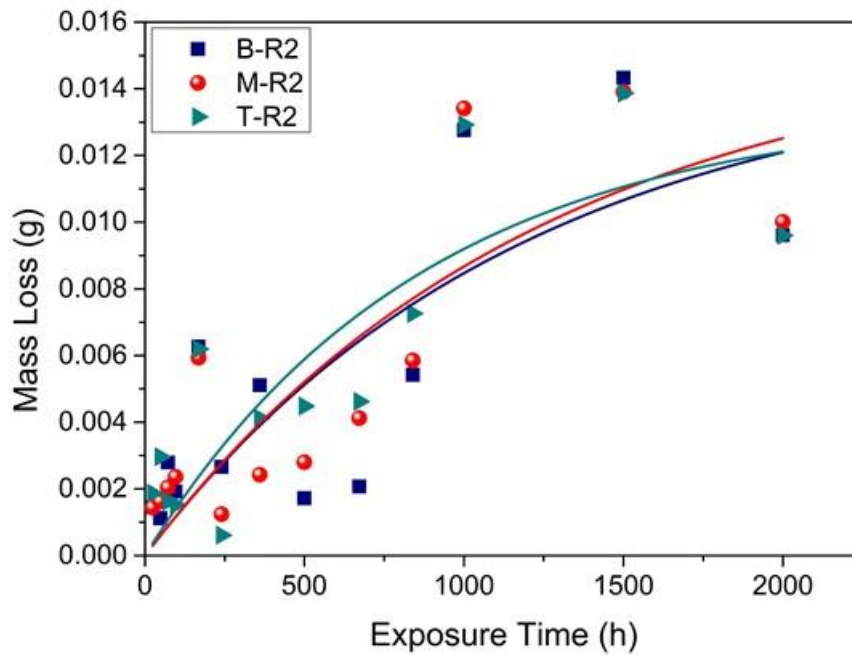
Figure 36. SEM image and EDX mapping of aliquot at 2000 h of exposure of MSBNF in the reactor.

Figure 37 shows the average mass loss with their respective trend line estimated using the non-linear model BoxLucas, from three samples for every exposure period at three different positions, bottom, medium, and top for both R1 (pure Hitec) and R2 (MSBNF with 1.5 wt.% of Al₂O₃ nanoparticles). Every sample was weighted after immersion in HNO₃ solution to remove the corrosion products attached to the SS304 samples, and then, cleaned with a light brushing several times, according to ASTM G1-03. The mass loss of the samples is consistent with those obtained by mass gain, that is, the mass loss was lower for the samples submerged in the nanofluid compared to those immersed in pure Hitec, for all the positions evaluated. Compared with the mass loss results with the gravimetric gain, the first one was more conclusive considering the gravimetric gain test had a higher variability given layer detachments during the process.

In R1 the mass loss had a rapid increment up around to 360 h of exposure, in the case of the bottom position after 1000 h the mass loss begins to stabilize reaching a maximum of 0.019 g, while in the medium and top positions after 2000 h a stabilization was not obtained, being greater the mass loss in the medium position. Regarding R2, a constant increment of mass loss can be observed for the three positions evaluated, in the top position a slight increase in mass loss up to 1500 h compared with the other position was observed. For R2, the mass loss during the total time of exposure agreed with the behavior of mass gain measurements. Similar behavior in the three positions evaluated was observed, which could represent that the part of the nanofluid stability was preserved thanks to the constant movement inside the reactor.



a.



b.

Figure 37. Mass loss of corroded samples immersed during 2000 h in three different position bottom (B), medium (M), and top (T), in **a.** Hitec (R1) and **b.** MBSNF with 1.5 wt.% of Al₂O₃ (R2).

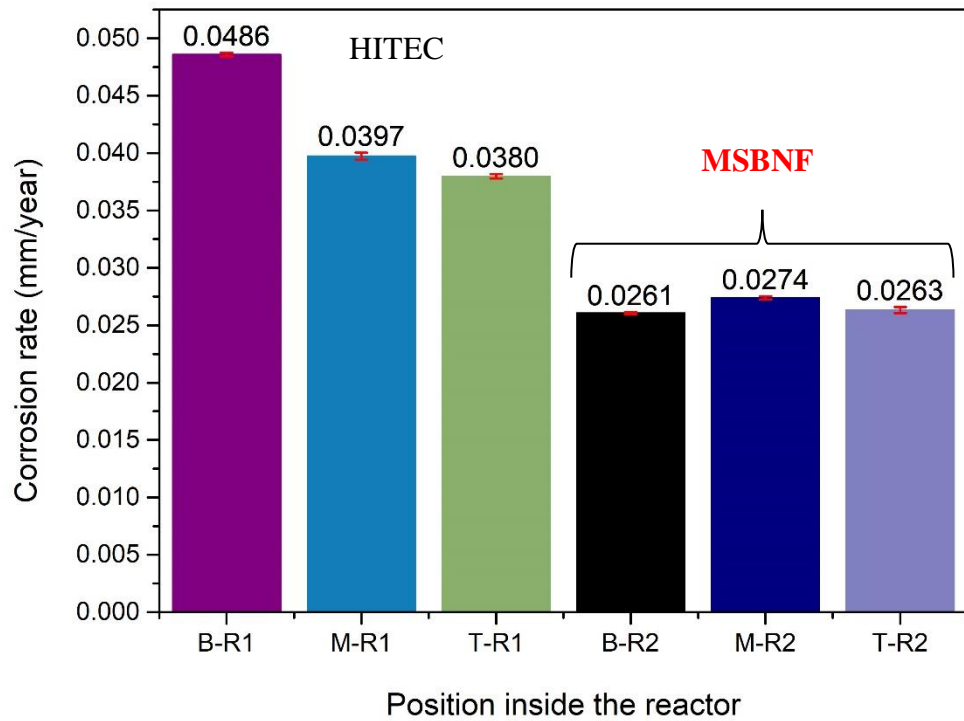
It is important to highlight that the corrosive behavior for SS304 was higher in contact with pure Hitec (R1) compared to the MSBNF with 1.5 wt.% of Al₂O₃ (R2) after 2000 h of exposure, according to both gravimetric, gain and loss mass, tests. These results can be checked with the assessment of the corrosion rate, **Figure 38 a.** after 1000 h and **b.** after 2000 h time of the experiment. In both results, R2 presented a corrosion rate remarkably lower. It is clear that the corrosion rate is not influenced by the position inside the reactor when MSBNF is used, for 1000 h and 2000 h, obtaining a corrosion rate of 0.0274 mm / year at 1000 h and 0.0097 mm / year at 2000 h, as the highest values. In the same way, the corrosion rate decrease with time of exposure for all the samples evaluated, as usual in corrosion tests when protective layers are formed. Recently, Ma *et al.* [157] reported the behavior of a solar salt nanofluid with alumina nanoparticles obtained by the one-step method from Aluminum Nitrate, for which after 432 h of immersion at 565°C. They obtained a corrosion rate of 0.01 mm / year, higher than ours obtained in similar conditions but with a longer immersion time.

Few reports in the literature have informed the effect of nanoparticles on corrosive salt behavior. Padmanaban y Schuller *et al.* [98], [99] evaluated the effect of SiO₂ nanoparticles on the corrosion rates for binary carbonate salt (42.7 % Li₂CO₃-K₂CO₃) showing a reduction of the corrosion rate. On the other hand, Fernandez *et al.* [101] showed that compatibility depends on the type of nanoparticle used; that is, with silica nanoparticles, the corrosion rate was not affected, while the alumina nanoparticles increased the protection of the corrosion produced by molten salts.

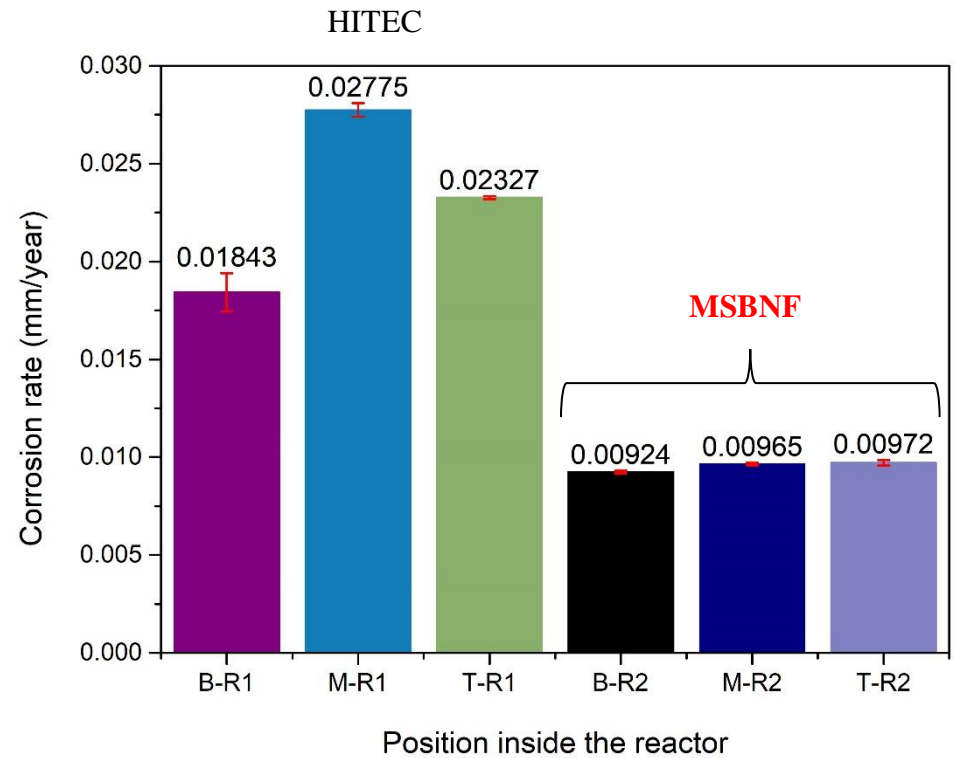
On the contrary, Grosu *et al.* [100] informed an increment of the corrosion rate given the formation of microbubbles of air trapped in between nanoparticles using Hitec XL as fluid and alumina and silica as nanoparticles, as well as the presence of the nanoparticles in the corrosion layer. However, the temperature evaluated in Grosu's research was lower compared to the temperature studied here. Recently, Nithiyantham *et al.*, [102] reported the corrosive behavior of the Solar Salt with the addition of alumina and silica nanoparticles, at 310°C and 390°C. The use of nanoparticles had a positive effect on the corrosive behavior of the molten salt with the incorporation of the nanoparticles in the corrosion layer, reducing the corrosion rate.

The results reported here agree with Nithiyantham *et al.*, [102]. The use of the nanoparticles had a positive effect, evidenced by the incorporation of stable oxides layer as well as the presence of nanoparticles inside the corrosion layer which led to the reduction of corrosion rates compared to pure Hitec. **Figure 39** shows the SEM image and EDX mapping obtaining in the SS304 surface after 2000 h of exposure in MSBNF with 1.5 % of Al₂O₃ in the top position, where it is evident the presence

of Al₂O₃ nanoparticles. In the same way, **Figure 40** shows the SEM images of the SS304 cross-section after 2000 h of exposure and their EDX for the medium position, where it is possible to observe the presence of alumina nanoparticles in the corrosion layer. According to Nithiyantham *et al.* [102], the presence of alumina nanoparticles in the corrosion layer formed a passive layer acting as a corrosion inhibitor. Due to the physical and chemical incorporation of nanoparticles, the corrosion rate decreases if compared to the pure Hitec [149]–[152]. Additionally, according to the results of XRD and the evaluation of corrosion, the presence of nanoparticles may contribute to the formation of the spinel (FeCr₂O₄) in the samples immersed in the nanofluid. This layer, although some authors consider it less protective, in this system seems to be one of the causes for the ameliorated corrosive behavior of the nanofluid. So it could be said that it is more protective and stable compared to the oxide layer formed in the samples immersed in Hitec. This behavior can be verified due to the presence of spiders in the corrosion layer of the samples subjected to the Hitec salt, as well as the main component of the salt and the difference in thickness of the corrosion layer. This may indicate that the simple chromium layer is not stable in salt and therefore less protective.



a.



b.

Figure 38. Corrosion rate of the pure Hitec and MSBNF with 1.5% Al₂O₃, a. 1000 h and b. 2000 h of exposure time

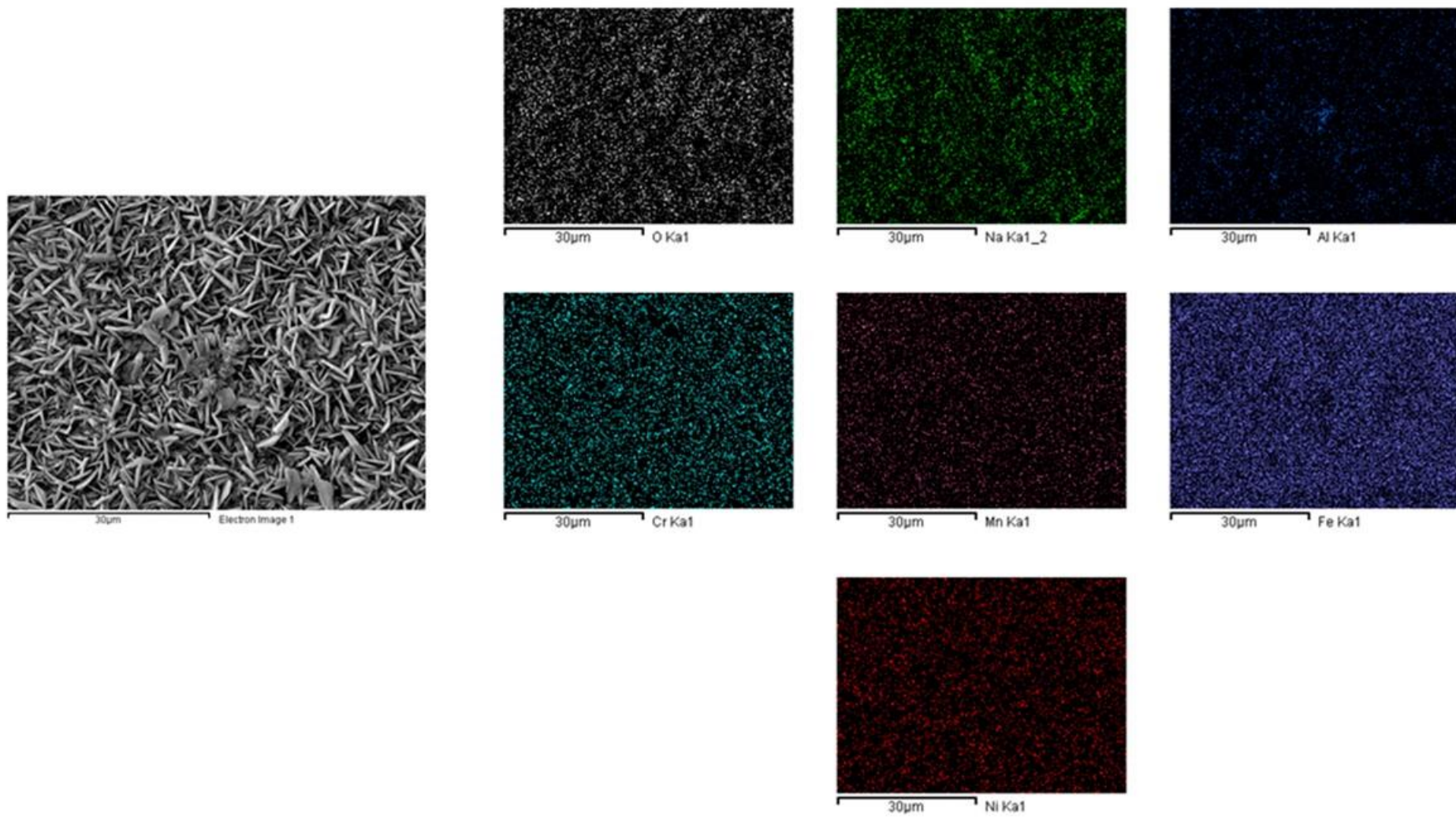


Figure 39. SEM image and EDX mapping of SS304 surface after 2000 h of exposure time in MSBNF with 1.5 wt.% of Al_2O_3 in the top position.

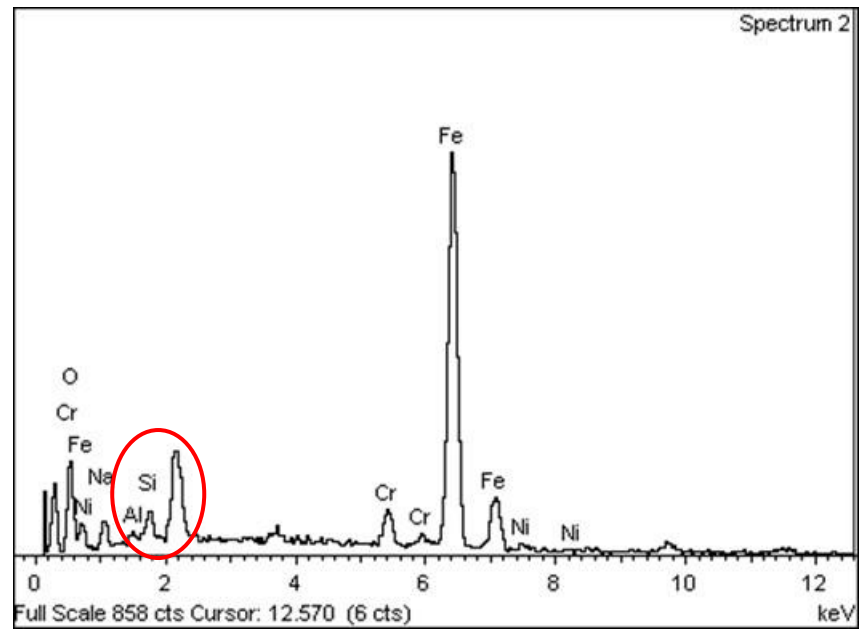
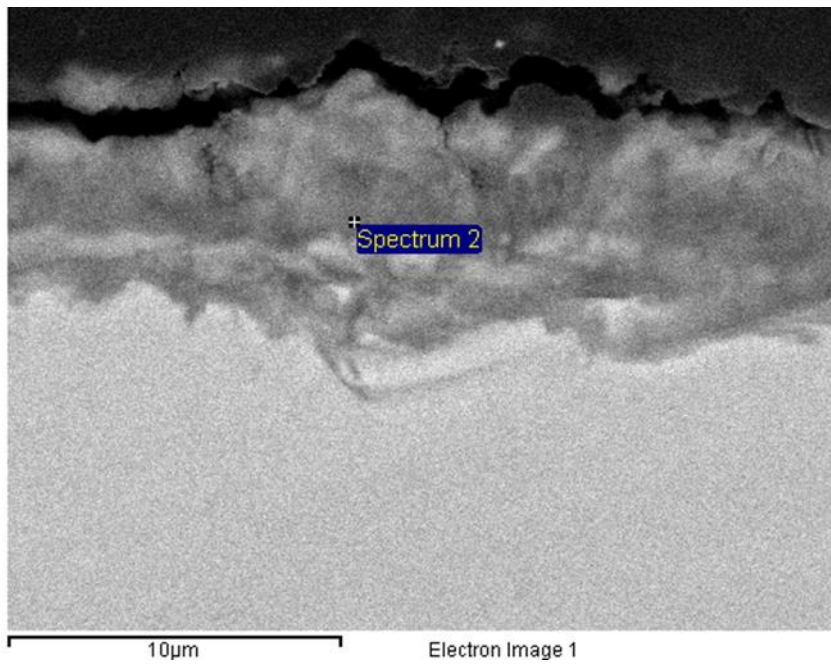


Figure 40. SEM image and EDX analysis of SS304 sample after 2000 h of exposure time in MSBNF with 1.5 wt.% of Al_2O_3 in the medium position.

5.5 Conclusion

Considering the corrosive nature of the salts in contact with the metals used in the manufacture of storage tanks in CSP plants, the selection of the metals and the design of the molten salts are important to minimize the effects of corrosion. Therefore, in this research, the evaluation of the corrosive behavior of the pure Hitec and the MSBNF with 1.5 wt% of alumina nanoparticles synthesized with the traditional two-step method (TM) was performed with the aim understand the effect of the addition of solid particles on the aggressive nature of the molten salt.

By XRD analysis and Rietveld refinement, the formation of different protective chromium layers was evidenced for the samples immersed in Hitec after 672 h at 550°C compared to the samples submitted to the nanofluid. A spinel layer of FeCr_2O_4 was observed in the samples immersed in the MSBNF, given the results obtained after the evaluation of corrosion, this layer could be more protective compared to the oxide layer formed in the samples exposed to Hitec; which together with the embedded nanoparticles inside the corrosion layer and by forming a denser layer, mitigated the aggressiveness of the salt.

Moreover, the main component of the salt, sodium nitrite (NaNO_2), was found in the corrosion layer of the sample immersed in Hitec, this result and the SEM images where the “spider” morphology was observed, could indicate greater fouling of the salt in these samples compared to the samples immersed in the nanofluid, causing the presence of aggressive anions that generate greater penetration of corrosion. This behavior could indicate that the spinel layer evidenced in the samples immersed in the MSBNFs is more resistant to salt penetration compared to the simple oxide layer found in samples exposed to Hitec. In the same way, there was no indication of pitting or any attack through the grain boundaries, and therefore intergranular corrosion was not observed, evidencing uniform internal oxidation for both samples immersed in pure Hitec and the MSBNF.

According to the gravimetric results of both gain and mass loss, as well as a lower corrosion rate at both 1000 and 2000h of exposure, a less aggressive character of the nanofluid in contact with the SS304 steel was obtained compared to the Hitec. This behavior can be given by the inclusion of alumina nanoparticles in the corrosion layer, generating a more compact layer. It should be noted that

the values of gravimetric gain in both evaluated fluids were lower than those reported by other authors, although in our case the samples were subjected to a higher temperature.

On the other hand, the stability through time of the MSBNF was determined thanks to the similar results obtained from the bottom and medium position as well as the presence of nanoparticles in the corrosion layer after 2000 h of exposition, this stability was established thanks to the mechanical agitation throughout the test. In this way, by using a minimum agitation it could be possible to guarantee the nanofluid character at all times when used as a storage fluid in CSP plants.

5.6 Pure Hitec and MSBNF with 1.5%Al₂O₃ evaluation after corrosive behavior test

Both pure Hitec and the MSBNF with 1.5 wt.% of Al₂O₃ were examined after the corrosion test in order to check for any degradation phenomena and the presence of corrosion products. So, the melting point, SEM images, Raman spectrometry, and DRX were performed.

5.6.1 Melting point evaluation

After subjecting Hitec and the MSBNF for 2000 h cycling between 550 and 160°C at each removal of metal samples from the reactors during the evaluation of aggressiveness, the melting point was measured to establish the stability with time of this property in the time. **Table 17** shows the melting point and heat of fusion of the Hitec and the MSBNF. Regarding the results of the pure salt, there was evidence of a reduction in both the melting temperature up to 5.56 % and the heat fusion, while for the nanofluid the behavior was opposite, that is, the melting temperature and heat of fusion increased up to 5.93 % and 23.5 % respectively. The different behavior of the MSBNF compared with the pure Hitec can be related to the particle agglomeration during the corrosive behavior test [158]. In the same way, the melting point can be affected by the presence of corrosion products in the molten salt. Different results have been reported in the literature corresponding to the enthalpy changes with the addition of the nanoparticles in the molten salt. Lasfargues et al. [158] reported an increment of the enthalpy with 1 % of TiO₂ nanoparticles, by the contrary, with 1 % of CuO, the enthalpy decreased compared to the base salt. On the other hand, Nithiyantham et al. [102] showed that SiO₂ and Al₂O₃ had no significant effect on the enthalpy of the solar salt after 1500 h of the corrosion test at 390°C.

Table 17. Melting point of pure Hitec and MSBNFs after the corrosive behavior test.

Sample	Melting Point (°C)	Change Percentage (%)	Standard Deviation	Onset (°C)	Endset (°C)	Heat of Fusion (J/g)
Hitec (H)-initial	145.38	-	0.53	139.36	148.95	85.43
Hitec -500 h	137.29	-5.56	1.68	127.50	143.34	72.89
Hitec-1000 h	144.73	-0.44	0.67	139.36	148.81	82.00
Hitec-1500 h	145.33	-0.03	0.29	139.48	149.70	80.10
Hitec- 2000 h	141.86	-2.42	6.08	135.56	147.95	78.50
H+1.5% Al ₂ O ₃ -initial	139.45	-	0.84	129.81	145.95	71.81
H+1.5% Al ₂ O ₃ -500 h	146.81	5.28	0.41	141.19	153.90	88.69
H+1.5% Al ₂ O ₃ -1000 h	147.17	5.54	0.26	141.04	154.60	74.73
H+1.5% Al ₂ O ₃ -1500 h	147.58	5.83	0.66	141.53	155.38	81.11
H+1.5% Al ₂ O ₃ -2000 h	147.71	5.93	0.63	141.43	156.19	81.38

5.6.2 Scanning Electron Microscopy SEM

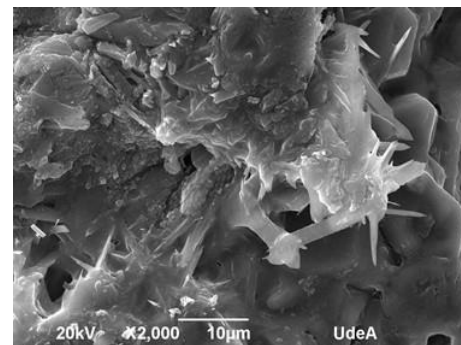
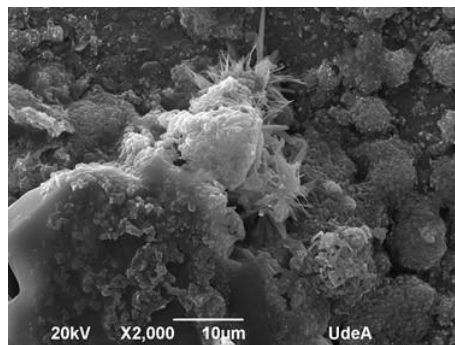
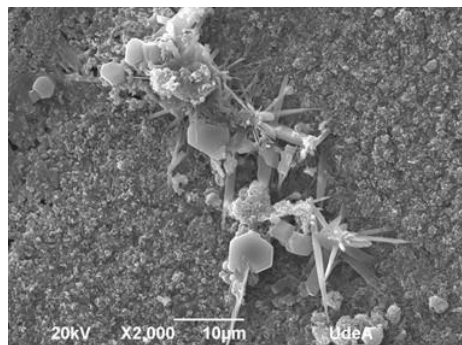
Figure 41 shows the SEM analysis of the Hitec and the MSBNF after the corrosive behavior test for 1000 h, 1500 h and 2000 h, different microstructures of the solidification were evident after comparing the pure salt and the nanofluid images. However, all of these microstructures correspond to the element of the molten salt, that is, Na and K, this result can be checked with the EDX mapping in *Figure 42*. In the same way, in the EDX mappings was possible to observe the presence of chromium as a corrosion product, this impurity in both Hitec and the MSBNF may be responsible for the changes obtained in the thermal properties of the aliquots evaluated.

1000 h

1500 h

2000 h

HITEC



MSBNF

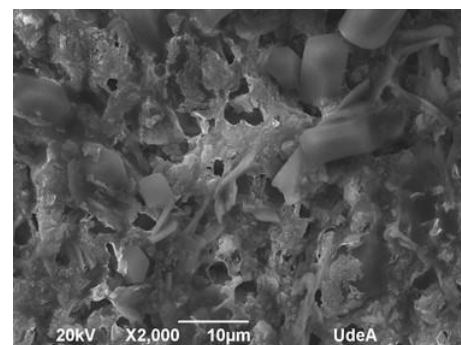
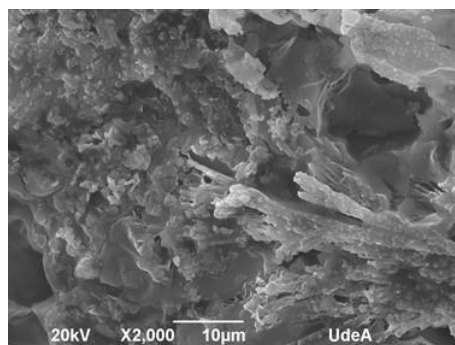
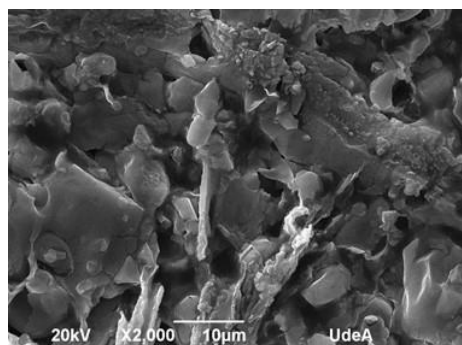


Figure 41. SEM images of the aliquot of Hitec and MSBNF from the reactor after 1000, 1500, and 2000 h of corrosive behavior test.

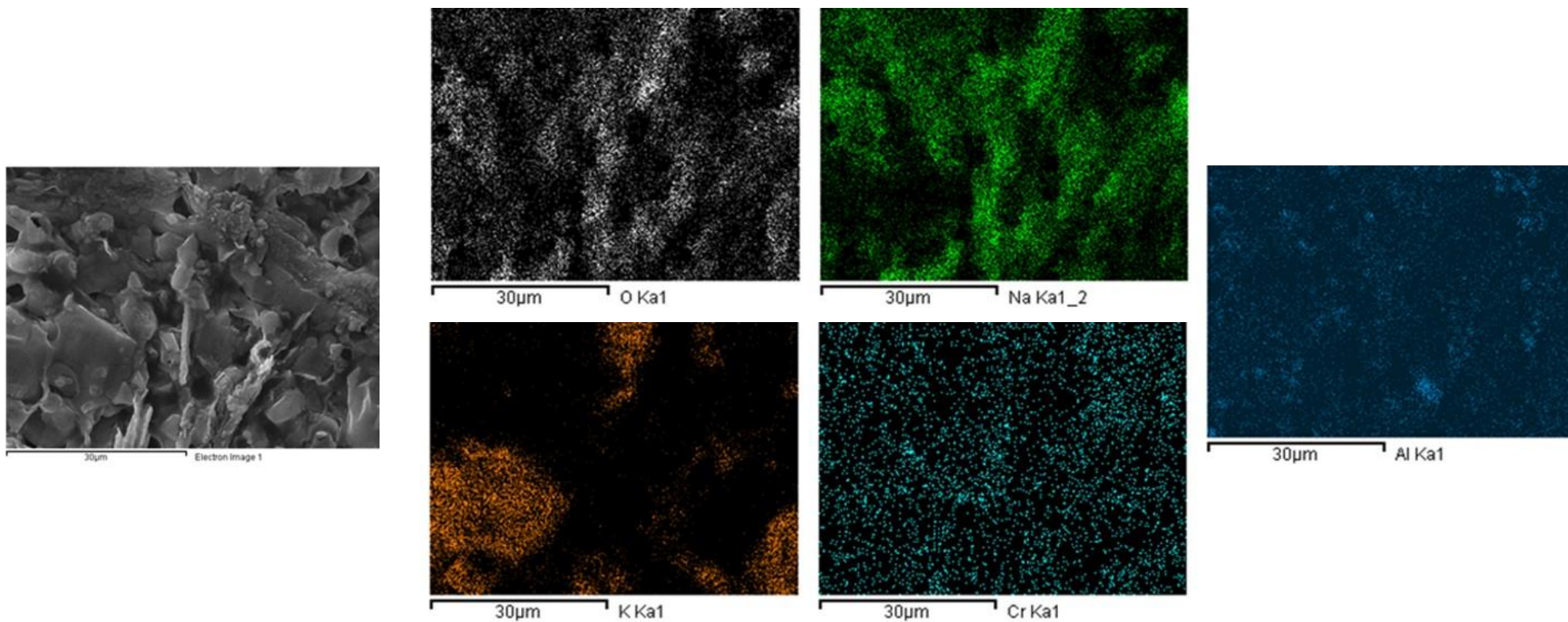


Figure 42. SEM image and EDX mapping of the aliquot of MSBNF from the reactor after 1500 h of corrosive behavior test.

5.6.3 Raman Spectrometry of the pure Hitec and MSBNF during the corrosive behavior test

In order to determine the chemical changes in pure Hitec and the MSBNF with 1.5 wt.% of Al_2O_3 after the corrosive behavior test at 550°C under N_2 atmosphere for 2000 h, Raman spectrometry was performed. *Figure 43* shows the Raman spectra of pure Hitec and *Table 18* the Raman band shifting of its salts: NaNO_3 , KNO_3 , and NaNO_2 . Similarly, *Figure 44* presents the Raman spectra of the MSBNF with 1.5 wt% of Al_2O_3 , it is important to highlight that given the low concentration of nanoparticles within the nanofluid, it was difficult to obtain a spectrum where the presence of nanoparticles was evident. However, *Figure 44 a.* shows the presence of nanoparticles thanks to the characteristic doublet bands of alpha-alumina with a strong band in 1372 and 1401cm^{-1} [159].

Figure 45 shows the Raman spectrum of the pristine alumina nanoparticles used for the synthesis of the MSBNFs. The characteristic bands of the molten salt components were found in both Hitec and the nanofluid, which means that these are not affected strongly by the presence of nanoparticles, especially the strong absorption of nitrate ion between $1000\text{-}1200\text{ cm}^{-1}$, which is less intense between $700\text{-}800\text{ cm}^{-1}$ and $1300\text{-}1400\text{ cm}^{-1}$. As well as the bands corresponding to the nitrite ion, between $150\text{-}160\text{ cm}^{-1}$, $826\text{-}832\text{ cm}^{-1}$, and the strongest between $1327\text{-}1331\text{ cm}^{-1}$ [160], [161].

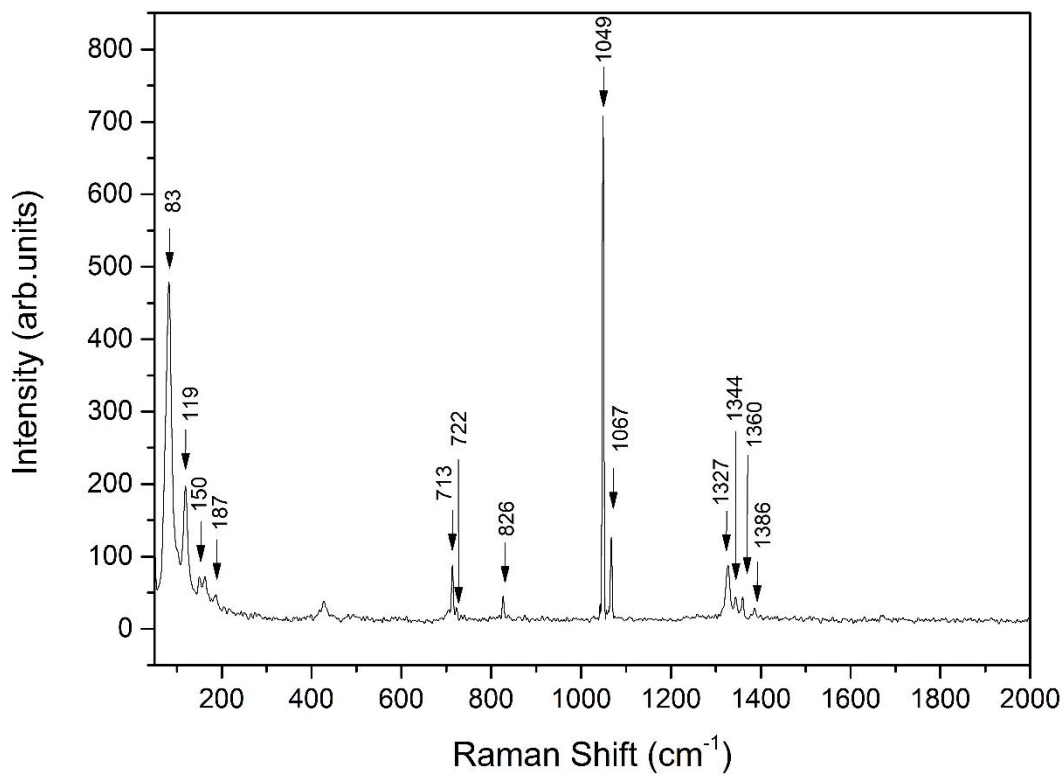
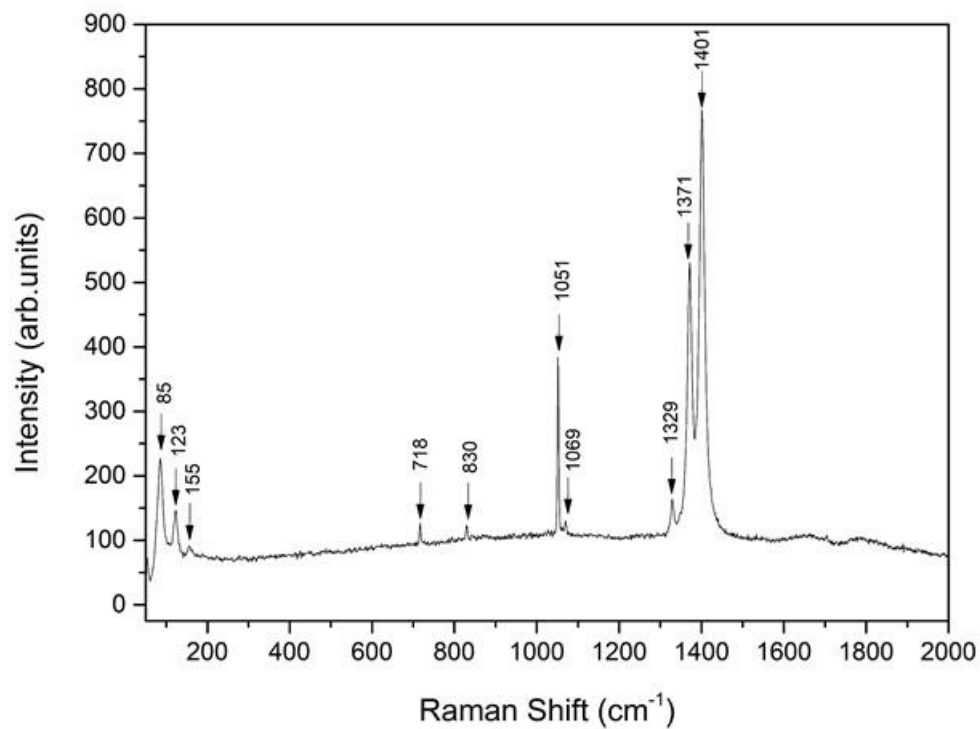


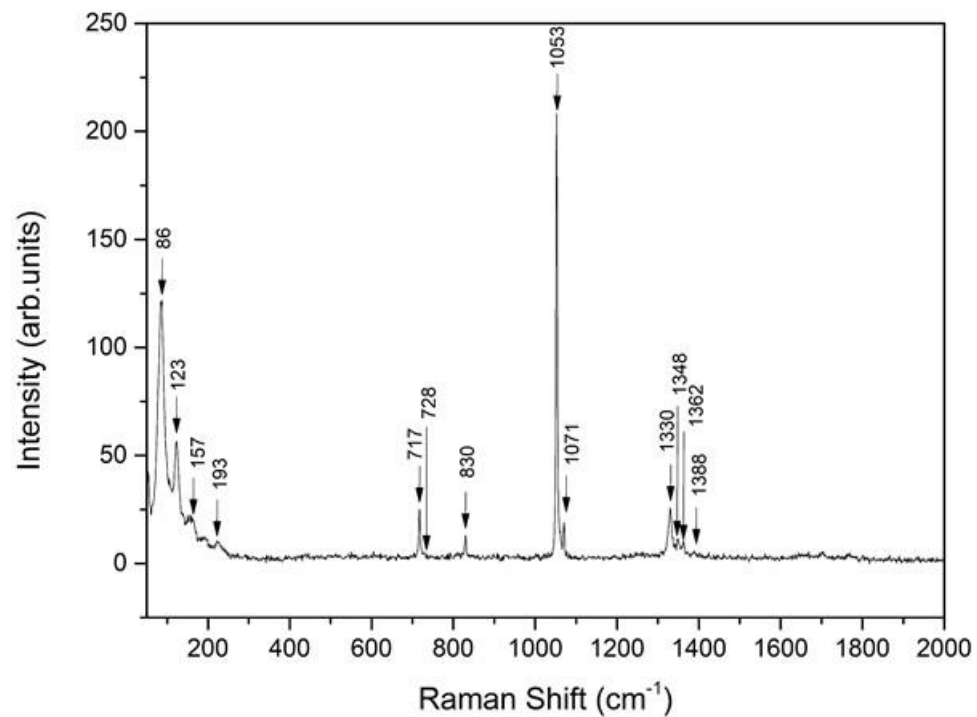
Figure 43. Raman spectra of pure Hitec.

Table 18. Raman band shifting for pure NaNO_3 , NaNO_2 , and KNO_3 , components of Hitec [97].

Pure Salt	Raman band shifting (cm^{-1})											
	K	K	Na	Na	NO_2	NO_2	NO_2	NO_3	NO_3	NO_3	K	K
NaNO_3	-	-	105	198	-	-	-	733	1070	1398	-	-
KNO_3	83	125	-	-	-	-	-	720	1053		1345	1360
NaNO_2	-	-	136	160	840	1237	1335	-	-	-	-	-



a.



b.

Figure 44. Raman spectra of the MSBNF with 1.5 wt.% of Al₂O₃, a. showing the presence of nanoparticles and b. MSBNF without the presence of nanoparticles.

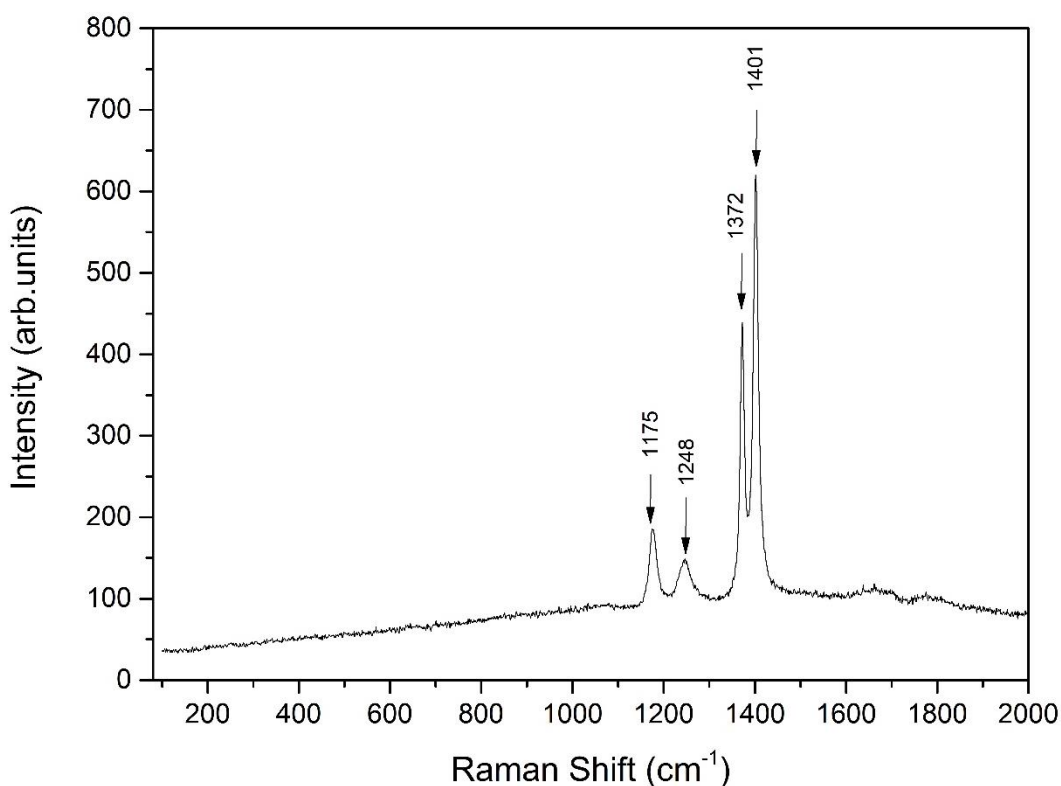


Figure 45. Raman spectra of pristine alumina nanoparticles.

During the corrosive behavior test aliquots at 24, 48, 76, 97, 336, 432, 500, 668, 720, 864, 1663, 1932, and 2000 h were sampled from the reactors with Hitec and MSBNF with 1.5 wt.% of Al_2O_3 as fluids. **Figure 46** and **Table 19** show the stability evaluation by Raman measurements of the aliquots during the corrosive behavior test with highlighted Raman bands for Hitec. In the same way, **Figure 47** and **Table 20** present the stability evaluation by Raman measurements and respective Raman bands for the nanofluid. According to the results, no significant changes were found through time in the characteristic $\text{NO}_3\text{-NO}_2$ bands, that is around 150, 826 and 1327 cm^{-1} , although in some cases the intensities of the bands were not high at the end of the test, that is, at 2000 h the three bands were still present in the spectra. This behavior can be related to the constant nitrogen atmosphere throughout the test. Some authors have reported that by keeping a nitrogen atmosphere, it is possible to increase the stability of the salt; due to the nitrogen atmosphere, the partial pressure of nitrogen can be fixed, avoiding the production of oxides and the decomposition of nitrite to nitrate.[49], [128]. It is important to highlight that the different cations alter the electrical environment of the polyatomic anions affecting their vibrational frequencies, for this reason, the bands are not always in the same

positions [162]. Taking into account the Raman results, the stability over time of the Hitec salt and, even more important, the nanofluid was demonstrated. Using this technique, it was not possible to observe corrosion products in the aliquots of the salt or the nanofluid.

Table 19. Raman bands of Hitec during corrosive behavior test.

Time\ Raman band shifting (cm-1)	Na	K	NO₂	Na	NO₃	NO₃	NO₂	NO₃	NO₃	NO₂	K	K	NO₃
0	83	119	150	187	713	722	826	1049	1067	1327	1344	1360	1386
24	86	122	155	189	717	729	830	1052	1071	1330	1347	1364	1389
48	86	123	158	189	719	730	832	1054	1072	1329	1347	1363	1387
72	86	123	156	187	717	727	831	1052	1071	1330	1348	1362	1391
96	87	123	162	187	717	727	830	1052	1071	1331	1348	1362	1388
336	85	121	154	187	715	724	828	1050	1067	1328	1347	1360	1389
432	84	120	160	186	714	723	826	1049	1067	1326	1345	1360	1387
500	84	121	155	188	716	728	828	1050	1069	1329	1347	1361	1388
668	87	124	157	187	718	727	831	1054	1072	1331	1350	1364	1392
720	87	124	156	190	718	728	831	1054	1072	1331	1348	1365	1392
864	83	121	155	187	714	724	827	1049	1062	1327	1344	1361	1387
1668	83	119	154	186	715	725	827	1049	1067	1327	1347	1360	1388
1932	84	121	155	187	715	725	828	1050	1068	1327	1347	1361	1387
2000	85	121	154	187	715	730	827	1050	1068	1327	1347	1360	1387

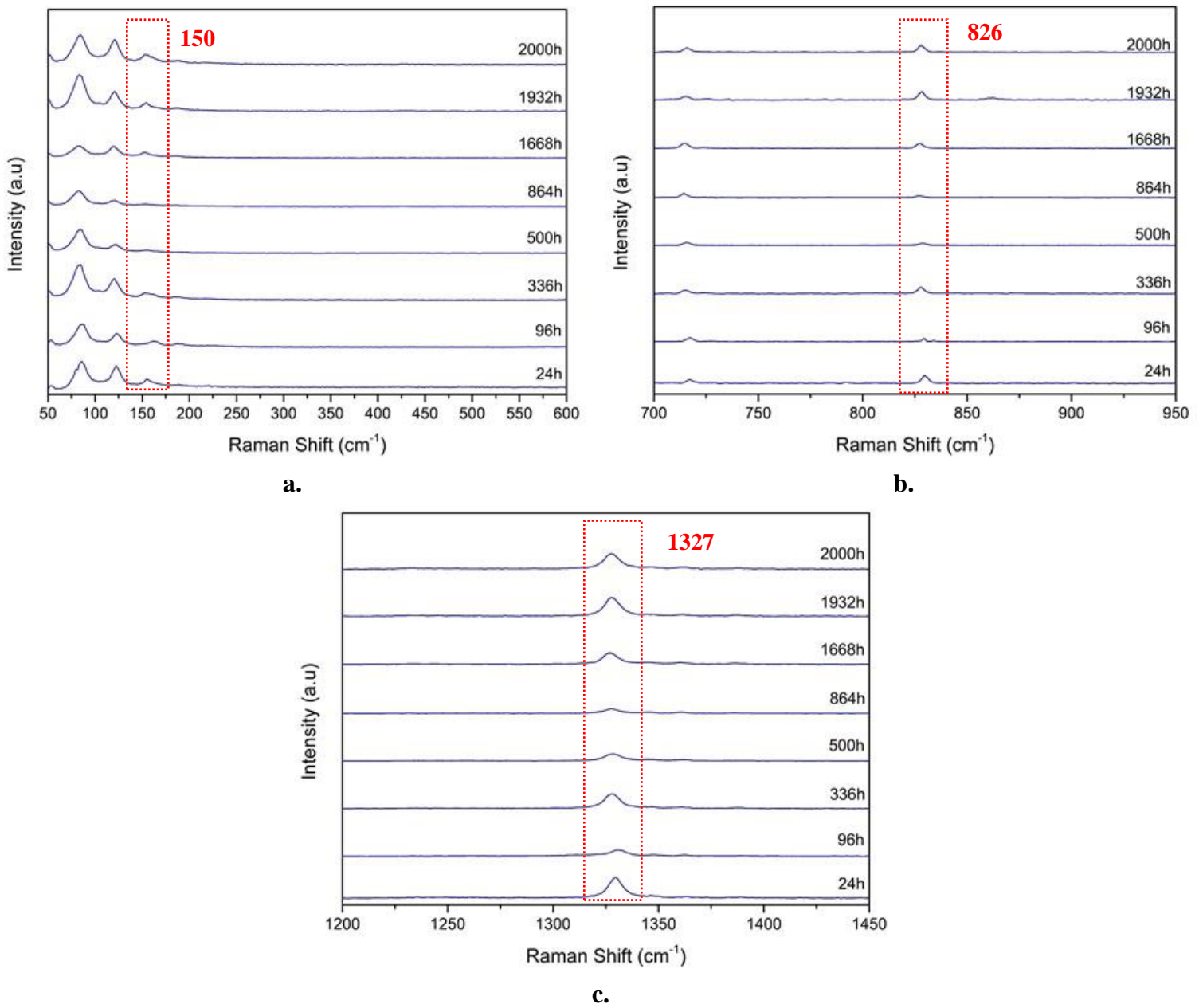
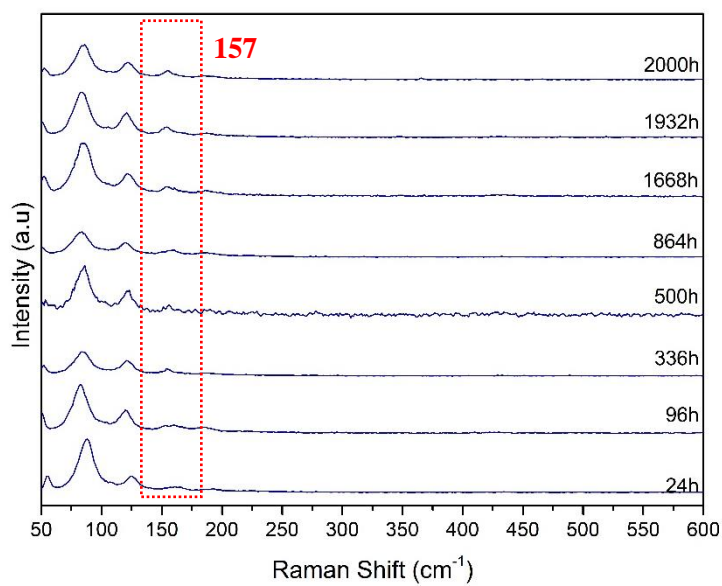


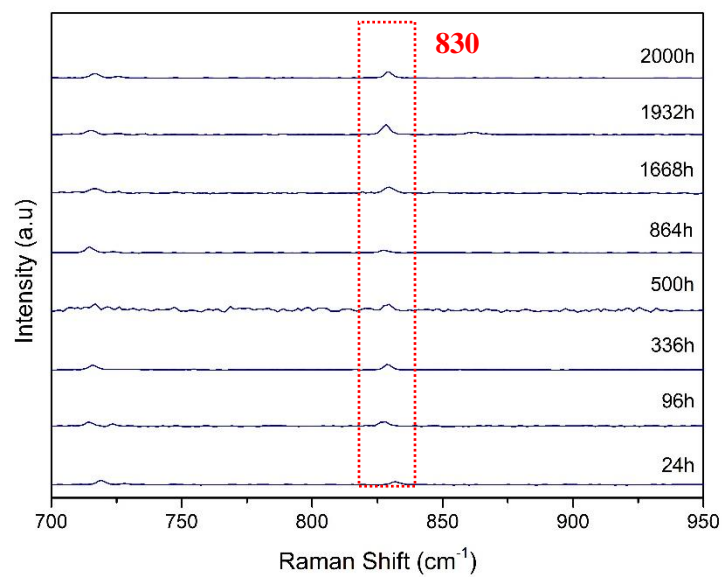
Figure 46. Evaluation of the chemical stability by Raman during the corrosive behavior test of the Hitec.

Table 20. Raman bands of Hitec with 1.5 wt.% of Al₂O₃ during corrosive behavior test.

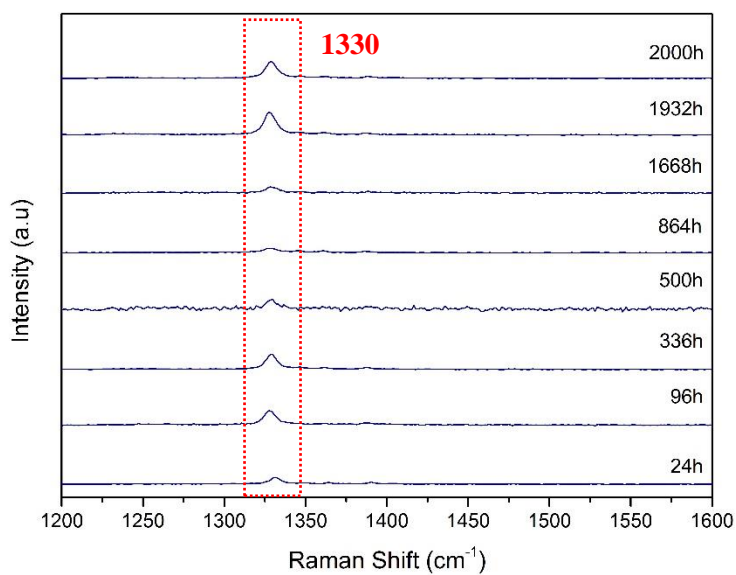
Time\ Raman band shifting (cm-1)	Na	K	NO₂	Na	NO₃	NO₃	NO₂	NO₃	NO₃	NO₂	K	K	NO₃
0	86	123	157	193	717	728	830	1053	1071	1330	1348	1362	1388
24	88	125	157	192	719	728	832	1054	1072	1331	1346	1364	1391
48	86	122	156	187	717	726	830	1052	1069	1330	1348	1362	1389
72	85	122	155	185	717	727	830	1052	1071	1330	1348	1362	1388
96	83	120	160	186	715	724	827	1049	1067	1327	-	1361	1386
336	84	121	155	186	716	724	828	1051	1069	1328	1347	1361	1388
432	83	121	154	186	715	725	827	1050	1068	1327	1348	1360	1386
500	86	123	157	187	717	728	830	1053	1071	1330	1348	1362	1388
668	87	123	157	186	718	727	831	1053	1071	1330	1341	1361	1388
720	88	123	157	187	718	725	831	1054	1072	1331	1347	1361	1390
864	84	120	160	187	715	724	827	1051	1067	1330	1347	1361	1386
1668	86	121	154	186	717	726	830	1051	1069	1329	-	-	1388
1932	84	121	155	187	715	725	828	1050	1068	1327	1348	1361	1387
2000	86	122	155	185	717	726	830	1051	1069	1329	1345	1361	1388



a.



b.

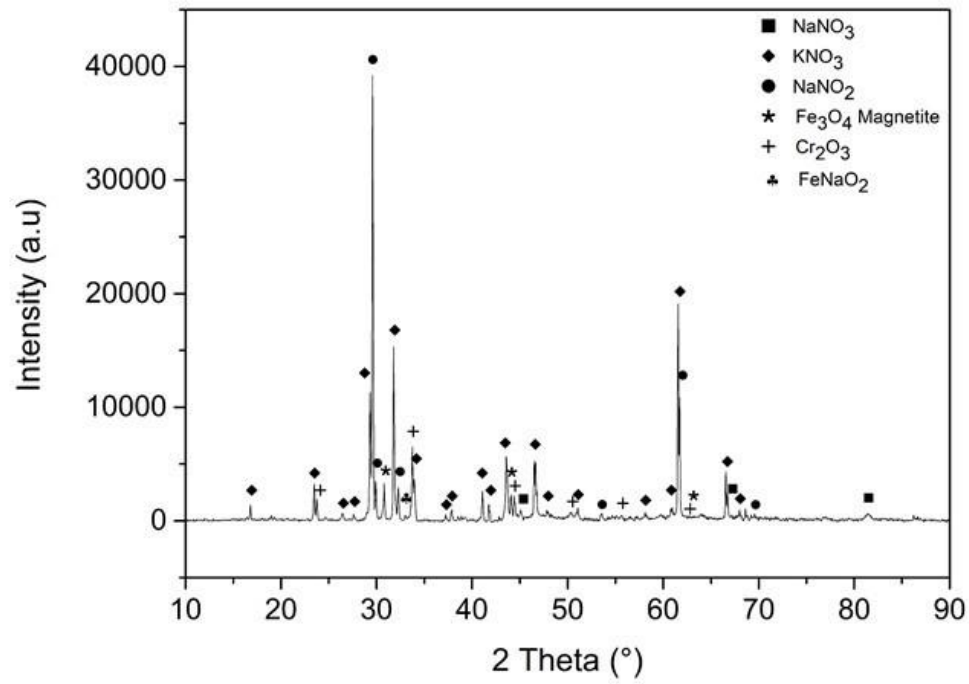


c.

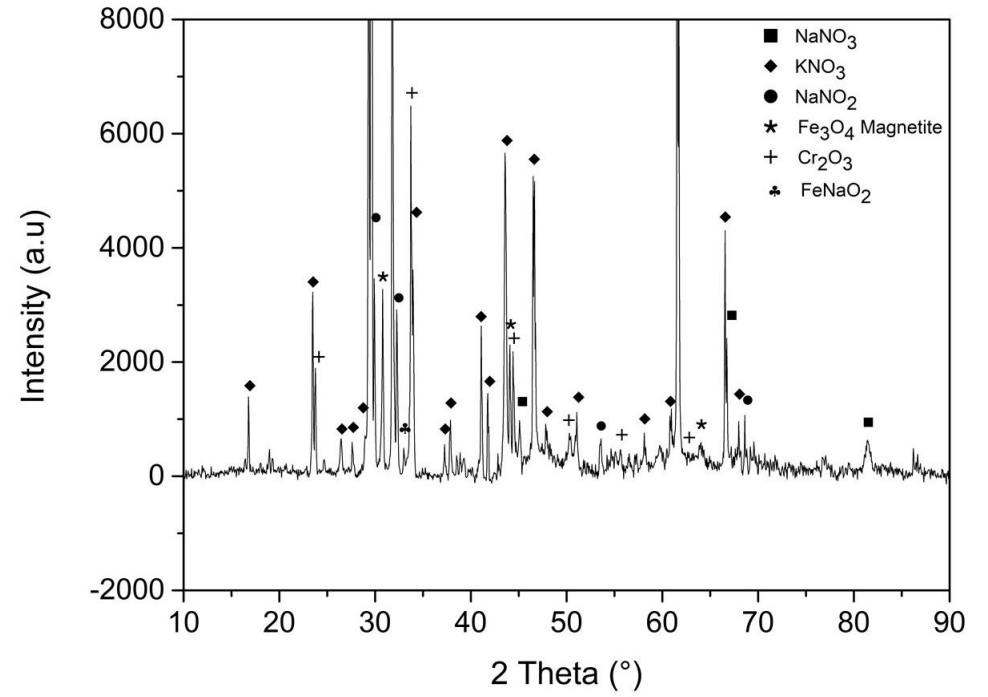
Figure 47. Evaluation of the chemical stability by Raman during the corrosive behavior test of the MSBNF with 1.5 wt.% of Al_2O_3 .

5.6.4 XRD

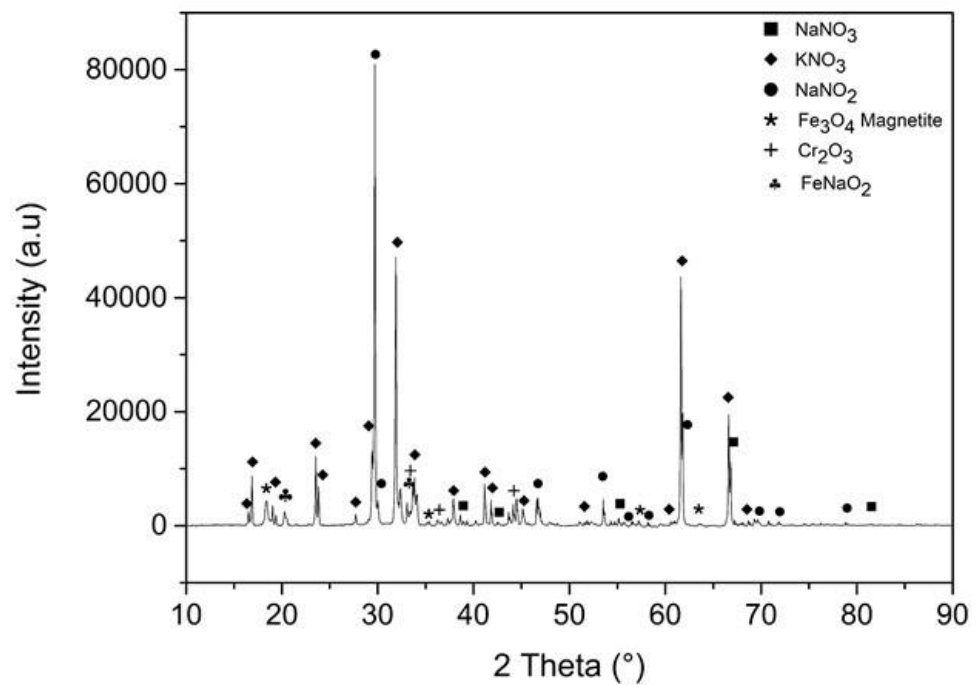
Figure 48 shows the XRD patterns obtained for the aliquots of Hitec and MSBNF from the reactors after 2000 h of the corrosive behavior test, as well as the close view for better identification of all the peaks. In the results for both samples, the components of the molten salt were found, that is, NaNO_3 , KNO_3 , and NaNO_2 . Despite the good behavior of both the Hitec salt and the nanofluid against corrosion, the presence of corrosion products such as Magnetite, Cr_2O_3 , and FeNaO_2 were evidenced. These products may be the cause of the decrease in the thermal properties of the salt, as has been reported by other authors [101], [103]



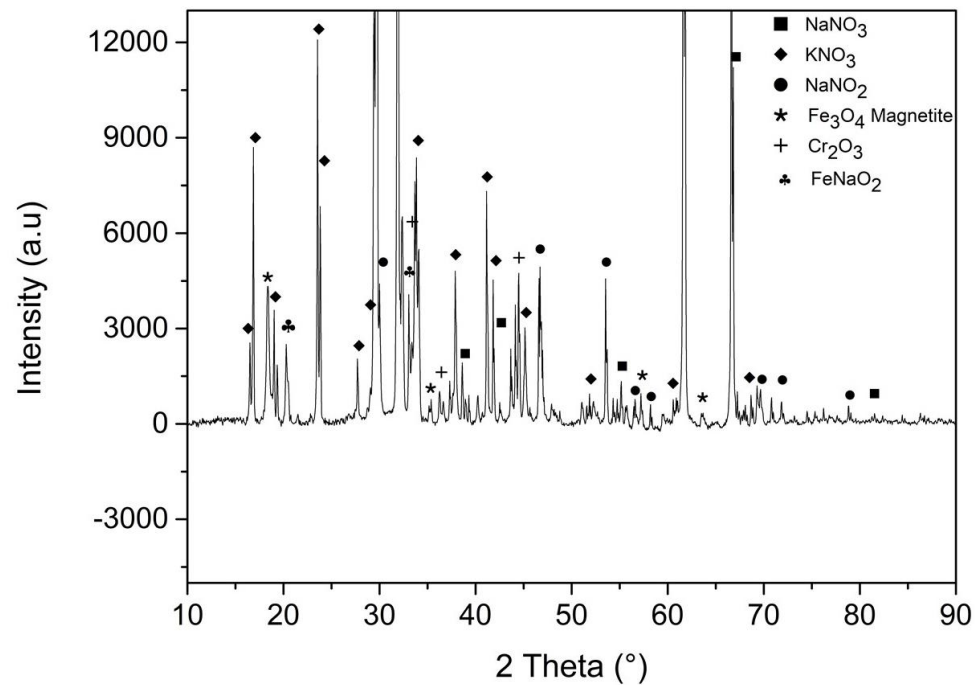
a.



b.



c.



d.

Figure 48. The XRD pattern of the aliquot of **a.** Hitec and **b.** close view of Hitec, **c.** MSBNF, and **d.** close view of MSBNF, after 2000 h at 550°C.

5.7 Conclusion

In order to establish the chemical stability and presence of corrosion products in the Hitec and the MSBNF after the corrosive behavior test, melting point measurements, SEM micrograph, Raman, and XRD were performed. Although both Hitec and the MSBNF showed good corrosion behavior, the presence of the main corrosion products within the salt and the nanofluid was evidenced after the evaluation of the aggressiveness during 2000 h subjected to cycling between 550 and 160°C at each sample withdrawal. However, good chemical stability was determined by Raman in all samples throughout the corrosion test. Both the Hitec salt and the nanofluid showed the characteristic bands of the Nitrite ion, indicating that the sample did not degrade.

6. SUMMARY

6.1 Summary

Considering the need to improve the thermal properties of molten salts used as a storage medium in thermal energy storage systems (TES) of CSP plants, with the aim to decrease LCOE and improve the competitiveness of this technology compared to traditional from fossil sources; the use of solid particles was implemented and showed a significant improvement in the thermal properties of salts, specifically for specific heat capacity and thermal conductivity. Hence, and in order to contribute to the understanding of the salt-nanoparticle system, molten salt-based nanofluids were synthesized with Hitec as base salt and alumina nanoparticles using two different methods: *i.* a traditional two-step method that uses water during the process for the distribution and homogenization of the system, and *ii.* a two-step modified method by replacing water with butanol in order to reduce costs and production time, without having a great influence on the dispersion and homogenization of the nanofluid.

The thermal properties, specific heat capacity, melting point, and stability temperature were evaluated, showing the potential of the proposed new two-step method with an increase of up to 14.08% in the specific heat capacity, 4.21% in the melting point without significantly affecting the stability with only 1.5 wt.% of Al₂O₃ nanoparticles. On the other hand, with the same proportion (1.5 wt.%) an increase of up to 18.74% in the specific heat was achieved by the traditional two-step method, reducing the melting point by 4.08%, without modification of stability. It should be noted that all the samples evaluated showed an improvement in the thermal properties compared to the base salt.

The presence of the nanoparticles after the thermal evaluation was evidence in the samples synthesized with both methods. However, the interconnecting network of nanoparticles or needle-like structure reported for some authors were not found in this investigation. Therefore, this is not the reason why there was a significant increase in Cp. The proposed mechanisms to explain the significant increment of Cp in MSBNFs are: *i.* higher specific heat capacity of nanoparticles than the bulk, *ii.* the abnormal increase in thermal resistance between nanoparticles and surrounding liquid molecules and *iii.* the layering of liquid molecules at the surface to form a semi-solid layer, and the possible recent mechanism of the functionalization of nanoparticles by ion-exchange mechanism.

Experimentally, in this thesis, it was not possible to demonstrate that the increase in the C_p of the nanofluid occurred by only one of these mechanisms.

In addition to the influence of the high surface area of the nanoparticles per unit volume and the good dispersion of the smallest particles in the salt, the increase in C_p may be due to the formation of a new phase, a white foam also observed in this work, which some authors have shown has an effect both on the ionic interaction of the fluid with the nanoparticles, and on the generation of a second Kapitza resistance. On the other hand, taking into account other studies, it could be indicated that the ion exchange capacity would be favored thanks to the presence of the potassium ion within the salt. The mixture of all these factors and the additional ones that must be tested experimentally for this particular system, in which there is the presence of three different salts, can lead to obtaining additional storage and therefore to an increase in the C_p of the nanofluid.

Considering the application to which the materials synthesized in this research are directed, that is, as a storage medium in the TES systems of CSP plants, the storage capacity, cost of the material is of utmost importance. In this way, the storage capacity was calculated according to the evaluated thermal properties, obtaining an increase of up to 20% with 1.0 wt.% of nanoparticles obtained by the traditional method, while 19% was reached with 1.5 wt.% of nanoparticles synthesized by the new proposed method. Although the cost per Kg and the cost of storage decreased in the same proportion for the two synthesis methods evaluated, it should be noted that in the calculation of these values it does not take into account some factors within the process such as the use of water and the energy for its complete removal, as well as the time required for this, generating an additional cost for the traditional method compared to the method proposed in this research. Thanks to the improvement in storage capacity after the addition of alumina nanoparticles, the size of thermal energy storage tanks could be reduced and subsequently also the costs of the CSP technology.

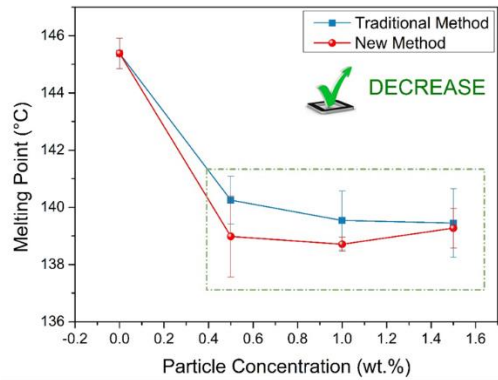
The results of the evaluation of the aggressiveness during 2000 h at 550 °C under a controlled nitrogen atmosphere and constant mechanical agitation, showed a better behavior to corrosion by the nanofluid with 1.5wt% of alumina nanoparticles compared to pure Hitec. This behavior may be related to the embedding of the nanoparticles in the oxide layer, allowing the formation of a more compact corrosion layer, as well as the possible influence of nanoparticles on the formation of a compact layer of compound spinel $FeCr_2O_4$, which was shown to be more protective in this case. There is no indication of any attack through the grain boundaries, and therefore intergranular corrosion was not observed, evidencing uniform internal oxidation. There was not significant pitting in any of the

samples evaluated, neither exposed to Hitec nor in the nanofluid. The salt and nanofluid used for the evaluation of aggressiveness were characterized after the test, the presence of corrosion products causing changes in the thermal properties of the salt was evident, particularly the melting point. However, there was no evidence of a decrease in the chemical stability of both the salt and the nanofluid after remaining for 2000h at 550°C, this behavior is related to the controlled atmosphere of nitrogen during the process, avoiding the $\text{NO}_2/\text{NO}_3^-$ conversion. **Figure 49** shows a summary of the main properties evaluated in this research.

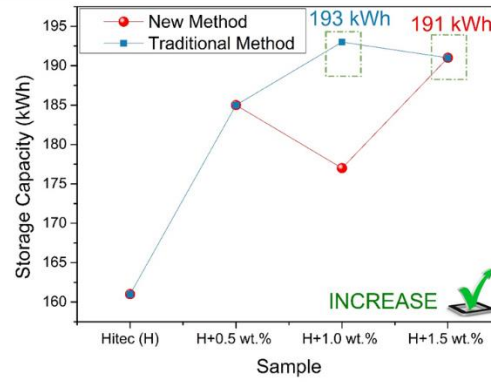
MOLTEN SALT-BASED NANOFUIDS

TRADITIONAL METHOD VS. NEW METHOD

1. THERMOPHYSICAL PROPERTIES



2. STORAGE CAPACITY AND COST



HITEC VS. MSBNF (1.5 wt% Al₂O₃)

3. AGGRESSIVE BEHAVIOR

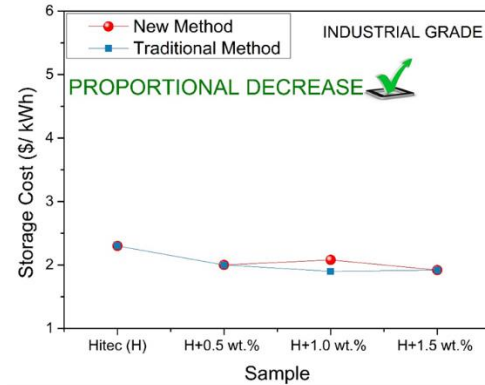
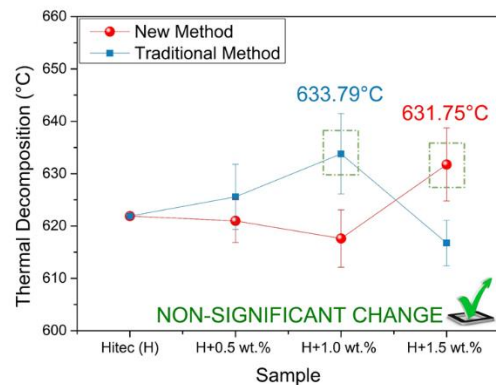
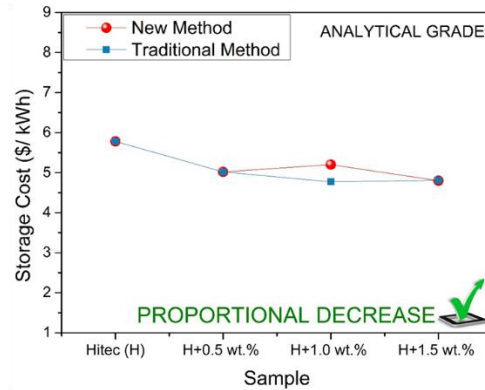
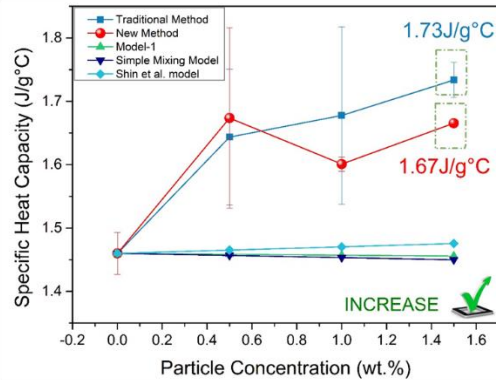
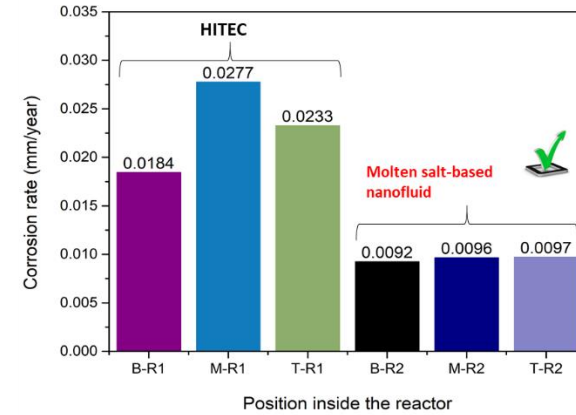


Figure 49. Summary scheme with the main properties evaluated in this research.

6.2 Main Achievements

6.3 List of Products

During this research the following papers, conference, and equipment were developed:

Papers:

- ✓ **Recent Developments in Phase Change Materials for Energy Storage Applications: A Review**
H. Nazir, M. Batool, F.J. Bolivar Osorio, M. Isaza-Ruiz, X. Xu, K. Vignarooban, P. Phelan, Inamuddin, A.M. Kannan*.
International Journal of Heat and Mass Transfer. 129 (2019) 491–523.
- ✓ **Viscosity and Stability Analysis of Hitec Salt-Based Alumina Nanofluids**
Marllory Isaza-Ruiz, Rosa Mondragón, Francisco Bolivar Osorio, Jorge Ventura, Leonor Hernández*.
Solar Energy Materials & Solar Cells 222 (2021) 110923.
- ✓ **Thermal Properties of Hitec Salt-Based Nanofluids Synthesized by New Two-Step Method**
Marllory Isaza-Ruiz*, Francisco Bolivar Osorio.
Procedia Environmental Science, Engineering and Management 8 (2021) (1) 147-155.
- ✓ **Development of a New Method of Synthesis of Hitec Salt-Based Alumina Nanofluids.**
Marllory Isaza-Ruiz*, Francisco Bolivar Osorio.
Ingeniería e Investigación (2021), **Submitted**.
- ✓ **Corrosion Behavior of Stainless Steel in Contact with Hitec Salt-Based Alumina Nanofluids for CSP applications**
Marllory Isaza-Ruiz*, Juan Guillermo Castaño, Francisco Bolivar Osorio.
(2021), **In preparation**.

- ✓ **Corrosion Behavior of Stainless Steel in Contact with Molten Hitec Salt for CSP applications.**

Marllory Isaza-Ruiz^{*}, Juan Guillermo Castaño, Francisco Bolivar Osorio.
(2021), **In preparation.**

Chapter in the Book:

- ✓ **Nanofluidos: La nueva generación de fluidos**

Marllory Isaza Ruiz

(2020) Fondo Editorial ITM, **Submitted**

Conference:

- ✓ **Determination of Specific Heat of Molten Salt-Based Nanofluids Using Modulated and Standard Differential Scanning Calorimetry: A Comparative Study**

Marllory Isaza-Ruiz , Francisco Bolivar Osorio

Oral presentation in Eurotherm Seminar #112 Advances in Thermal Energy Storage. May 15-17, 2019. Lleida-Spain

- ✓ **Thermal Properties of Hitec Salt-Based Nanofluids Synthesized by New Two-Step Method**

Marllory Isaza-Ruiz , Francisco Bolivar Osorio

Environmental Innovations II: Advances in Engineering, Technology, and Management. September 21-25, 2020. Online Conference. **Submitted.**

Equipment:

- ✓ **Corrosive behavior test reactors**

This research was carried out the design and manufacture of two reactors with a capacity of 1000 ml of sample with a controlled atmosphere, temperature, and mechanical agitation to evaluate the corrosive behavior of molten salt in under real conditions.

6.4 Future Directions

After the completion of this Ph.D. project and in order to have a better understanding of the system, the following aspects could be considered for future research.

1. According to the results presented in this research, the viability of the application of the new method to synthesize the molten salt-based nanofluids was shown. However, given the scope of this project, it was not possible to assess its aggressiveness against any steel commonly used for the manufacture of storage tanks for CSP plants. Therefore, in a future project, the corrosive behavior of nanofluids obtained using this method could be evaluated.
2. Similarly, the study of other atmospheres and other metals could allow selecting the best conditions for the use of these nanofluids made by both the traditional method and the new method proposed for use as a storage medium in CSP plants.
3. The examination in terms of salt composition and kinetics are required to have a comprehensive understanding of the system.

References

- [1] REN21 Renewables Now, *Renewables 2019 global status report 2019*. 2019.
- [2] C. Richter, S. Teske, and R. Short, “Concentrating Solar Power - Global Outlook 09,” pp. 1–88, 2009.
- [3] U. Pelay, L. Luo, Y. Fan, D. Stitou, and M. Rood, “Thermal energy storage systems for concentrated solar power plants,” *Renewable and Sustainable Energy Reviews*, vol. 79, no. March, pp. 82–100, 2017.
- [4] A. Gil *et al.*, “State of the art on high temperature thermal energy storage for power generation. Part 1—Concepts, materials and modellization,” *Renewable and Sustainable Energy Reviews*, vol. 14, no. 1, pp. 31–55, Jan. 2010.
- [5] M. Liu *et al.*, “Review on concentrating solar power plants and new developments in high temperature thermal energy storage technologies,” *Renewable and Sustainable Energy Reviews*, vol. 53, pp. 1411–1432, 2016.
- [6] S. Kuravi, J. Trahan, D. Y. Goswami, M. M. Rahman, and E. K. Stefanakos, “Thermal energy storage technologies and systems for concentrating solar power plants,” *Progress in Energy and Combustion Science*, vol. 39, no. 4, pp. 285–319, Aug. 2013.
- [7] M. T. Islam, N. Huda, A. B. Abdullah, and R. Saidur, “A comprehensive review of state-of-the-art concentrating solar power (CSP) technologies: Current status and research trends,” *Renewable and Sustainable Energy Reviews*, vol. 91, no. November 2017, pp. 987–1018, 2018.
- [8] R. Serrano-López, J. Fradera, and S. Cuesta-López, “Molten salts database for energy applications,” *Chemical Engineering and Processing*, vol. 73, pp. 87–102, 2013.
- [9] D. Shin, “MOLTEN SALT NANOMATERIALS FOR THERMAL ENERGY STORAGE AND CONCENTRATED SOLAR POWER APPLICATIONS,” 2011.
- [10] L. A. Weinstein, J. Loomis, B. Bhatia, D. M. Bierman, E. N. Wang, and G. Chen, “Concentrating Solar Power,” *Chemical Reviews*, vol. 115, no. 23, pp. 12797–12838, 2015.
- [11] D. A. Baharoon, H. A. Rahman, W. Z. W. Omar, and S. O. Fadhl, “Historical development

- of concentrating solar power technologies to generate clean electricity efficiently – A review,” *Renewable and Sustainable Energy Reviews*, vol. 41, pp. 996–1027, 2015.
- [12] X. Xu, K. Vignarooban, B. Xu, K. Hsu, and A. M. Kannan, “Prospects and problems of concentrating solar power technologies for power generation in the desert regions,” *Renewable and Sustainable Energy Reviews*, vol. 53, pp. 1106–1131, 2016.
- [13] IRENA Statistics, *Renewable Energy Capacity Statistics 2019*. 2019.
- [14] International Renewable Energy Agency (IRENA), *IRENA (2018), Renewable capacity statistics 2018*. 2018.
- [15] S. P. and S. Greenpeace International, “Concentrating Solar Power Global Outlook 09,” *Power*, p. 88, 2009.
- [16] T. E. Boukelia, M. S. Mecibah, B. N. Kumar, and K. S. Reddy, “Investigation of solar parabolic trough power plants with and without integrated TES (thermal energy storage) and FBS (fuel backup system) using thermic oil and solar salt.,” *Energy*, vol. 88, pp. 292–303, Aug. 2015.
- [17] Q. Liu, Y. Wang, Z. Gao, J. Sui, H. Jin, and H. Li, “Experimental investigation on a parabolic trough solar collector for thermal power generation,” *Science China Technological Sciences*, vol. 53, no. 1, pp. 52–56, 2010.
- [18] A. Messadi and Y. Timoumi, “Thermal Study of a Parabolic Trough Collector,” in *Design and Modeling of Mechanical Systems - II*, 2015, pp. 811–821.
- [19] IRENA, “Renewable Energy Technologies: Cost Analysis Series,” *Comprehensive Renewable Energy*, vol. 3, no. 2, pp. 595–636, 2012.
- [20] O. Achkari and A. El Fadar, “Latest developments on TES and CSP technologies – Energy and environmental issues, applications and research trends,” *Applied Thermal Engineering*, vol. 167, no. August 2019, 2020.
- [21] J. Cot-Gores, A. Castell, and L. F. Cabeza, “Thermochemical energy storage and conversion: A-state-of-the-art review of the experimental research under practical conditions,” *Renewable and Sustainable Energy Reviews*, vol. 16, no. 7, pp. 5207–5224, 2012.

- [22] M. Aneke and M. Wang, "Energy storage technologies and real life applications – A state of the art review," *Applied Energy*, vol. 179, pp. 350–377, 2016.
- [23] R. W. Bradshaw, J. G. Cordaro, and N. P. Siegel, "MOLTEN NITRATE SALT DEVELOPMENT FOR THERMAL ENERGY STORAGE IN PARABOLIC TROUGH SOLAR POWER SYSTEMS," 2009.
- [24] C. Villada, F. Jaramillo, J. G. Castaño, F. Echeverría, and F. Bolívar, "Design and development of nitrate-nitrite based molten salts for concentrating solar power applications," *Solar Energy*, vol. 188, no. May, pp. 291–299, 2019.
- [25] T. Wang, D. Mantha, and R. G. Reddy, "Novel low melting point quaternary eutectic system for solar thermal energy storage," *Applied Energy*, vol. 102, pp. 1422–1429, 2013.
- [26] A. G. Fernández, S. Ushak, H. Galleguillos, and F. J. Pérez, "Development of new molten salts with LiNO_3 and $\text{Ca}(\text{NO}_3)_2$ for energy storage in CSP plants," *Applied Energy*, vol. 119, no. 3, pp. 131–140, 2014.
- [27] H. Nazir *et al.*, "Recent developments in phase change materials for energy storage applications: A review," *International Journal of Heat and Mass Transfer*, vol. 129, pp. 491–523, 2019.
- [28] Z. Jiang *et al.*, "Form-stable LiNO_3 – NaNO_3 – KNO_3 – $\text{Ca}(\text{NO}_3)_2$ /calcium silicate composite phase change material (PCM) for mid-low temperature thermal energy storage," *Energy Conversion and Management*, vol. 106, no. 3, pp. 165–172, 2015.
- [29] S. Jegadheeswaran and S. D. Pohekar, "Performance enhancement in latent heat thermal storage system: A review," *Renewable and Sustainable Energy Reviews*, vol. 13, no. 9, pp. 2225–2244, 2009.
- [30] M. Liu, J. C. Gomez, C. S. Turchi, N. H. S. Tay, W. Saman, and F. Bruno, "Determination of thermo-physical properties and stability testing of high-temperature phase-change materials for CSP applications," *Solar Energy Materials and Solar Cells*, vol. 139, pp. 81–87, 2015.
- [31] K. Nithyanandam and R. Pitchumani, "Optimization of an encapsulated phase change material thermal energy storage system," *Solar Energy*, vol. 107, pp. 770–788, Sep. 2014.
- [32] K. Pielichowska and K. Pielichowski, "Phase change materials for thermal energy storage,"

- Progress in Materials Science*, vol. 65, pp. 67–123, Aug. 2014.
- [33] C. Y. Zhao, W. Lu, and Y. Tian, “Heat transfer enhancement for thermal energy storage using metal foams embedded within phase change materials (PCMs),” *Solar Energy*, vol. 84, no. 8, pp. 1402–1412, 2010.
- [34] H. Zhang, J. Baeyens, G. Cáceres, J. Degève, and Y. Lv, “Thermal energy storage: Recent developments and practical aspects,” *Progress in Energy and Combustion Science*, vol. 53, pp. 1–40, 2016.
- [35] K. Niedermeier, J. Flesch, L. Marocco, and T. Wetzel, “Assessment of thermal energy storage options in a sodium-based CSP plant,” *Applied Thermal Engineering*, vol. 107, pp. 386–397, 2016.
- [36] D. Salas, E. Tapachès, N. Mazet, and D. Aussel, “Economical optimization of thermochemical storage in concentrated solar power plants via pre-scenarios,” *Energy Conversion and Management*, vol. 174, no. April, pp. 932–954, 2018.
- [37] B. Ma, “Experimental and Numerical Investigation of Molten Salt Nanomaterials for Enhanced Thermal Energy Storage (TES) and Heat Transfer Fluid (HTF),” 2017.
- [38] C. Parrado, A. Marzo, E. Fuentealba, and A. G. Fernández, “2050 LCOE improvement using new molten salts for thermal energy storage in CSP plants,” *Renewable and Sustainable Energy Reviews*, vol. 57, pp. 505–514, 2016.
- [39] D. Kearney *et al.*, “Assessment of a Molten Salt Heat Transfer Fluid in a Parabolic Trough Solar Field,” *Jsee*, vol. 125, no. April 2002, pp. 1–20, 2002.
- [40] K. Vignarooban, X. Xu, A. Arvay, K. Hsu, and A. M. Kannan, “Heat transfer fluids for concentrating solar power systems - A review,” *Applied Energy*, vol. 146, pp. 383–396, 2015.
- [41] A. Bonk, S. Sau, N. Uranga, M. Hernaiz, and T. Bauer, “Advanced heat transfer fluids for direct molten salt line-focusing CSP plants,” *Progress in Energy and Combustion Science*, vol. 67, pp. 1339–1351, 2018.
- [42] H. Benoit, L. Spreafico, D. Gauthier, and G. Flamant, “Review of heat transfer fluids in tube-receivers used in concentrating solar thermal systems: Properties and heat transfer

- coefficients,” *Renewable and Sustainable Energy Reviews*, vol. 55, pp. 298–315, 2016.
- [43] A. G. Fernández, H. Galleguillos, E. Fuentealba, and F. J. Pérez, “Thermal characterization of HITEC molten salt for energy storage in solar linear concentrated technology,” *Journal of Thermal Analysis and Calorimetry*, vol. 122, no. 1, pp. 3–9, 2015.
- [44] R. Tufeu, J. P. Petitet, L. Denielou, and B. Neindre, “Experimental determination of the thermal conductivity of molten pure salts and salt mixtures,” *International Journal of Thermophysics*, vol. 6, no. 4, pp. 315–330, 1985.
- [45] S. F. Ahmed, M. Khalid, W. Rashmi, A. Chan, and K. Shahbaz, “Recent progress in solar thermal energy storage using nanomaterials,” *Renewable and Sustainable Energy Reviews*, vol. 67, no. January, pp. 450–460, 2017.
- [46] K. Coscia, T. Elliott, S. Mohapatra, A. Oztekin, and S. Neti, “Binary and Ternary Nitrate Solar Heat Transfer Fluids,” *Journal of Solar Energy Engineering*, vol. 135, no. 2, p. 021011, 2013.
- [47] Coastal Chemical Co. LLC, “HITEC ® Heat Transfer Salt,” Houston TX, 2009.
- [48] D. Kearney *et al.*, “Assessment of a Molten Salt Heat Transfer Fluid in a Parabolic Trough Solar Field,” *Journal of Solar Energy Engineering*, vol. 125, no. 2, pp. 170–176, 2003.
- [49] C. Villada, A. Bonk, T. Bauer, and F. Bolívar, “High-temperature stability of nitrate/nitrite molten salt mixtures under different atmospheres,” *Applied Energy*, vol. 226, pp. 107–115, 2018.
- [50] M. X. Ho and C. Pan, “Optimal concentration of alumina nanoparticles in molten hitec salt to maximize its specific heat capacity,” *International Journal of Heat and Mass Transfer*, vol. 70, pp. 174–184, 2014.
- [51] M. X. Ho and C. Pan, “Experimental investigation of heat transfer performance of molten HITEC salt flow with alumina nanoparticles,” *International Journal of Heat and Mass Transfer*, vol. 107, pp. 1094–1103, 2016.
- [52] S. U. S. Choi and J. A. Eastman, “Enhancing thermal conductivity of fluids with nanoparticles,” *ASME International Mechanical Engineering Congress and Exposition*, vol. 66, no. March, pp. 99–105, 1995.

- [53] S. K. Das, S. U. S. Choi, W. Yu, and T. Pradeep, *Nanofluids: Science and Technology*. 2007.
- [54] W. N. With, O. Hanley, J. Buongiorno, T. Mckrell, C. Link, and H. O. Hanley, "Measurement and Model Correlation of Specific Heat Capacity of Water-Based Nanofluids With Silica, Alumina and Copper Oxide Nanoparticles," 2015.
- [55] S.-Q. Zhou and R. Ni, "Measurement of the specific heat capacity of water-based Al₂O₃ nanofluid," *Applied Physics Letters*, vol. 92, no. 9, p. 093123, 2008.
- [56] R. S. Vajjha and D. K. Das, "Specific Heat Measurement of Three Nanofluids and Development of New Correlations," *Journal of Heat Transfer*, vol. 131, no. 7, p. 071601, 2009.
- [57] P. K. Namburu, D. P. Kulkarni, A. Dandekar, and D. K. Das, "Experimental investigation of viscosity and specific heat of silicon dioxide nanofluids," *Micro & Nano Letters*, vol. 2, no. 4, pp. 67–71, 2007.
- [58] P. Andreu-Cabedo, R. Mondragon, L. Hernandez, R. Martinez-Cuenca, L. Cabedo, and J. E. Julia, "Increment of specific heat capacity of solar salt with SiO₂ nanoparticles.," *Nanoscale research letters*, vol. 9, no. 1, p. 582, 2014.
- [59] H. Tiznobaik and D. Shin, "Enhanced specific heat capacity of high-temperature molten salt-based nanofluids," *International Journal of Heat and Mass Transfer*, vol. 57, no. 2, pp. 542–548, 2013.
- [60] M. Chieruzzi, G. F. Cerritelli, A. Miliozzi, J. M. Kenny, and L. Torre, "Heat capacity of nanofluids for solar energy storage produced by dispersing oxide nanoparticles in nitrate salt mixture directly at high temperature," *Solar Energy Materials and Solar Cells*, vol. 167, no. December 2016, pp. 60–69, 2017.
- [61] Y. Hu, Y. He, Z. Zhang, and D. Wen, "Effect of Al₂O₃ nanoparticle dispersion on the specific heat capacity of a eutectic binary nitrate salt for solar power applications," *Energy Conversion and Management*, vol. 142, pp. 366–373, 2017.
- [62] M. Chieruzzi, G. F. Cerritelli, A. Miliozzi, and J. M. Kenny, "Effect of nanoparticles on heat capacity of nanofluids based on molten salts as PCM for thermal energy storage," *Nanoscale Research Letters*, vol. 8, no. 1, pp. 1–9, 2013.

- [63] D. Shin and D. Banerjee, "Enhancement of specific heat capacity of high-temperature silica-nanofluids synthesized in alkali chloride salt eutectics for solar thermal-energy storage applications," *International Journal of Heat and Mass Transfer*, vol. 54, no. 5–6, pp. 1064–1070, 2011.
- [64] H. Riazi, S. Mesgari, N. A. Ahmed, and R. A. Taylor, "The effect of nanoparticle morphology on the specific heat of nanosalts," *International Journal of Heat and Mass Transfer*, vol. 94, pp. 254–261, 2016.
- [65] M.-C. Lu and C.-H. Huang, "Specific heat capacity of molten salt-based alumina nanofluid.," *Nanoscale research letters*, vol. 8, no. 1, p. 292, 2013.
- [66] R. Devaradjane and D. Shin, "Nanoparticle Dispersions on Ternary Nitrate Salts for Heat Transfer Fluid Applications in Solar Thermal Power," *Journal of Heat Transfer*, vol. 138, no. 5, p. 051901, 2016.
- [67] L. Zhang, X. Chen, Y. Wu, Y. Lu, and C. Ma, "Effect of nanoparticle dispersion on enhancing the specific heat capacity of quaternary nitrate for solar thermal energy storage application," *Solar Energy Materials and Solar Cells*, vol. 157, pp. 808–813, 2016.
- [68] D. Shin and D. Banerjee, "Effects of silica nanoparticles on enhancing the specific heat capacity of carbonate salt eutectic (work in progress)," *International Journal of Structural Changes in Solids – Mechanics and Applications*, vol. 2, no. 2, pp. 25–31, 2010.
- [69] G. Qiao, M. Lasfargues, A. Alexiadis, and Y. Ding, "Simulation and experimental study of the specific heat capacity of molten salt based nanofluids," *Applied Thermal Engineering*, vol. 111, pp. 1517–1522, 2017.
- [70] D. Shin and D. Banerjee, "Specific heat of nanofluids synthesized by dispersing alumina nanoparticles in alkali salt eutectic," *International Journal of Heat and Mass Transfer*, vol. 74, pp. 210–214, 2014.
- [71] B. Dudda and D. Shin, "Effect of nanoparticle dispersion on specific heat capacity of a binary nitrate salt eutectic for concentrated solar power applications," *International Journal of Thermal Sciences*, vol. 69, pp. 37–42, 2013.
- [72] M. Chieruzzi, A. Miliozzi, T. Crescenzi, L. Torre, and J. M. Kenny, "A New Phase Change

- Material Based on Potassium Nitrate with Silica and Alumina Nanoparticles for Thermal Energy Storage,” *Nanoscale Res Lett*, vol. 10, no. 1, pp. 984–994, 2015.
- [73] D. Shin and D. Banerjee, “Enhanced Specific Heat of Silica Nanofluid,” *Journal of Heat Transfer*, vol. 133, no. 2, p. 024501, 2011.
- [74] J. Seo and D. Shin, “Size effect of nanoparticle on specific heat in a ternary nitrate (LiNO₃–NaNO₃–KNO₃) salt eutectic for thermal energy storage,” *Applied Thermal Engineering*, vol. 102, pp. 144–148, Jun. 2016.
- [75] M. X. Ho and C. Pan, “Experimental investigation of heat transfer performance of molten HITEC salt flow with alumina nanoparticles,” *International Journal of Heat and Mass Transfer*, vol. 107, pp. 1094–1103, 2017.
- [76] M. Schuller, Q. Shao, and T. Lalk, “Experimental investigation of the specific heat of a nitrate-alumina nanofluid for solar thermal energy storage systems,” *International Journal of Thermal Sciences*, vol. 91, pp. 142–145, 2015.
- [77] P. D. Myers, T. E. Alam, R. Kamal, D. Y. Goswami, and E. Stefanakos, “Nitrate salts doped with CuO nanoparticles for thermal energy storage with improved heat transfer,” *Applied Energy*, vol. 165, pp. 225–233, 2016.
- [78] A. Svobodova-Sedlackova, C. Barreneche, G. Alonso, A. I. Fernandez, and P. Gamallo, “Effect of nanoparticles in molten salts – MD simulations and experimental study,” *Renewable Energy*, vol. 152, pp. 208–216, 2020.
- [79] B. Jo and D. Banerjee, “Enhanced Specific Heat Capacity of Molten Salt-Based Carbon Nanotubes Nanomaterials,” *Journal of Heat Transfer*, vol. 137, no. 9, p. 091013, 2015.
- [80] H. Tiznobaik, D. Banerjee, and D. Shin, “Effect of formation of ‘long range’ secondary dendritic nanostructures in molten salt nanofluids on the values of specific heat capacity,” *International Journal of Heat and Mass Transfer*, vol. 91, pp. 342–346, 2015.
- [81] D. Jo, B.; Banerjee, “Enhanced specific heat capacity of molten salts using organic nanoparticles,” in *ASME 2011 International Mechanical Engineering Congress & Exposition*, 2011, no. 2011, pp. 1–8.
- [82] N. Navarrete, L. Hernández, A. Vela, and R. Mondragón, “Influence of the production

- method on the thermophysical properties of high temperature molten salt-based nanofluids,” *Journal of Molecular Liquids*, vol. 302, p. 112570, 2020.
- [83] B. Muñoz-Sánchez, J. Nieto-Maestre, G. Imbuluzqueta, I. Marañón, I. Iparraguirre-Torres, and A. García-Romero, “A precise method to measure the specific heat of solar salt-based nanofluids,” *Journal of Thermal Analysis and Calorimetry*, vol. 129, no. 2, pp. 905–914, 2017.
- [84] Q. Xie, Q. Zhu, and Y. Li, “Thermal Storage Properties of Molten Nitrate Salt-Based Nanofluids with Graphene Nanoplatelets.,” *Nanoscale research letters*, vol. 11, no. 1, p. 306, 2016.
- [85] B. Dudda and D. Shin, “Investigation of Molten Salt Nanomaterial as Thermal Energy Storage in Concentrated Solar Power,” in *Proceedings of the ASME 2012 International Mechanical Engineering Congress & Exposition*, 2012, pp. 1–6.
- [86] N. Navarrete, L. Hernández, A. Vela, and R. Mondragón, “Influence of the production method on the thermophysical properties of high temperature molten salt-based nanofluids,” *Journal of Molecular Liquids*, vol. 302, 2020.
- [87] Y. Hu, Y. He, Z. Zhang, and D. Wen, “Enhanced heat capacity of binary nitrate eutectic salt-silica nanofluid for solar energy storage,” *Solar Energy Materials and Solar Cells*, vol. 192, no. December 2018, pp. 94–102, 2019.
- [88] B. El Far, S. M. M. Rizvi, Y. Nayfeh, and D. Shin, “Study of viscosity and heat capacity characteristics of molten salt nanofluids for thermal energy storage,” *Solar Energy Materials and Solar Cells*, vol. 210, no. March, p. 110503, 2020.
- [89] U. Nithiyantham, L. González-Fernández, Y. Grosu, A. Zaki, J. M. Igartua, and A. Faik, “Shape effect of Al₂O₃ nanoparticles on the thermophysical properties and viscosity of molten salt nanofluids for TES application at CSP plants,” *Applied Thermal Engineering*, vol. 169, no. March 2019, 2020.
- [90] Y. Li *et al.*, “Experimental study on the effect of SiO₂ nanoparticle dispersion on the thermophysical properties of binary nitrate molten salt,” *Solar Energy*, vol. 183, no. December 2018, pp. 776–781, 2019.

- [91] H. Akoh, Y. Tsukasaki, S. Yatsuya, and A. Tasaki, "Magnetic Properties of Ferromagnetic Ultrafine Particles Prepared By Vacuum," vol. 45, 1978.
- [92] X. Chen, Y. ting Wu, L. di Zhang, X. Wang, and C. fang Ma, "Experimental study on the specific heat and stability of molten salt nanofluids prepared by high-temperature melting," *Solar Energy Materials and Solar Cells*, vol. 176, no. December 2017, pp. 42–48, 2018.
- [93] X. Chen, Y. ting Wu, L. di Zhang, X. Wang, and C. fang Ma, "Experimental study on the specific heat and stability of molten salt nanofluids prepared by high-temperature melting," *Solar Energy Materials and Solar Cells*, vol. 176, no. November 2018, pp. 42–48, 2018.
- [94] X. Chen, Y. ting Wu, L. di Zhang, X. Wang, and C. fang Ma, "Experimental study on thermophysical properties of molten salt nanofluids prepared by high-temperature melting," *Solar Energy Materials and Solar Cells*, vol. 191, no. December 2017, pp. 209–217, 2019.
- [95] R. Mondragón, J. E. Juliá, L. Cabedo, and N. Navarrete, "On the relationship between the specific heat enhancement of salt-based nanofluids and the ionic exchange capacity of nanoparticles," *Scientific Reports*, vol. 8, no. 1, pp. 1–12, 2018.
- [96] H. Tiznobaik and D. Shin, "Enhanced specific heat capacity of high-temperature molten salt-based nanofluids," *International Journal of Heat and Mass Transfer*, vol. 57, no. 2, pp. 542–548, 2013.
- [97] C. Villada, "Design and Development of Nitrate-Nitrite Based Molten Salts for Energy Storage Applications in CSP Plants," Universidad de Antioquia, 2018.
- [98] A. P. IYER, "THE EFFECT OF SILICA NANOPARTICLES ON CORROSION OF STEEL BY MOLTEN CARBONATE EUTECTICS," 2011.
- [99] M. Schuller *et al.*, "Molten Salt-Carbon Nanotube Thermal Energy Storage for Concentrating Solar Power Systems," 2012.
- [100] Y. Grosu, N. Udayashankar, O. Bondarchuk, L. González-Fernández, and A. Faik, "Unexpected effect of nanoparticles doping on the corrosivity of molten nitrate salt for thermal energy storage," *Solar Energy Materials and Solar Cells*, vol. 178, no. December 2017, pp. 91–97, 2018.
- [101] A. G. Fernández, B. Muñoz-Sánchez, J. Nieto-Maestre, and A. García-Romero, "High

- temperature corrosion behavior on molten nitrate salt-based nanofluids for CSP plants,” *Renewable Energy*, vol. 130, pp. 902–909, 2019.
- [102] U. Nithiyantham, Y. Grosu, L. González-Fernández, A. Zaki, J. M. Igartua, and A. Faik, “Corrosion aspects of molten nitrate salt-based nanofluids for thermal energy storage applications,” *Solar Energy*, vol. 189, no. July, p. 200025, 2019.
- [103] Á. G. Fernández and L. F. Cabeza, “Molten salt corrosion mechanisms of nitrate based thermal energy storage materials for concentrated solar power plants: A review,” *Solar Energy Materials and Solar Cells*, vol. 194, no. February, pp. 160–165, 2019.
- [104] I. B. Singh, “The influence of moisture on the oxidation rate of iron in NaNO_3 and KNO_3 melts,” *Corrosion Science*, vol. 37, no. 12, pp. 1981–1989, 1995.
- [105] B. Ma and D. Banerjee, “Experimental measurements of thermal conductivity of alumina nanofluid synthesized in salt melt,” *AIP Advances*, vol. 7, no. 11, 2017.
- [106] D. Shin and D. Banerjee, “Effects of silica nanoparticles on enhancing the specific heat capacity of carbonate salt eutectic (work in progress),” *INTERNATIONAL JOURNAL OF STRUCTURAL CHANGES IN SOLIDS – Mechanics and Applications*, vol. 2, no. 2, pp. 25–31, 2010.
- [107] Y. L. Botero, J. E. López-Rendón, D. Ramírez, D. M. Zapata, and F. Jaramillo, “From clay minerals to Al_2O_3 nanoparticles: Synthesis and colloidal stabilization for optoelectronic applications,” *Minerals*, vol. 10, no. 2, 2020.
- [108] American Society for Testing and Materials, “ASTM E1269 - Standard Test Method for Determining Specific Heat Capacity by Differential Scanning,” *ASTM Standards*, vol. i, pp. 1–6, 2011.
- [109] American Society for Testing and Materials, “E2716-09 Standard Test Method for Determining Specific Heat Capacity by Sinusoidal Modulated Temperature Differential Scanning Calorimetry,” *ASTM Standards*, vol. i, no. E2716-09, pp. 1–4, 2015.
- [110] M. Sarvghad, S. Delkasar Maher, D. Collard, M. Tassan, G. Will, and T. A. Steinberg, “Materials compatibility for the next generation of Concentrated Solar Power plants,” *Energy Storage Materials*, vol. 14, no. March, pp. 179–198, 2018.

- [111] F. Zaversky, J. García-Barberena, M. Sánchez, and D. Astrain, “Transient molten salt two-tank thermal storage modeling for CSP performance simulations,” *Solar Energy*, vol. 93, pp. 294–311, 2013.
- [112] C. Mayo, E. Batuecas, R. Díaz, and F. J. Pérez, “Comparative environmental assessment of two materials suited to central tower CSP technology,” *Solar Energy*, vol. 162, no. January, pp. 178–186, 2018.
- [113] O. S. Ahmed, “Corrosion behaviour of AISI 304 stainless steel in contact with eutectic salt for concentrated solar power plant applications,” 2013.
- [114] American Society for Testing and Materials, “A240: Standard Specification for Chromium and Chromium-Nickel Stainless Steel Plate for General Applications,” *ASTM Standards*, vol. I, p. 12, 2004.
- [115] American Society for Testing and Materials, “G1-03: Standard Practice for Preparing , Cleaning , and Evaluating Corrosion Test,” *ASTM Standards*, vol. 90, no. Reapproved 2011, pp. 1–9, 1999.
- [116] P. Mikkola, P. Ylhä, E. Levänen, and J. B. Rosenholm, “Effect of impurities on dispersion properties of alpha-alumina powder,” *Ceramics International*, vol. 30, no. 2, pp. 291–299, 2004.
- [117] F. R. Feret, D. Roy, and C. Boulanger, “Determination of alpha and beta alumina in ceramic alumina by X-ray diffraction,” *Spectrochimica acta, Part B: Atomic spectroscopy*, vol. 55, no. 7, pp. 1051–1061, 2000.
- [118] F. C. Larche, “Melting point of alpha-alumina,” *Journal of the Franklin Institute*, 1945.
- [119] S. J. Park and M. K. Seo, *Types of Composites*, vol. 18. 2011.
- [120] M. Wannaborworn, P. Praserttham, and B. Jongsomjit, “A comparative study of solvothermal and sol-gel-derived nanocrystalline alumina catalysts for ethanol dehydration,” *Journal of Nanomaterials*, vol. 2015, 2015.
- [121] S. Alexander, V. Gomez, and A. R. Barron, “Carboxylation and Decarboxylation of Aluminum Oxide Nanoparticles Using Bifunctional Carboxylic Acids and Octylamine,” *Journal of Nanomaterials*, vol. 2016, no. February, 2016.

- [122] K. Y. Paranjpe, "Alpha, Beta and Gamma Alumina as a catalyst -A Review," *The Pharma Innovation Journal*, vol. 6, no. 11, pp. 236–238, 2017.
- [123] Z. Said, R. Saidur, and N. A. Rahim, "Energy and exergy analysis of a flat plate solar collector using different sizes of aluminium oxide based nanofluid," *Journal of Cleaner Production*, vol. 133, pp. 518–530, 2016.
- [124] R. Kiruba, S. Vinod, A. W. Zaibudeen, R. V. Solomon, and J. Philip, "Stability and rheological properties of hybrid γ -Al₂O₃ nanofluids with cationic polyelectrolyte additives," *Colloids and Surfaces A: Physicochemical and Engineering Aspects*, vol. 555, no. May, pp. 63–71, 2018.
- [125] O. Beneš, R. J. M. Konings, S. Wurzer, M. Sierig, and A. Dockendorf, "A DSC study of the NaNO₃–KNO₃ system using an innovative encapsulation technique," *Thermochimica Acta*, vol. 509, no. 1–2, pp. 62–66, Sep. 2010.
- [126] P. Gimenez and S. Fereres, "Effect of Heating Rates and Composition on the Thermal Decomposition of Nitrate Based Molten Salts," *Energy Procedia*, vol. 69, pp. 654–662, 2015.
- [127] M. Bin Mohammad, G. A. Brooks, and M. A. Rhamdhani, "Thermal analysis of molten ternary lithium-sodium-potassium nitrates," *Renewable Energy*, vol. 104, pp. 76–87, 2017.
- [128] R. I. Olivares, "The thermal stability of molten nitrite/nitrates salt for solar thermal energy storage in different atmospheres," *Solar Energy*, vol. 86, no. 9, pp. 2576–2583, 2012.
- [129] S. Jeong and B. Jo, "Understanding mechanism of enhanced specific heat of single molten salt-based nanofluids: Comparison with acid-modified salt," *Journal of Molecular Liquids*, p. 116561, 2021.
- [130] A. Svobodova-Sedlackova, A. Calderón, C. Barreneche, P. Gamallo, and A. I. Fernández, "Understanding the abnormal thermal behavior of nanofluids through infrared thermography and thermo-physical characterization," *Scientific Reports*, vol. 11, no. 1, pp. 1–11, 2021.
- [131] R. Taylor *et al.*, "Small particles, big impacts: A review of the diverse applications of nanofluids," *Journal of Applied Physics*, vol. 113, no. 1, 2013.
- [132] S.-Q. Zhou and R. Ni, "Measurement of the specific heat capacity of water-based Al₂O₃

- nanofluid,” *Applied Physics Letters*, vol. 92, no. 9, p. 093123, 2008.
- [133] S. Akilu, A. T. Baheta, K. V. Sharma, and M. A. Said, “Experimental determination of nanofluid specific heat with SiO₂ nanoparticles in different base fluids,” *AIP Conference Proceedings*, vol. 1877, no. September, 2017.
- [134] L. di Zhang, X. Chen, Y. ting Wu, Y. wei Lu, and C. fang Ma, “Effect of nanoparticle dispersion on enhancing the specific heat capacity of quaternary nitrate for solar thermal energy storage application,” *Solar Energy Materials and Solar Cells*, vol. 157, pp. 808–813, 2016.
- [135] B. Muñoz-Sánchez, J. Nieto-Maestre, I. Iparraguirre-Torres, A. García-Romero, and J. M. Sala-Lizarraga, “Molten salt-based nanofluids as efficient heat transfer and storage materials at high temperatures. An overview of the literature,” *Renewable and Sustainable Energy Reviews*, vol. 82, pp. 3924–3945, 2018.
- [136] H. Riazi, T. Murphy, G. B. Webber, R. Atkin, S. S. M. Tehrani, and R. A. Taylor, “Specific heat control of nanofluids: A critical review,” *International Journal of Thermal Sciences*, vol. 107, pp. 25–38, 2016.
- [137] Q. Peng, X. Wei, J. Ding, J. Yang, and X. Yang, “High-temperature thermal stability of molten salt materials,” *International Journal of Energy Research*, vol. 32, pp. 1164–1174, 2008.
- [138] L. Qiu *et al.*, “A review of recent advances in thermophysical properties at the nanoscale: From solid state to colloids,” *Physics Reports*, vol. 843, pp. 1–81, 2020.
- [139] S. F. Ahmed, M. Khalid, W. Rashmi, A. Chan, and K. Shahbaz, “Recent progress in solar thermal energy storage using nanomaterials,” *Renewable and Sustainable Energy Reviews*, vol. 67, pp. 450–460, 2017.
- [140] B. Bakthavatchalam, K. Habib, R. Saidur, B. B. Saha, and K. Irshad, “Comprehensive study on nanofluid and ionanofluid for heat transfer enhancement: A review on current and future perspective,” *Journal of Molecular Liquids*, vol. 305, p. 112787, 2020.
- [141] S. J. Wagner and E. S. Rubin, “Economic implications of thermal energy storage for concentrated solar thermal power,” *Renewable Energy*, vol. 61, pp. 81–95, 2014.

- [142] REN21, *Renewables 2018 Global Status Report*. 2018.
- [143] S. M. Hasnain, “Review on sustainable thermal energy storage technologies, part I: Heat storage materials and techniques,” *Energy Conversion and Management*, vol. 39, no. 11, pp. 1127–1138, 1998.
- [144] MIT, “X-Ray Diffraction Shared Experimental Facility.” [Online]. Available: <http://prism.mit.edu/%0Axray/education/downloads.html>.
- [145] A. G. Fernández, M. I. Lasanta, and F. J. Pérez, “Molten salt corrosion of stainless steels and low-Cr steel in CSP plants,” *Oxidation of Metals*, vol. 78, no. 5–6, pp. 329–348, 2012.
- [146] A. G. Fernández and F. J. Pérez, “Improvement of the corrosion properties in ternary molten nitrate salts for direct energy storage in CSP plants,” *Solar Energy*, vol. 134, no. 3, pp. 468–478, 2016.
- [147] A. Bonk, D. Rückle, S. Kaesche, M. Braun, and T. Bauer, “Impact of Solar Salt aging on corrosion of martensitic and austenitic steel for concentrating solar power plants,” *Solar Energy Materials and Solar Cells*, vol. 203, no. September, p. 110162, 2019.
- [148] J. L. Marulanda, S. I. Castañeda, and F. J. Perez, “Study microstructure and composition of oxidation in steam at 700 and 750°C of austenitic steels aisi 304, 316 and 317,” *Revista Facultad de Ingenieria*, no. 67, pp. 98–111, 2013.
- [149] Y. Yamamoto *et al.*, “Development of Creep-Resistant, Alumina-Forming Ferrous Alloys for High-Temperature Structural Use,” pp. 1–10, 2018.
- [150] Y. Yamamoto, M. P. Brady, M. L. Santella, H. Bei, P. J. Maziasz, and B. A. Pint, “Overview of strategies for high-temperature creep and oxidation resistance of alumina-forming austenitic stainless steels,” *Metallurgical and Materials Transactions A: Physical Metallurgy and Materials Science*, vol. 42, no. 4, pp. 922–931, 2011.
- [151] M. P. Brady *et al.*, “The development of alumina-forming austenitic stainless steels for high-temperature structural use,” *Jom*, vol. 60, no. 7, pp. 12–18, 2008.
- [152] M. P. Brady, Y. Yamamoto, M. L. Santella, and B. A. Pint, “Effects of minor alloy additions and oxidation temperature on protective alumina scale formation in creep-resistant austenitic stainless steels,” *Scripta Materialia*, vol. 57, no. 12, pp. 1117–1120, 2007.

- [153] M. P. Brady, K. A. Unocic, M. J. Lance, M. L. Santella, Y. Yamamoto, and L. R. Walker, "Increasing the upper temperature oxidation limit of alumina forming austenitic stainless steels in air with water vapor," *Oxidation of Metals*, vol. 75, no. 5–6, pp. 337–357, 2011.
- [154] Y. Yamamoto *et al.*, "Alumina-forming austenitic stainless steels strengthened by laves phase and MC carbide precipitates," *Metallurgical and Materials Transactions A: Physical Metallurgy and Materials Science*, vol. 38 A, no. 11, pp. 2737–2746, 2007.
- [155] S. H. Goods and R. W. Bradshaw, "Corrosion of Stainless Steels and Carbon Steel by Molten Mixtures of Commercial Nitrate Salts," *Journal of Materials Engineering and Performance*, vol. 13, no. 1, pp. 78–87, 2004.
- [156] J. Gasia, L. Miró, and L. F. Cabeza, "Review on system and materials requirements for high temperature thermal energy storage. Part 1: General requirements," *Renewable and Sustainable Energy Reviews*, vol. 75, no. May 2016, pp. 1320–1338, 2017.
- [157] B. Ma, D. Shin, and D. Banerjee, "One-step synthesis of molten salt nanofluid for thermal energy storage application – a comprehensive analysis on thermophysical property, corrosion behavior, and economic benefit," *Journal of Energy Storage*, vol. 35, no. December 2020, p. 102278, 2021.
- [158] M. Lasfargues, Q. Geng, H. Cao, and Y. Ding, "Mechanical Dispersion of Nanoparticles and Its Effect on the Specific Heat Capacity of Impure Binary Nitrate Salt Mixtures," *Nanomaterials*, vol. 5, no. 3, pp. 1136–1146, 2015.
- [159] Y. F. Zhu, L. Shi, C. Zhang, X. Z. Yang, and J. Liang, "Preparation and properties of alumina composites modified by electric field-induced alignment of carbon nanotubes," *Applied Physics A: Materials Science and Processing*, vol. 89, no. 3, pp. 761–767, 2007.
- [160] K. Xu and Y. Chen, "Raman spectroscopic studies of mixed crystals of NaNO₃–KNO₃ quenched from different temperatures: evidence for limited solid solutions in the system," *Journal of Raman Spectroscopy*, vol. 30, no. 6, pp. 441–448, 1999.
- [161] R. W. Berg, D. H. Kerridge, and P. H. Larsen, "NaNO₂ + NaNO₃ Phase Diagram: New Data from DSC and Raman Spectroscopy," *Journal of Chemical & Engineering Data*, pp. 34–39, 2006.

- [162] R. W. Berg and D. H. Kerridge, "Raman mapping in the elucidation of solid salt eutectic and near eutectic structures," *Journal of Raman Spectroscopy*, vol. 33, no. 3, pp. 165–172, 2002.